Feasibility Study of a Combined Wind and Solar Park within the Energy Storage Lake of Delta21

Panagiotis Mastrodimos

TU Delft

Feasibility Study of a Combined Wind and Solar Park within the Energy Storage Lake of Delta21

by

Panagiotis Mastrodimos

to obtain the degree of Master of Science
at the Delft University of Technology,
to be defended publicly on Tuesday January 17, 2023 at 10:00 AM.

Student number:	5369142	
Project duration:	March 2022 – January 2023	
Supervisors:	Dr-Ing. Sebastian Schreier	TU Delft ***[Chair]***
	Dr. Harleigh Seyffert	TU Delft
	Dr. Xiaoli Jiang	TU Delft
	D.r Hesan Ziar	TU Delft
	Willem Biesheuvel	GroenLeven
	Huub Lavooij	Delta21
	Leen Berke	Delta21

Abstract

The penetration of the renewable energy sources in the global market has been constantly growing over the last years. This trend is expected to accelerate even more in the future due to the improving technologies, the economies of scale, the competitive supply chains and the improving developer experience. The main challenge for a faster and wider implementation of these resources is their intermittent character and the limitations that this implies.

A concept that successfully deals with this variable energy output is the Hybrid Power Plants (HPP). HPPs combine at least two different sources of energy with the goal of delivering stable power with reduced fluctuations throughout the year. In addition, HPPs present various other synergies such as in operational costs or in the developing processes, that could lead to a reduced Levelized Cost of Energy (LCOE).

The goal of this thesis is to assess the potential synergy of a combined wind and solar park for the case of the Energy Storage Lake (ESL) of the project Delta21. The Delta21 project has a twofold character: firstly, the usage of the ESL as a large battery integrated with green energy production and secondly the protection of the inland against floods due to high sea level or superfluous river discharge. The main challenge for this specific case is the large water level fluctuations within the lake on a daily basis due to the operation of the lake.

The feasibility of a hybrid wind and solar park can be examined by various different perspectives and disciplines. Among these relevant components, the most frequently studied ones are the optimization of the energy resources, the use of common electrical infrastructure and the effect of the intermittent wind turbine shadows on the solar panels. Due to the special conditions, with the large water level fluctuations met at the lake, two more components become critical and these are the type of foundation of the wind turbines and the mooring configuration for the floating solar units.

This project is evaluating a new potential synergy that regards the use of the wind turbine towers as anchoring points for the floating solar units. Therefore, the research is focused on the estimation of the forces acting on a floating solar unit. These forces are a combination of wind loads acting on the solar panels and the freeboard of the floaters, and wave forces acting on the submerged part of the floaters. In particular, the technology of the floating solar boat as introduced by GroenLeven and the small scale wind turbines as designed by Dutch Wind Design are adopted for this project.

Analytical formulations are used for the calculation of the wind loads. As for the wave forces, the linear potential theory is used and the calculations of the hydrodynamic coefficients and wave exciting forces are performed through the Boundary Element Method (BEM) software NEMOH. After the computation of first order wave forces and the corresponding responses of the floaters, the far-field approach is used for the estimation of the Quadratic Transfer Function (QTF) of the drift force.

The methodology developed in this project and the accuracy of the model are validated with the use of reference data that regard the interaction of connected floating units placed in a close proximity and the corresponding second order wave forces as predicted by the far-field approach.

The resulting forces as exerted on a single solar boat are then expanded accordingly for a solar unit of 4.1MW installed capacity consisting of 400 solar boats, as defined by the base case design. When the drift force density spectrum is adopted, the total mooring force is 90% higher than the rest of the forces acting on the tower. The corresponding wind loads on the solar boat account for only 4.5% of the mooring force. In comparison, for four different scenarios that make use of the maximum value of the drift force and include a variable parameter, the ratio of the mooring force over the tower forces presents a wide range with values of

35% up to 164%. The most influential parameter in the total solar unit force is the incident wave height.

Finally, the potential mooring forces originating from loads on the solar units do not seem to be a showstopper for the proposed configuration. However, further work is required for the evaluation of the financial impact of such a system as well as the technical feasibility of the connection points. Other recommendations regard the optimization of the layout of the HPP with the objectives of maximum energy production or the minimization of LCOE.

Acknowledgements

This research marks the end of my academic journey at Delft University of Technology. It all started several years ago back in Greece at Aristotle University of Thessaloniki and my studies as a civil engineer. I can still recall my attempts on writing a motivational letter for the application process of the track of Offshore and Dredging Engineering. It was already that time that I realized that renewable sources of energy is the sector that I would like to focus upon. Fast forward to the end of my first year of studies at TU Delft, the complexity of offshore floating structures made me look in awe the attempts of stabilizing huge floating wind turbines, mooring complex floating solar parks and predicting the responses of large vessels. I could not be luckier to combine these elements in my final project as a student. A project that could not be have been accomplished without several people that I would like to grab the opportunity and thank individually for their support and contribution.

I would like to express my sincere gratitude to the committee members for their support and guidance throughout the graduation research. Starting with my TU Delft daily supervisor Dr-Ing. Sebastian Schreier who was the one to always help me find the correct direction. In most cases, this direction was towards the scientific approach of my work, when through his feedback and constant questions pushed me to find my own way and shape my project. His constant insights and diverse techniques of looking at problems as if they were opportunities have made our conversations nothing but pleasant and insightful for my research. However, I have to mention other cases as well, when I felt completely disoriented and lost during these 9 months, and our talks combined with his friendly advice helped me carry on. Secondly, I would like to thank Dr. Harleigh Seyffert, Dr. Xiaoli Jiang and Dr. Hesan Ziar for joining the graduation committee. Special thanks to Huub Lavooij and Leen Berke, the initiators of Delta21, for allowing me to participate and contribute as much as possible to such a large project for the Netherlands. Your enthusiasm and focus is very admirable and I hope to see this project coming into reality in the near future. Following, I would like to thank my company supervisor Willem Biesheuvel and GroenLeven for giving me the opportunity of graduating within a company. This collaboration gave a useful insight to approach my project from the industry point of view. Finally, many thanks to Ton Bos and Charles Vaanhold from Dutch Wind Design for the valuable input on this project.

Throughout this two-year journey in the Netherlands, I had the chance to meet and connect with many diverse individuals, both at an academic as well as a personal level. People that became friends and I know I can rely on. Special thanks to Andrew, Joanna and Kostas for always supporting me and giving an optimistic touch in my life. And of course to my family, without whom none of these would have ever happened. You all contributed in unique ways of shaping my character and I could not be more thankful for that. I hope that my professional career will be a chance to make a change for the better towards every direction!

Panagiotis Mastrodimos
January 2023, Delft

Contents

List of Figures

List of Tables

1 | Introduction

This chapter is introducing the concept of the hybrid power plants and their relevant components. The background of the problem in hand as well as the main research question follow.

1.1 Hybrid Power Plants

The penetration of the renewable energy resources in the global electricity market has been constantly growing over the past decades. The environmental concern and the corresponding progressive depletion of fossil fuels has shifted research and attention towards renewable resources.

Within 2020, the share of renewable energy in the global electricity mix, reported a high record estimated at 29%. Moreover, solar photovoltaics (PV) had a record breaking year reaching up to 760GW of installed power including both on-grid and off-grid systems. A comparable record high was achieved for wind power leading to 743GW of total installed capacity [73], with 707.4GW installed at onshore locations and the rest offshore. Specifically for the case of the Netherlands, the PV installed capacity in 2020 reached to 10.1GW while the wind capacity to 6.5GW, originating from 2.6GW and 3.9GW of offshore and onshore respectively [42]. However, the stochastic nature of these two resources and the corresponding technical challenges related to grid power supply are the main obstructions towards further deployment and installation [5]. The risks related to this fluctuating and unpredictable nature can be mitigated up to a certain level with the so called hybrid power plants (HPP). These HPP combine at least 2 energy resources which are then connected through substations and provide combined power, and they offer potential reduction in the inter-annual variability as well as reduction in the installation and maintenance costs [3]. Solar radiation is present during the day and summer, while the wind can compensate for the absence of solar production during night and decreased performance in winter. The main advantage of such a HPP compared to independently operating systems can be summarized to the following [101, 107]:

- space can be used more efficiently, with the increase in the installed capacity and energy output per square meter; this can lead to a reduced Levelized Cost of Energy (LCOE)
- a higher capacity factor and a more stable power output can be achieved at locations where the two energy sources are complementary (negative correlated)
- infrastructure investment costs related to electrical components can be reduced if a single grid connection point is used
- the needs in energy balancing and curtailments are significantly reduced when compared to pure solar or wind power plants
- from a developer's point of view, new synergies are created within the development and permitting process as well as for the operation and maintenance of the plants; this leads to an overall reduction of development, capital and operational expenditures
- hybrid power plants can be advantageous in terms of dispatching power in the market; in cases where the electricity market prices are negatively correlated to wind power, the hybrid power plant could earn revenue from the market, when prices are high, thanks to the solar resource

There are numerous studies that have investigated the potential exploitation of wind and solar PV power production complementarity to deal with this variability in energy output [19, 35, 75, 110]. The potential synergy of developing offshore floating wind and solar energy in a case study for the area off Asturias (Spain) has been performed in [62]. The results showed that the capacity density (MW/km^2) and the specific yield

(MWh/km^2/year) can be increased by 10 and 7 times respectively for a combined wind-solar park in comparison to a stand-alone wind farm. More significantly however, the power output variability of the combined park was reduced by 68% relative to the wind farm.
In Figure 1.1, the opportunity of co-locating the solar panels in the space available between the wind turbines is presented.

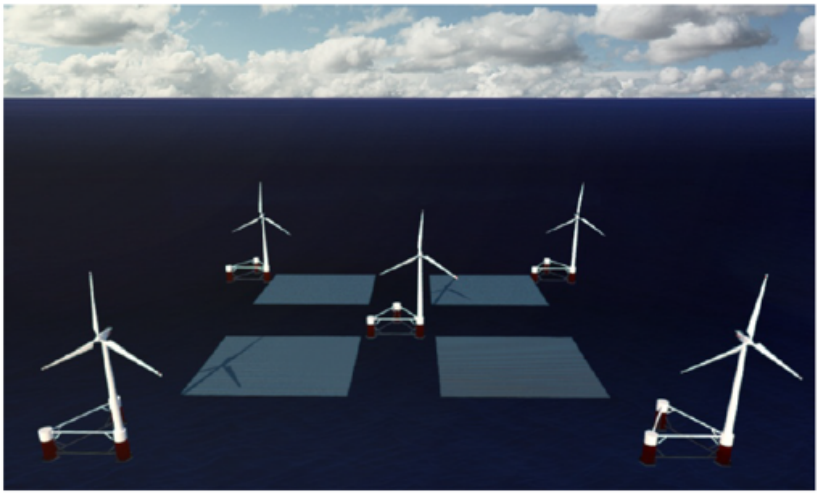

Figure 1.1: Opportunities for synergies between wind and solar parks [62]

The first utility scale hybrid plant in Europe was developed in Haringvlied (the Netherlands). The layout of the existing wind-solar-energy storage system and the controller's features were presented in [80], and the simulated hybrid system was shown to satisfy all requirements. Another study [18] attempted to investigate the advantages of an offshore hybrid farm consisting of wind turbines and PV panels on the western coast of the Iberian Peninsula. The analysis was performed through a classification based on the stability of resource, richness of the offshore resource, economic and risk factors. The study concluded that the examined combination of wind and solar resources reduce the spatial and temporal variability.
A technical-economic risk study for the financial impact of PV power insertion into a wind energy system for the case of Brazil was carried out in [12]. The findings showed that even if the PV equipment is more expensive than wind, the installation of a certain number of PV panels has a high probability of making the project economically successful.
Bekele and Palm [6] investigated the possibility of providing electricity to a remote location in Ethiopia, from a stand-alone solar-wind system. They proposed a list of different feasible power supply systems and ranked them based on their Net Present Value (NPV). They reached to the conclusion that an energy system which includes renewable resources is the most appropriate solution besides the slightly higher Net Present Cost (NPC).
For a case study in Libya [50], after numerous simulations were performed, the results showed that the most economically feasible design to supply average load connected to gird is a combination of PV arrays and wind turbines.
The spatiotemporal variability and complementarity of wind and solar resources within Germany was studied in [92], by using different time scales (daily, seasonal, annual). The results obtained, revealed the need of analyzing the correlation of these two resources in even smaller time scales such as sub-daily. Klonari et al. [57] mapped all the operating or under development hybrid wind-solar parks, in an attempt to identify drivers and barriers that could help in the formulation of new policies with the ultimate goal of boosting their development.
WindEurope has developed and made publicly available an online data-set of co-located wind and solar power plants with storage technologies [108]. A screenshot of this database is presented in Figure 1.2. The orange dots correspond to projects in which a storage system is also implemented while the blue dots are the ones without storage.

Figure 1.2: Co-located hybrid wind and solar projects [108]

From the 27 projects included in this data-set, the main functionalities of the parks can be divided into the following:

- Enhanced and smoother power output (51%): make power generation profile flatter over time compared to a pure wind or solar system, eliminate rapid voltage and power ramps
- Increased capacity factor (26%): better utilization of the converter, transformer and connection capacity through negative correlation of wind and solar resources
- Weak power grid (33%): provide more predictable and schedulable power dispatch, assisting in the satisfaction of load demand for cases/areas where the power grid is too weak to provide reliable power supply.

Mazzeo et al .[69] performed a literature review on the trends of research in the field of hybrid PV-wind systems including 550 articles. The main findings of this review are:

- the most prevalent study methodology is the simulation
- parametric analysis is most commonly met with HOMER being the most widely used software
- Loss of Power Supply Probability (LPSP), Resource Fraction (RF), Cost of Energy (COE), Net Present Cost (NPC) and the emissions of CO_2 (E) are the most used indicators for the energy, economic and environmental analysis respectively
- battery is the most widely used auxiliary component
- the optimization techniques most frequently used in studies are the Particle Swarm Optimization (PSO) and Genetic Algorithm (GA)
- stand-alone systems are investigated in the majority of projects compared to grid-connected

As the demand in reliable and stable electricity remains a priority, the benefits of co-locating wind and solar technologies present significant advantages of these technologies compared to when used separately [20, 55].

In addition, as both the floating PV technologies [14] and floating offshore wind [47] structures are becoming more and more appealing with the corresponding reduction in cost, hybrid systems on water bodies or offshore areas will be further investigated in the future.

1.1.1 Energy Storage Systems

In addition to the combination of two energy resources, the inclusion of an energy storage system (ESS) would allow for further regulation of their intermittency and seasonality of electricity generation [25]. The main functions that energy storage technologies can perform when applied to energy systems can be summarized into the following [22, 30, 95]: providing operational support to the grid, load shifting, peak shaving and stabilizing the grid by frequency and voltage control. This consequently means that ESSs can play an important role in the reliability and stability of the grid. .Moreover, ESSs can generate revenue by providing ancillary services but also add flexibility to the operational strategies and achieve the objectives as set by the demand-side management. In conclusion, they can significantly contribute to a greater insertion of renewable energy sources into the energy matrix.

For this thesis, the focus is drawn on the case of Delta21 project which offers the possibility of performing a large energy storage function. Moreover, the technologies adopted are the solar boat of GroenLeven and the small scale wind turbine of Dutch Wind Design.

1.2 The case of Delta21

Delta21 is a project that seeks to increase the water safety in the Rhine-Meuse Delta. A combined event of high sea level and a high river discharge could be threatening for the water safety and therefore enormous dike reinforcements would be needed to prevent flooding. The plan consists of building a new dike at the west side of the Haringvliet, that can pump the water out of the Haringlviet when the two scenarios occur simultaneously.

However, such a system would only operate 1-2 times every 10 years and this could potentially lead to high failure probability. This could be prevented if the pumps operate in a daily basis for a different purpose. The proposed idea is to create an Energy Storage Lake (ESL) in which energy can be stored and again generated with the use of the pumps/turbines. The pumps/turbines will have an installed capacity of 1.8GWe and could exchange 430 million m^3 of seawater once a day. Therefore, the project can be used in a twofold way: protect inland from a high sea level and also move superfluous river discharge into the North Sea.

The location and the layout of the lake are presented in Figure 1.3 [27].

Figure 1.3: Location and layout of the Delta21 ESL [27]

Delta21 is also looking into other possibilities for multiuse of the lake. One of these is the combination of a wind park and photovoltaic panels. A surface area of approximately 43km^2 offers a great opportunity for such a park. The hybrid park can generate renewable electricity with a further possibility of storing the excess energy through the pump system. The battery can be charged when there is surplus of energy by using the pumping station to pump water out of the lake until it is completely empty. Afterwards, the battery can be discharged and therefore provide energy to the grid, by utilizing the turbine function of the station while water from the sea is

filling up the lake again. This large battery with the possibility of storing 1.8GWe would consequently lead to a very constant flow of energy, enhancing in this way the performance of the renewable sources.

However, the pumped storage use would also lead to a fluctuating water level within the reservoir, with a maximum rate of 11m per 12 hours. These large water fluctuations as well as the blending of fresh water coming from the river and the brackish sea water bring up new challenges. Consequently, certain limitations and considerations must be applied during the selection and the design, both for the wind turbines and the PV panels.

The maximum water level in the ESL will be at NAP -5m while the lowest at NAP -16m. The bottom of the lake is going to be excavated at the level of NAP -17.5m. This consequently means that after the discharge of the water, the minimum water level is going to be 1.5m. It is therefore challenging to install either fixed or floating structures with this enormously fluctuating water level.

1.3 GroenLeven

The benefits of FPV systems can be summarized into the following: the large availability of water for the cleaning of the panels and the significantly increased efficiency of the panels due to the water cooling of the system. The energy storage lake offers a friendly environment for these solar panels, as the wave action will be considerably lower inside the lake, when compared with open sea conditions.
GroenLeven is already a leader in the implementation of floating solar parks. Their floating solar boat solution offers the following advantages over the rest of the available structures [9]:

- a reduced direct water contact footprint that accounts only for the 15% of the total size and enables the water to move freely underneath the structure
- easy and safe maintenance is guaranteed through the stable walkways created between the boats
- an integrated DC cabling system with protected cables running under the walkways; inverters at each solar row and a floating transformer leading to a total reduction of the costs and the electrical losses
- an east-west orientation of the panels at an optimized tilt angle leading to an increased strength against wind
- a layout of the floating blocks that allows light transmission and thus minimizing the ecological impact of the water body by preventing the reduction in primary algae production
- a modular FPV system which can be easily scaled and in the same time the installation rate can be maximized due to the stardarized construction procedure

Besides the aforementioned advantages, the usage of this technology, which is solely applied in sandpits and lakes, forms new challenges. The main ones are: the fresh-salty environment within the lake that needs to be accounted for during the steel selection, the mooring system and the power cables that have to follow the water fluctuations and finally the integration of the electrical system for a park that will reach up to hundreds of MW installed.

1.4 Dutch Wind Design

The innovative windmill design of Dutch Wind Design (DWD) is definitely a solution worth investigating for the Delta21 project. This design is characterized by a large sized direct drive ring generator that holds the blades. Next to that, the aerodynamic shape of the ring accelerates the wind into the blade section and thus increases the energy captured. With a small installed capacity of around 128kW (which can be further adjusted to meet site-specific conditions), these turbines offer multiple advantages when compared with larger conventional turbines. These according to [11] are:

- higher efficiency of about 50% especially in the range of 3.5 to 10m/s which is also to be found around the lake; generator efficiency also reaches values up to 97.98%
- the aerodynamic shape of the ring allows the energy level in the air to recover significantly faster than conventional turbines, and thus the wake effects are minimized allowing for a spacing of 3 rotor diameters between the turbines (for common turbines the distance is set to about 5 rotor diameters)

- long lifetime which allows the DWD turbines to service up to 30 years (5-10 years more than the common turbines)
- maintenance needed is minimized due to the modular generator and its control strategy; the lack of a gearbox and the over-sized main bearing contribute as well to this
- short payback time as a result of the long lifespan, low maintenance and high efficiency, that can reach at maximum the 7 years
- quick installation since there is no need for special crane vessels
- low noise stemming from the fact that no gearbox is present and that the tip speed is very low
- no horizon pollution due to the relative small wind turbine size, leading to a small object shadow as well
- the small size and the alternative darker colors have proved to minimize bird impacts and thus making DWD turbine friendlier to animals

1.5 Aspects of HPP design

When zooming out of the design of a HPP, there are multiple aspects or parameters that can be investigated and properly tuned for every individual case. For the case of the Delta21 ESL these parameters have been categorized as presented in Figure 1.4. The first three aspects have been selected after an overview of the research on hybrid parks, while the last two are of importance for the specific site.

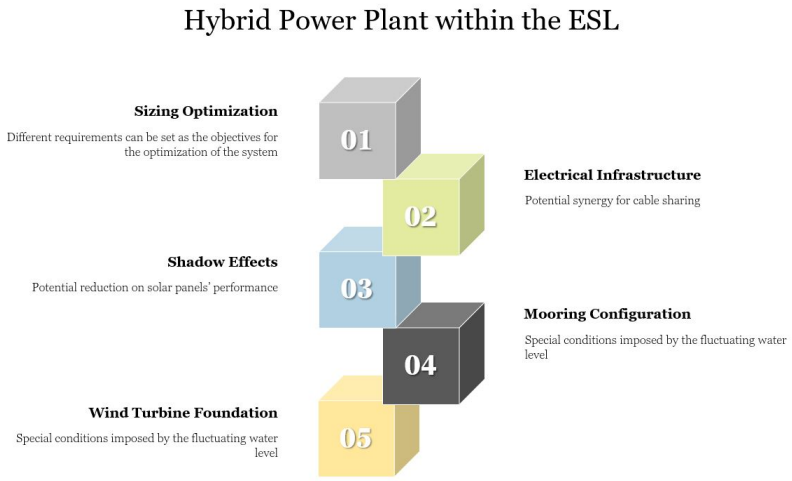

Figure 1.4: HPP parameters

A brief discussion of the most relevant properties of each one of the aforementioned parameters will follow.

1.5.1 Sizing Optimization

The optimization of the layout has as an utter goal the achievement of a specific objective. In most cases, the objective is set to be the minimization of the cost while in others it might be the maximization of the energy production. The variables of the system are most frequently set to be the size/installed capacity of the wind turbines and the solar panels. Particle Swarm Optimization (PSO) is the method most frequently used in relevant studies in the literature [32, 66, 78, 91]. Other studies [2, 70, 109] adopted a Genetic Algorithm (GA) to investigate the optimization of such hybrid systems.

In addition,the software that is most frequently met in hybrid optimization studies is HOMER. HOMER makes simulations for every hour of a whole year and checks whether the load demand is met by the system. After that, it finds the configuration that can achieve that with minimum cost, taking into account a fixed cost per hour and energy cost per kWh [99, 100],. Matrix Laboratory (MATLAB) is also used for the the sizing and economic analysis of such a hybrid system with different concepts for energy storage [26, 72].

Most of the studies perform an analysis of the power production of a hybrid system based on historical data of hourly global solar irradiation as well as hourly mean values of wind speed. Ekren et al.[28] proposed a different approach based on the utilization of probabilistic distributions to perform random input simulations for the system, in a case study for a PV-solar system with battery storage.

Another field which also seems to offer a good opportunity for the implementation of a hybrid wind and solar system is that of coupling with hydroelectric power stations. The existence of such a hydroelectric plant can be used for energy storage when a surplus from the wind turbines and PV panels occurs and therefore can compensate for the varying nature of these two resources. This coupling can lead to a reduction in both needs for energy storage and the energy losses inherently associated with storage [54].

Ma et al. [65] also performed a similar analysis but in this case a solar-wind-pumped storage system was investigated in a standalone mode for an isolated microgrid for a remote island of a small scale of just a few kilowatts. The system optimization was based on two different criteria: the first one is related to the reliability of such a system and is the LPSP and the second with the COE. The findings of this study revealed that for the optimization of such a system, the profile of the load demand is the single most important factor.

Other optimization methods that have been performed throughout the last decade are moving-window optimization and multi-objective optimization. The former proved to be a very useful tool that can lead to the optimized solution when long and short term variability in the energy outcome is requested [59]. The latter method has been used in [61] with three different objectives namely: minimization of power generation, maximization of power supply reliability and maximization of power fill rate. For this case, varying environmental conditions, different monetary penalties for unmet demand and multiple load profiles were studied. The conclusion of the study was that the highest impact for the determination of the sizing comes from the available environmental resources.

After this short review of existing studies on the optimization of hybrid wind and solar system it has become evident that it is a field that has been widely investigated over the last 15 years. The existence of different tools-software and optimization techniques allow for a wide range of approaches that such a topic can be confronted. In most cases, the optimization is mainly dependent on the available resources (solar irradiation and wind speeds) and the electricity load profile that has to be met.

1.5.2 Electrical Infrastructure

One of the promising features of a combined hybrid wind and solar park with a storage unit is the common usage of the electrical infrastructure. The required inverters, converters and medium/high voltage cabling for the transfer of electricity are components that have a profound share in the total investment cost.

The main issue with respect to transport cable is that a renewable system does not produce all the time at the rated capacity and even when it does the system losses result in a sub-optimal usage of the cable.

More specifically, the electric grid infrastructure is one of the main cost drivers for offshore wind farms, accounting for up to one third of the overall project cost, with the export cable being the main contributor [74]. Next to that, the intermittent nature of wind leads to a non-optimal usage of the cable due to irregular transitions between states of high and low power [84]. Therefore, a shared grid infrastructure with the solar farm could lead to cost reduction and better cable utilization.

Golroodbari et al. [37] investigated the potential of incorporating a floating solar park in an existing Dutch offshore wind farm. Worth mentioning is the conclusion that the inclusion of a certain number of FPV capacity could lead to a potential increase in the cable capacity factor from 49% up to 88%. However, the actual cost of FPV technology and the available subsidy scheme are the two economical factors that will regulate the optimal share of installed solar power.

The "cable pooling" which is the possibility of sharing only one cable for both wind and solar energy has also been investigated by Mertens [71]. In this paper, it is stated that a baseload profile in the Netherlands can be achieved using a ratio of wind to solar energy yield $E_W/E_S = 1.7$ and a ratio of wind to solar installed power $P_W/P_S = 0.6$. More importantly however, assuming a capacity factor of 30% and 10% for wind and solar respectively, when a common cable is used, for a 100% yearly match the energy curtailment reaches up to 6% while for 75% energy match it drops to only 1%.

Another study that looked deeper in the same direction was conducted by Ara et al. [1]. A two-level planning approach was introduced for the techno-economic feasibility of a hybrid wind-solar system. For this case study off the coast of India, the results showed that the LCOE is reduced by 8% when the existing electrical components of the wind park are utilized by adding solar panels.

Sharing the same electrical infrastructure in a hybrid park can further reduce the cost and increase the capacity factor of the cable. However, such an approach should always be attached to an investigation of the layout and the percentage of capacities installed.

1.5.3 Shadow Effects

Another important aspect of a hybrid wind and solar park is the effect of shading of the wind turbines on the performance of the photovoltaic panels. Two different types of turbine shading can be distinguished: self-shading and invasion shading. The latter takes place mostly during early morning and afternoon hours when the solar radiation is low and therefore has a small impact on the energy production, while the former mainly occurs during daytime and therefore may impact the overall PV output. Again, self-shading can be further analyzed into tower shading and blade shading (shadow flickers), corresponding to slow and fast changing shadows respectively.

The effect of shadowing on the performance of the solar panels can be approached by two ways: in a macro and in a micro scale. The former is related to the overall production losses within a solar park while the latter with the reduced production of a single PV module.

Interestingly, in a micro scale approach of PV modules, the total shadowing of a single cell among an array of 36 serially connected cells can cause a 30% reduction on the PV output [94]. This reduction is mostly affected by the amount of series resistance of PV module and the current mismatch among the shaded and unshaded cells. However, the assumption of constant shadowing is not applicable in the case of a hybrid park since the wind turbines are going to introduce slow and fast moving shadows, and the losses of the system in a macro scale approach are fairly low [4].

There are two approaches when it comes to the evaluation of incoming irradiation. The first approach makes the assumption of an every day-perfect day and uses "Clear Sky" equations whereas the second requires the use of measured data of global-horizontal and diffuse-horizontal solar radiation and therefore takes into account the true variety of daily conditions [93].

Moreover, the adopted model for the wind turbine shading can highly affect the analysis. The most used approaches are the opaque sphere, blades as disks, tower only and that of a combination of tower and fast moving blades shadows. A difference of up to 2% in shadow losses can occur in the case of comparing the only tower and the dynamic model [85].

In a study performed for two different latitudes onshore: 32^o and 50^o, by calculating the shadow patterns and trajectories, it was concluded that for a location of 50^o the effect is significantly larger [67]. However, for both cases the main outcome is that the average percentage of land loss due to wind turbine shading is less than 1%. This result prerequisites the existence of maintenance lanes around the wind turbines which cannot be used in any case for the installation of the solar panels.

Ludwig et al. [63] evaluated the onsite integration of a hybrid PV-wind power plant in Germany. Among other aspects, they investigated the effects of turbine shading on the panels. By performing simulations with different time steps and different % for each of the two resources (varying thus the distance between a turbine and a panel), they concluded that even for the worst case scenario -denser layout- the power losses did not exceed the 2.3%.

The aforementioned value can further lowered to under 1% if an optimization with the objective of minimizing the shadow losses is further pursued [85].

In conclusion, the effects of wind turbines' shadows on the solar panels should be taken into account in the design. However, this phenomenon will only lead to low power losses which can be further compensated for if a denser layout -and hence a higher yield- is incorporated. Lastly, the fast moving blade shadows should be further looked into.

1.5.4 Mooring Configuration

Besides the components relevant to energy production, the structural integrity in a hybrid system must be studied. For the case of Delta21, this is a very important field since the 11m fluctuation of the water level in a bi-daily basis entails risks and challenges. For the PV panels, the solution of a bottom founded system is rejected since for the minimum water level within the lake, a large and wide structure would be left standing at 12.5m from the bottom. Therefore, a floating approach seems more suitable for this case. However, it is considered that water level fluctuations and shallow depths are among the key challenges for the mooring system [43]. Figure 1.5 shows the typical arrangement of floating solar system. The mooring system that provides station keeping for the floating structure can be achieved in two ways. The first configuration is bottom mooring which can be implemented by

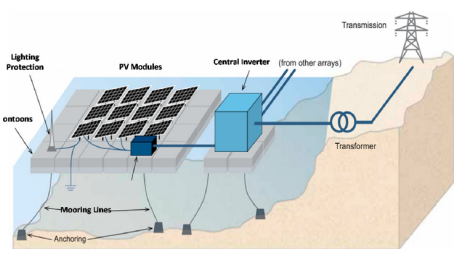

Figure 1.5: Schematic overview of a typical floating solar system [87]

either anchors or suction piles. Shoreline mooring is the other option for small and shallow basins where bottom mooring may introduce problems in the materials of the seabed [34]. In addition, the mooring configuration can be either taut or catenary. The catenary mooring system is exploiting the self-weight of the mooring line to cope with the floater's static offset and dynamic motions and it is the most widely used system for medium and shallow waters. On the other hand, the taut leg system allows for a smaller anchor footprint and therefore less material usage [64].

In water bodies where the water level fluctuation is high, a catenary mooring system is more suitable than a taut one [106]. Compliant moorings present similar characteristics with the catenary system but can be deployed with less space and less disturbance to the seabed. In any case, if a catenary system is implemented within a significant varying water level, special attention must be paid in the design process as the behavior and in particular the stiffness of these mooring lines will constantly change. This consequently may lead to potential snatch loads which are impulse mooring loads, with higher amplitude than the static and dynamic mooring loads. Snatch or snap loads can occur when a mooring becomes slack and then suddenly is re-tensioned.

Additional options for a catenary system is the inclusion of clump weights and jumpers. Such a system for the mooring configuration of a Wave Energy Converter (WEC) was investigated by [36]. It was found that the mooring pre-tension has a great impact on the mean displacement in surge due to wave drift effects and therefore on the survivability conditions.
Different type of mooring configurations are presented in Figure 1.6 and include both rigid and floating solutions.

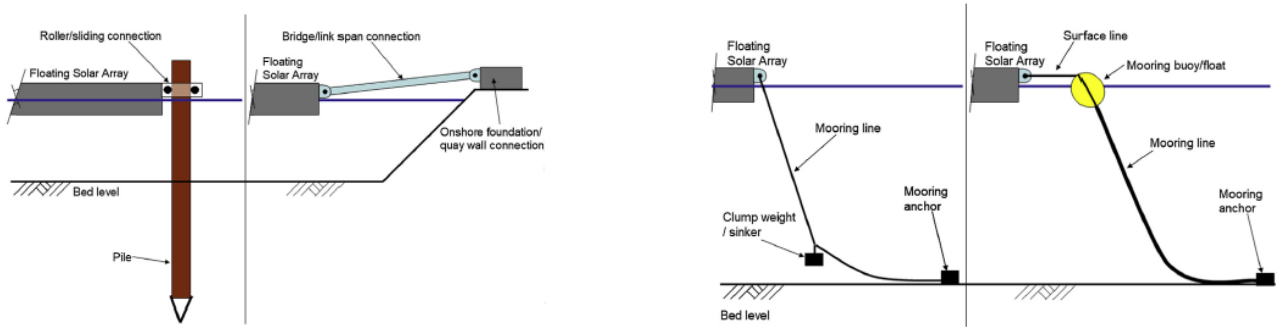

(a) Examples of rigid mooring systems

(b) Examples of floating mooring systems

Figure 1.6: Typical mooring configurations[106]

In a case study in mid-western Taiwan, the tidal variations imposed an average 2.5m water level fluctuation. The FPV was moored by catenary stud-less mooring lines and both numerical and experimental simulations were carried out to analyze the motions of the system. The instantaneous peaks in the mooring tension occurred during wave conditions close to the resonance frequency of the floating platform in surge and pitch motions [111].
Three-dimensional potential theory followed by numerical methods can be used to investigate the response of an FPV array under the effect of different environmental loads. This can be wave only, wind only, current only and then their combined effect. The wind load has been shown to be dominant for the mooring tension and displacement of an FPV array moored by 124 V-shaped lines for an average water depth of 10m [113].
Moreover, numerical methods based on diffraction/radiation theory can be used as well for the design of the mooring system. Such an approach was adopted in [40] where superflex wire ropes were proposed for the installation of a WEC in ultra-shallow water depths. An overall reduction of the mooring material, the length of the mooring line and the mooring radius was achieved by incorporating the superflex rope due to its elastic energy storage. However, long term economic and environmental aspects should be further investigated.
An anchor-tension type mooring system, fixed with a chemical anchor and cable to the wall of the waterway was selected for the case of a waterway to be able to deal with small water level fluctuations [56].
Other fields of research on the mooring configuration have been optimization techniques [60] and identification of the trends of the hardware mooring costs with respect to water variations [41]. Finally, the topic of implementing FPV system in irrigation reservoirs with the object of reducing the water evaporation while generation electrical power has been widely studied [83, 88]. These cases present similar behavior with the ELS of Delta21 since the reservoirs are subject to high water level variations.

1.5.5 Wind Turbine Foundation

Until now, many different types of wind turbine foundations have been investigated and installed in existing projects. All the types fall within two categories: fixed and floating substructure. The first category consists of monopiles, gravity based structures (GBS), tripods and jackets, while the latter consists of semi-submersibles, tension leg platforms (TLP) and spar-buoys (Figure 1.7).

Figure 1.7: Different types of foundation (Illustration by Joshua Bauer,NREL)

For the specific environmental conditions of Delta21 lake, floating solutions will be not discussed, since the minimum water level of 1.5m within the lake wouldn't be sufficient for the required draft.

During the early stages of offshore wind development, the majority of the support structures were gravity based such as Vindeby (1991), Tunø Knob (1995), Middelgrunden (2001), Nysted (2004) and Sprogø (2009) in Denmark, Lillgrund (2008) in Sweden, and Thorntonbank (2009) and Belwind (2011) in Belgium [51].

As stated in [8], the most attractive solutions for up to 30m of water depth are monopiles, jackets and gravity based structures (GBS). However, in economical terms, GBS is the most cheap solution since concrete is cheaper than steel. In contrast, due to the large volume of concrete needed to support a wind turbine, GBS could lead to limitations of required vessels for transportation. It is therefore becoming clear, that the size of the required slab is critical for the selection of the specific foundation.

Moreover, in [89] it is also stated that for distances less than 15-20 km from the shore, GBS are more widely used.

Qian et al. [82] studied the behavior of a piled beam-slab foundation in sand onshore under different loads, by performing experimental analysis on a scaled model. The main outcome of the study was that the vertical loads increase the horizontal bearing capacity of the slab.

A gravity caisson foundation consisted of a central tower and a bottom caisson with a larger diameter was proposed in [15]. The study focused on the towing and the positioning of the foundation using backfill of sand on soft seabed, in a water depth of 21m.

Whitehouse et al. [105] evaluated the scour of gravity base foundations and highlighted the need of integrating these considerations into the life cycle management.

1.5.6 Parameter Selection

The presentation of the most relevant components in the design of a wind-PV park within the ESL of Delta21 and the relevant available literature has been attempted in Section 1.5.

The first three components, namely optimization, electrical infrastructure and shadow effects, are mostly connected with the performance of the hybrid system. They are important aspects when the maximization of the energy yield and the minimization of the costs are being seeked but this can be performed during a later stage of the design.

The technical feasibility of such a combined farm is first and foremost depending on the viability of the structural components. These are the mooring configuration for the FPV panels and the substructure for the wind turbines. GBS have been implemented in various projects and locations and have proven their reliability.However, the effect of the water fluctuation and the corresponding dynamic analysis of the tower must be further investigated.

On the other hand, a floating system and the corresponding mooring configuration that must be capable to cope with 11m difference in water level is something new and challenging. Even though a large variety in studies regarding mooring systems exist, the analysis of the mooring systems of FPV has not been sufficiently explored yet. Next to that, the energy storage function of the lake generates an environment which tests the application of floating panels.

The purpose of this study is therefore dedicated to the investigation of a suitable mooring configuration. In any case, there are definitely more components and aspects that have to be checked to have a solid understanding of the feasibility of such a hybrid power plant. However, the results of the project can be used as input for future studies that will look into other directions.

1.5.7 Further Considerations

Another potential synergy for this specific hybrid park is the integration of the mooring lines with the wind turbines foundation.

In order to minimize the effect of the mooring system on the seabed and keep the mooring footprint as low as possible, the mooring lines could be anchored on the wind turbine substructures.

This would consequently lead to lower costs for the mooring of the solar panels but the capability of the GBS to withstand also the tension from the moorings should be further checked. In this way, a logical sequence is created with regards to the feasibility of the whole system.

The most critical parameter as discussed earlier is the feasibility of the floating panels. With the environmental loads as input, the corresponding line tension can be calculated by taking into account the different water levels within the lake. Again, the environmental loads and the line tension would be the input for the structural response and stability of the foundation. In later stages, the optimization aspects of the system could be further investigated but only after proving and checking the technical feasibility.

1.6 Research Question

This study aims to investigate the possibility of using the wind turbine towers as anchoring points for the floating solar boats. It is important to consider what the advantages of such an approach over a conventional seabed anchoring would be.

- Reduced overall length of mooring lines; potentially leading to lower cost for the mooring system
- Reduced mooring footprint; enhanced usage of space
- Zero disturbance of the seabed
- At this early design stage, such a system seems promising to deal with the large water fluctuation
- A novel design that to the knowledge of the author has not been investigated until now
- Introducion of a new component to the synergy of offshore hybrid wind and solar parks

The main question that this thesis will answer is the following:

How large would the mooring force be if the towers of the wind turbines are used as anchoring points for the floating solar units within the ESL of Delta21?

1.7 Scope of the research

The exact configuration of the mooring system is not required to be determined at the beginning of the analysis. The boundaries of the system are that there are available bottom founded wind turbines in the perimeter of the floating solar plants that can be used for the anchoring. This study is focused exclusively for the energy storage lake of Delta21 and the environmental data that have been gathered from available data-set or calculated during other projects.

This project uses assumptions and rough estimates for the foundation of the wind turbines rather than analytical calculations due to the limited time frame for the completion of the project. In addition, environmental

considerations due to the impact of either wind turbine foundations or the coverage of the lake with solar units are disregarded.

The purpose of the project is to make estimates of the second order wave drift force of the floating solar panels. The initial step is breaking down the existing solar boat that GroenLeven is deploying, to smaller and easier to handle blocks.

Lastly, the results of this thesis can be used only as a first indicator of whether or not the proposed mooring configuration is feasible. Crucial aspects that have to be investigated further are the economic impact of such a system and the technical design of the connection point, suitable adjusted to follow the water fluctuations. In later stages, the length of the mooring lines can be looked in deeper after the optimization of the HPP layout based on energy output and the limitation of shadowing effects.

1.8 Approach

The floating solar units are composed of multiple rows and columns of solar boats. The problem can therefore be broken down to smaller and easier to deal with blocks. The first block is a single solar boat which can be again divided into smaller components. So, the main unit that will be studied is the floating solar boat of GroenLeven which has three main elements: the inclined solar panels, the metallic frame and four plastic floaters. The model will start from a single floater and will gradually develop to reach four floaters mechanically connected with each other.

The two main forces acting on a solar boat are the wave forces on the submerged part of the floaters and the wind forces acting on the solar panels and the part of the floaters above the waterline. For the calculation of the latter, analytical calculations can yield accurate results while for the first one the far-field approach will be adopted for the calculation of horizontal forces. One step earlier, linear potential theory will be used for the calculation of the required first order wave motions. Finally, the estimations of the forces of a single boat can be expanded with proper assumptions to a whole solar floating unit.

The final step towards answering the main research question is the comparison of the mooring force that the proposed configuration would imply with the forces acting already on the wind turbine. The wind forces are given as input from Dutch Wind Design while analytical formulas will be used for the estimation of wave and current forces on the submerged part of the tower.

1.9 Structure of the Thesis

This report contains the theory, implementation and validation of the method developed. The detailed structure of the report is as follows.

Chapter 2 presents the background of linear potential theory, the boundary element method, the structural theory used for the mechanical connection of the model and the available approaches to the second order wave forces. An overview of the model and the methodology followed in this project is given in Chapter 3. In Chapter 4, four different validation cases are presented to check the reliability of the model and the produced results. Chapter 5 presents the results obtained from the developed model. A discussion of these results is provided in Chapter 6 whereas conclusions are drawn in Chapter 7. Finally, recommendations for further investigation and work are included in Chapter 8.

2 | Theory

In this chapter, the theory used for the implementation of the model is presented. More specifically, it covers the linear potential theory, the boundary element method and the approaches for the calculation of second order drift forces.

2.1 Selection of method

The hydrodynamic forces on a floating body can be calculated with the use of multiple methods. The first and simplest method is the Morison equation which is able to calculate the drag and inertial forces on the body. Sarpkaya [90] tried to give a thorough understanding of the origins and the limitations in the use of Morison equation for the calculations of forces on offshore structures.

Additionally, forces can be calculated after the description of any flow field, which can be achieved by two governing methods/approaches. The first one which is the most complete is given by the viscous Navier-Stokes equation. These equations can be solved by Computational Fluid Dynamics (CFD), but it is restricted by a very high computational cost. It is unsurprising that if the accuracy of the solution is reduced, then the computational time can be attenuated as well. In such a case, the accuracy can be reduced but still remain efficient by introducing certain assumptions and simplifications.

And this is where the second method, linear potential flow theory, comes into play. The main simplifications that this method is adopting are that viscosity and viscous effects are not relevant to the problem considered. In order to make use of the potential flow theory, small deformations and rotations of the structure can only be considered.
Every theory or approach is valid within certain regions, as presented in Figure 2.1.

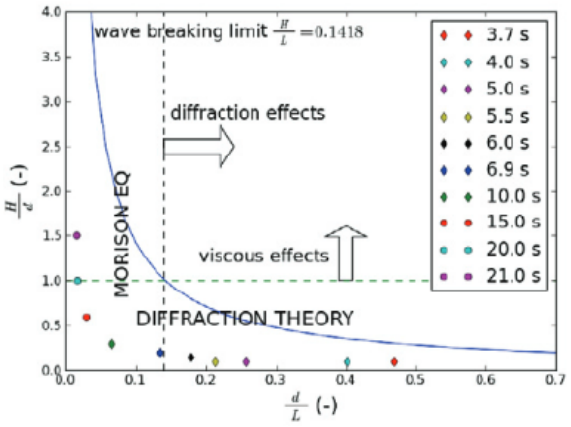

Figure 2.1: Potential theory and Morison equation validity regions (x-axis:d/L, y-axis H/d) [49]

For this thesis, the analysis include multiple floating bodies in close proximity and the diffraction effects have to be taken into account, excluding consequently the simple use of Morison's equation. Moreover, at this early stage of the design, estimations on the forces are more important rather than precise results followed by high computational time. Therefore, the linear potential theory is used for this project.

2.2 Linear Potential Flow Theory

As mentioned earlier and can be also found in [52], the main assumptions that potential flow method is adopting and regard the basic properties of the flow can be summarized into the following:

- The flow is non-viscous
- The flow is irrotational

- The flow is incompressible

Using the assumption that the fluid is incompressible and by applying the continuity principle for a control volume V, the continuity equation can be given by Equation 2.1.

$$\frac{\partial u}{\partial x} + \frac{\partial v}{\partial y} + \frac{\partial w}{\partial z} = 0 \tag{2.1}$$

In this equation, u,v and w are the components of the velocity of the flow $(\vec{V})$ in three directions, x,y and z respectively.

The other two assumptions; those of irrotational and non-viscous fluid, can be used to describe the motions of the water by the velocity potential function (Φ). This potential function (Φ), associated with a potential flow field, is actually a mathematical expression that has the property that at any point in the flow, the velocity component in any direction is just the derivative of this function in the chosen direction. Equation 2.2 is describing the aforementioned relationship.

$$u = \frac{\partial \Phi}{\partial x}, v = \frac{\partial \Phi}{\partial y}, w = \frac{\partial \Phi}{\partial z} \tag{2.2}$$

If ∇ is used as a collective term for all the first order derivatives in the corresponding x,y and z direction, the substitution of Equation 2.2 into Equation 2.1 yields the Laplace Equation (Equation 2.3).

$$\frac{\partial \Phi^2}{\partial x^2} + \frac{\partial \Phi^2}{\partial y^2} + \frac{\partial \Phi^2}{\partial z^2} = \nabla^2 \Phi = 0 \tag{2.3}$$

The potential must also satisfy the next three boundary conditions:

1. If (S) is the surface of the body, then the boundary condition at any point of the surface $(S(x, y, z))$ is expressed as:
$$\frac{\partial \Phi}{\partial n} = v_n \tag{2.4}$$
with v_n being the outward normal velocity at the submerged surface of the body, defined as positive in the direction of the fluid. This condition plays a very important role as it dictates that the normal velocity of any water particle at the surface of the body will be equal to the normal velocity of this watertight body itself.

2. It is necessary to guarantee that no fluid permeates through the sea bed and this implies the sea bottom boundary condition at $z = -\infty$:
$$\frac{\partial \Phi}{\partial z} = 0 \tag{2.5}$$

3. The linearized combined kinematic and dynamic free surface boundary condition at z=0. At z=0 the vertical velocity of the free surface is equal to the vertical motion of the fluid (kinematic). In addition, at z=0 the pressure above the free surface is constant and equal to zero (dynamic). The combination of the kinematic and dynamic free surface boundary conditions after differentiation of the dynamic and substitution of the kinematic yields:
$$\frac{\partial \Phi}{\partial z} - \frac{\omega^2}{g} \Phi = 0 \tag{2.6}$$
with, ω being the wave frequency expressed in $[rad/s]$ and g the gravity acceleration expressed in $[m/s^2]$.

Besides the boundary set of the three boundary conditions, the linearization of the problem, which seeks to make it simpler, introduces two additional assumptions. These linearization assumptions as described by [33] are:

- The ratio of wave height to wavelength (also referred as wave steepness) and the ratio of wave height to water depth must be significantly smaller than 1.
- The motions of the floating body are small and around a fixed mean position: the amplitude of the motions over the dimensions of the body should also be significantly smaller than 1.

According to [52, 103], when a floating body is exposed to an incident wave field, the interaction between those two can be divided into the following phenomena:

- The incident wave is causing changes in the pressure field around the still body. This phenomenon is captured by the velocity potential of the incident wave (Φ_0).

- The incident wave is reflected due to the presence of the floating body. The occurring diffracted waves exert fluid pressure forces which consequently affect the motion of the body in a way that is described by the diffraction potential (Φ_7).

- As the floating body in waves is oscillating, it generates radiation waves which once again exert fluid pressure forces on the body. These forces are taken into consideration through the radiation potential (Φ_{1-6}).

In regular waves, a linear potential Φ, which is a function of the earth-fixed coordinates and of time t, can be written as a product of a space-dependent term and a harmonic time-dependent term as follows [52]:

$$\Phi(x, y, z; t) = \phi(x, y, z) \cdot e^{-i\omega t} \tag{2.7}$$

The three aforementioned potentials can be combined to describe the total velocity potential in the vicinity of the floating body. The space-dependent part of the complex potential Φ follows from the superposition of these potentials and is given by Equation 2.8. Once again, the assumptions for the potential flow and linearized boundary conditions as well as the steady-state interaction of the body with a regular wave in deep water are adopted.

$$\phi = -i\omega\{(\phi_0 + \phi_7)\zeta_0 + \sum_{j=1}^{6} \phi_j \zeta_j\} \tag{2.8}$$

where, ϕ_j is associated with the j-modes of motion of the body (j=1-6).

Substituting the radiation potential into the hull boundary condition (Equation 2.4) the following relationship is true:

$$\frac{\partial \phi_{1-6}}{\partial n} = v_{nk} \tag{2.9}$$

As far as the undisturbed and diffraction potential are concerned, once again it should be guaranteed that the hull is water tight. It must be reminded that in the linear approach adopted here, the motions of the body are completely ignored while considering the wave excitation forces. Therefore, the fluid velocity in the normal direction to the hull due to the undisturbed wave potential plus the the diffraction potential should be zero. As a result, Equation 2.10 is valid.

$$\begin{aligned} \frac{\partial \phi_0}{\partial n} + \frac{\partial \phi_7}{\partial n} &= 0 \\ \frac{\partial \phi_0}{\partial n} &= -\frac{\partial \phi_7}{\partial n} \end{aligned} \tag{2.10}$$

The fluid pressure follows from the Bernoulli equation and is given by Equation 2.11 and has two components: the first component expresses the hydrodynamic pressure while the second one the hydrostatic pressure and they both depend on the density of the fluid.

$$\begin{aligned} p(x, y, z; t) &= -\rho \frac{\partial \Phi}{\partial t} - \rho g z \\ &= -\rho(\frac{\partial \Phi_0}{\partial t} + \frac{\partial \Phi_7}{\partial t} + \frac{\partial \Phi_{1-6}}{\partial t}) - \rho g z \end{aligned} \tag{2.11}$$

Figure 2.2 gives an overview of the motions of a floating rigid body in all 6 degrees of freedom; with length L, width B, total height H and draft D.

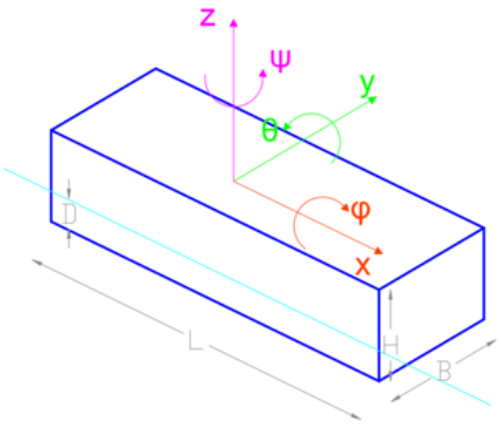

Figure 2.2: Definition of the axis system and degrees of freedom for a floating rigid body

The 6 degrees of freedom correspond to the following naming as mostly met in the literature of floating structures: displacement in the direction of x-axis is called surge (j=1), displacement in the direction of y-axis is called sway (j=2), displacement in the direction of x-axis is called heave (j=3), positive right hand rotation about x-axis is called roll (j=4), positive right hand rotation about y-axis is called pitch (j=5), positive right hand rotation about z-axis is called yaw (j=6).

Now, the forces and the moments acting on the body (in all 6 directions) can be distinguished into two components as explained earlier: the first order wave exciting hydrodynamic forces and moments, described by Equation 2.12 and the oscillating hydrodynamic forces and moments, described by Equation 2.13.

$$\begin{aligned} X_k &= -\iint_{S_0} p n_k \cdot dS_0 \\ &= -\rho\omega^2 \zeta_0 e^{-i\omega t} \iint_{S_0} (\phi_0 + \phi_7) n_k \cdot dS_0 \end{aligned} \tag{2.12}$$

$$\begin{aligned} F_k &= -\iint_{S_0} p n_k \cdot dS_0 \\ &= -\rho\omega^2 \sum_{j=1}^{6} \zeta_j e^{-i\omega t} \iint_{S_0} \phi_j n_k \cdot dS_0 \end{aligned} \tag{2.13}$$

Where:

S_0= mean wetted surface of the body

n_k= direction cosine of surface element dS_0 for the k-mode

$k = 1, 2, 3$ corresponds to forces and $k = 4, 5, 6$ corresponds to moments

The generalized direction cosines on S_0 are defined as follows:

$$\begin{aligned} &surge : n_1 = cos(n, x) \\ &sway : n_2 = cos(n, y) \\ &heave : n_3 = cos(n, z) \\ &roll : n_4 = (r \times n)_1 = y n_3 - z n_2 \\ &pitch : n_5 = (r \times n)_2 = z n_1 - x n_3 \\ &yaw : n_6 = (r \times n)_3 = x n_2 - y n_1 \end{aligned} \tag{2.14}$$

Now, an oscillatory motion (in a complex notation) can be described by Equation 2.15.

$$s_j = s_{a_j} e^{-i\omega t} \tag{2.15}$$

It naturally follows that the velocity and the acceleration of this oscillation are given by Equations 2.16 and 2.17.

$$\dot{s}_j = v_j = -i\omega s_{a_j} e^{-i\omega t} \tag{2.16}$$

$$\ddot{s}_j = \frac{\partial v_j}{\partial t} = -\omega^2 s_{a_j} e^{-i\omega t} \tag{2.17}$$

The corresponding hydrodynamic forces and moments can be split into a load in phase with the velocity and a load in phase with the acceleration as shown in Equation 2.18.

$$\begin{aligned} F_k &= -M_{kj}\ddot{s}_j - N_{kj}\dot{s}_j \\ &= (s_{a_j}\omega^2 M_{kj} + i s_{a_j}\omega N_{kj}) e^{-i\omega t} \\ &= (-s_{a_j}\omega^2 \rho \iint_{S_0} \phi_j n_k \cdot dS_0) e^{-i\omega t} \end{aligned} \tag{2.18}$$

The last part is similar to the right hand side of Equation 2.13, where $s_{a_j} = \zeta_j$. So, in the case of an oscillation of the body in direction j with a velocity potential ϕ_j, the hydrodynamic added mass and damping (coupling) coefficients are defined by Equation 2.19 as follows:

$$\begin{aligned} a_{kj} &= -Re[\rho \iint_{S_0} \phi_j n_k \cdot dS_0] \\ b_{kj} &= -Im[\rho\omega \iint_{S_0} \phi_j n_k \cdot dS_0] \end{aligned} \tag{2.19}$$

Both matrices are symmetric which means that the following symmetric relations hold (Equation 2.20):

$$\begin{aligned} a_{kj} &= a_{jk} \\ b_{kj} &= b_{jk} \end{aligned} \tag{2.20}$$

2.3 Boundary Element Method

The boundary element method (BEM) is a method which allows for the calculation of the hydrodynamic coefficients and forces that were described in Section 2.2.
In a fluid domain, the velocity potential at any point of the domain can be characterized in terms of a surface distribution of sources (Equation 2.21).

$$\phi(\vec{x}) = \frac{1}{4\pi} \int \sigma(\vec{x_s}) G(\vec{x}, \vec{x_s}) dS \tag{2.21}$$

where,

- $G(\vec{x}\vec{x_s})$ is the Green function
- $\vec{x_s}$ is a point on the body surface S
- $\sigma(\vec{x_s})$ is the unknown source distribution

The Green's function helps solving linear inhomogeneous partial differential equations. It satisfies all boundary conditions except from the normal velocity boundary condition on the surface of the structure as described by Equation 2.4.
As a consequence, the source strength can be solved using the boundary condition as described by Equation 2.22.

$$-\frac{1}{2}\phi(\vec{x}) + \frac{1}{4\pi} \int_{S_b} \frac{G(\vec{x}, \vec{x_s})}{\vec{n_x}} \phi(x) dS = v_n(\vec{x}) \tag{2.22}$$

A numerical approach to Equation 2.22 would be to describe the shape of the submerged hull by flat panels. Each one of this panel could then have a constant source strength σ. After that, a point per panel should be chosen where the boundary condition will be satisfied. And this point is called the collocation point named m. The normal derivative of the potential at location m can then be described as follows (Equation 2.23):

$$\frac{\partial \phi_m}{\partial n} = -\frac{1}{2}\sigma_m + \frac{1}{4\pi}\sum_{n=1}^{N}\sigma_n \cdot \frac{\partial G_{mn}}{\partial n}\Delta S_n \tag{2.23}$$

where n indicates the location of all the panels (with their strengths σ_n and areas ΔS_n) except panel m.

By substituting Equation 2.9 and 2.10 into Equation 2.23, the following formulas can be developed.

For the diffraction potential:

$$-\frac{1}{2}\sigma_7(x,y,z) + \frac{1}{4\pi}\sum_{n=1}^{N}\sigma n_7 \cdot \frac{\partial G_{mn}}{\partial n}\Delta S_n = -(\frac{\partial \phi_0}{\partial n})_m \tag{2.24}$$

For the radiation potential:

$$-\frac{1}{2}\sigma_{1-6}(x,y,z) + \frac{1}{4\pi}\sum_{n=1}^{N}\sigma n_{1-6} \cdot \frac{\partial G_{mn}}{\partial n}\Delta S_n = n_{1-6}(x_m, y_m, z_m) \tag{2.25}$$

Equations 2.24 and 2.25 show that every panel m has an expression for the boundary condition at that panel m and is affected by two components: the source sheet at panel m itself and the other source sheets on all remaining panels.
Since there are N panels with their collocation points, there are in total N number of these equations. And since each panel has its own source strength, a $N \times N$ system of equation occurs.
Starting with the diffraction potential, the system of equations to be solved for solving the source strengths is given by Equation 2.26.

$$\begin{pmatrix} A_{11} & \cdots & A_{1N} \\ \vdots & \ddots & \vdots \\ A_{N1} & \cdots & A_{NN} \end{pmatrix} \cdot \begin{pmatrix} \sigma_{1,7} \\ \vdots \\ \sigma_{N,7} \end{pmatrix} = \begin{pmatrix} -(\frac{\partial_0}{\partial n})_1 \\ \vdots \\ -(\frac{\partial_0}{\partial n})_N \end{pmatrix} \tag{2.26}$$

Where,

- $A_{nn} = -\frac{1}{2}$ (influence of source at panel n on $\frac{\partial \phi_7}{\partial n}$ at its own collocation point)
- $A_{mn} = -\frac{1}{4\pi}\frac{\partial G_{mn}}{\partial n}\Delta S_n$ (influence of source at panel n on $\frac{\partial \phi_7}{\partial n}$ at collocation point m)
- $\sigma_{n,7}$ is the unknown source strength of the diffraction potential at panel n

The same relationships can be generated for the radiation potential as described by Equation 2.27.

$$\begin{pmatrix} A_{11} & \cdots & A_{1N} \\ \vdots & \ddots & \vdots \\ A_{N1} & \cdots & A_{NN} \end{pmatrix} \cdot \begin{pmatrix} \sigma_{1,j} \\ \vdots \\ \sigma_{N,j} \end{pmatrix} = \begin{pmatrix} (n_j)_1 \\ \vdots \\ (n_j)_N \end{pmatrix} \tag{2.27}$$

Where,

- j indicates which radiation potential is considered: $j = 1..6$
- $A_{nn} = -\frac{1}{2}$ (influence of source at panel n on $\frac{\partial \phi_j}{\partial n}$ at its own collocation point)
- $A_{mn} = -\frac{1}{4\pi}\frac{\partial G_{mn}}{\partial n}\Delta S_n$ (influence of source at panel n on $\frac{\partial \phi_j}{\partial n}$ at collocation point m)
- $\sigma_{n,j}$ is the unknown source strength of the radiation potential at panel n
- $(n_j)_m$ is the local direction due to motion in direction j at panel m described by Equation 2.14

2.4 Equation of Motion

As was described in Section 2.2, a single body exposed to waves has 6 degrees of freedom (DoF) which correspond to 3 translations along the main axes and 3 rotations around these axes. The response of the body can be described by the equation of motion which gives the motion in all 6 degrees of freedom. According to [52], Newton's second law can be used to derive the equation of motion for a body in waves around it's center of gravity (CoG). It is also assumed here that both the total mass of the body and the mass distribution over the body are constant.
The translational motions of the CoG are described by Equation 2.28 while the rotational motions around the CoG are given by Equation 2.29.

$$\vec{F} = \frac{\partial}{\partial t}(m\vec{U}) \tag{2.28}$$

$$\vec{M} = \frac{\partial}{\partial t}(\vec{H}) \tag{2.29}$$

Where,

- $\vec{F}$ is the external force acting on the CoG [N]
- m is the mass of the rigid body [kg]
- $\vec{U}$ is the instantaneous velocity of the CoG [m/s]
- $\vec{M}$ is the external moment acting around the CoG [Nm]
- $\vec{H}$ is the instantaneous angular momentum about the the CoG [Nms]
- t is the time [s]

The adopted potential linear theory is allowing to consider the motions of the body in waves, as a superposition of the motions of the body in still water and the forces of the constrained body exposed to incoming waves.
As a result, the first component yields hydromechanical forces and corresponding moments that are induced by the harmonic oscillations of the body moving in still water. While the second component yields wave exciting forces as exerted by the waves on the restrained body.

Starting with the latter, the wave exciting forces and their resulting moments, that the body is experiencing due to the undisturbed incoming wave can be further analyzed into two components as shown in Equation 2.30.

$$F_w = F_{FK} + F_d \tag{2.30}$$

Where,

- F_w is the wave exciting force
- F_{FK} is the Froude-Krylov force
- F_d is the diffraction force

The Froude-Krylov force comes after the direct integration of the hydrodynamic wave pressure over the body's submerged surface. However, a part of the wave is diffracted and therefore a correction is needed. This correction is implemented through the diffraction force.
Revisiting the hydromechanical forces resulting from the harmonic oscillations of the body in still water, they can be divided into two parts: a hydrostatic and a hydrodynamic part. The hydrostatic part is the force acting on the body due to its displaced position and can be determined via Equation 2.31.

$$F_{h,static} = -cu(\omega) \tag{2.31}$$

Where, c is the hydrostatic stiffness matrix and is connected to the buoyancy of the body and u is the frequency dependent displacement in all DoF. For a body in waves with 6 DoF and double symmetry, the hydrostatic stiffness matrix **C** is a 6x6 matrix and can be described by Equation 2.32. For free floating bodies, which is the case for the floating solar boat in this analysis, the restoring spring terms are only present for heave, roll and pitch.

$$\boldsymbol{C} = \begin{bmatrix} 0 & & & & & & \\ & 0 & & & & & \\ & & c_{33} & & & & \\ & & & c_{44} & & & \\ & & & & c_{55} & & \\ & & & & & 0 & \end{bmatrix} \tag{2.32}$$

And the individual components are given by Equations 2.33-2.35.

$$c_{33} = \rho g A_{wp} \tag{2.33}$$

$$c_{44} = \rho g \nabla G M_{roll} \tag{2.34}$$

$$c_{55} = \rho g \nabla G M_{pitch} \tag{2.35}$$

Where:

- A_{wp} is the water-plane area
- ∇ is the water displacement
- GM_{roll} is the transverse metacentric height
- GM_{pitch} is the longitudinal metacentric height

The oscillations of the body also result into a hydrodynamic force. As was shown in Equation 2.18, this hydrodynamic force can be also expressed by Equation 2.36.

$$F_{h,dyn} = \omega^2 \boldsymbol{A}(\omega) u - i\omega \boldsymbol{B}(\omega) u \tag{2.36}$$

Where **A** and **B** are the added mass and damping matrices respectively as calculated by Equation 2.19. It should be noted that both of these matrices are depending on the frequency of the oscillations.

For a single body with the usual 6 DoF, the added mass and damping matrices will result in a 6x6 matrix at every frequency. This is illustrated by Equations 2.37 and 2.38.

$$\boldsymbol{A}(\omega) = \begin{bmatrix} a_{1,1}(\omega) & \cdots & a_{1,6}(\omega) \\ \vdots & \ddots & \vdots \\ a_{6,1}(\omega) & \cdots & a_{6,6}(\omega) \end{bmatrix} \tag{2.37}$$

$$\boldsymbol{B}(\omega) = \begin{bmatrix} b_{1,1}(\omega) & \cdots & b_{1,6}(\omega) \\ \vdots & \ddots & \vdots \\ b_{6,1}(\omega) & \cdots & b_{6,6}(\omega) \end{bmatrix} \tag{2.38}$$

After defining all the relevant components, the total equation of motion for a single body with 6 degrees of freedom floating in waves is given by Equation 2.39.

$$\tilde{u}(\omega)(-\omega^2(\boldsymbol{M} + \boldsymbol{A}(\omega)) + i\omega \boldsymbol{B}(\omega) + \boldsymbol{C}) = \tilde{F_w}(\omega) \tag{2.39}$$

Where,

- $\tilde{u}$ is the complex motion vector, $\tilde{u}(\omega) = \begin{bmatrix} \tilde{x} & \tilde{y} & \tilde{z} & \tilde{\phi} & \tilde{\theta} & \tilde{\psi} \end{bmatrix}^T$
- $\boldsymbol{M}$ is the mass matrix (6x6)
- $\boldsymbol{A}$ is the added mass matrix (6x6)
- $\boldsymbol{B}$ is the hydrodynamic damping matrix (6x6)
- $\boldsymbol{C}$ is the hydrostatic stiffness matrix (6x6)
- $\tilde{F_w}$ is the complex wave exciting force and moment vector

2.5 Two Floating Connected Bodies

The theory introduced for a single floating body presented until now can be further extended to a system of two floating bodies mechanically connected with each other [96]. Figure 2.3 presents the configuration adopted for this project, for the case of two interconnected bodies.

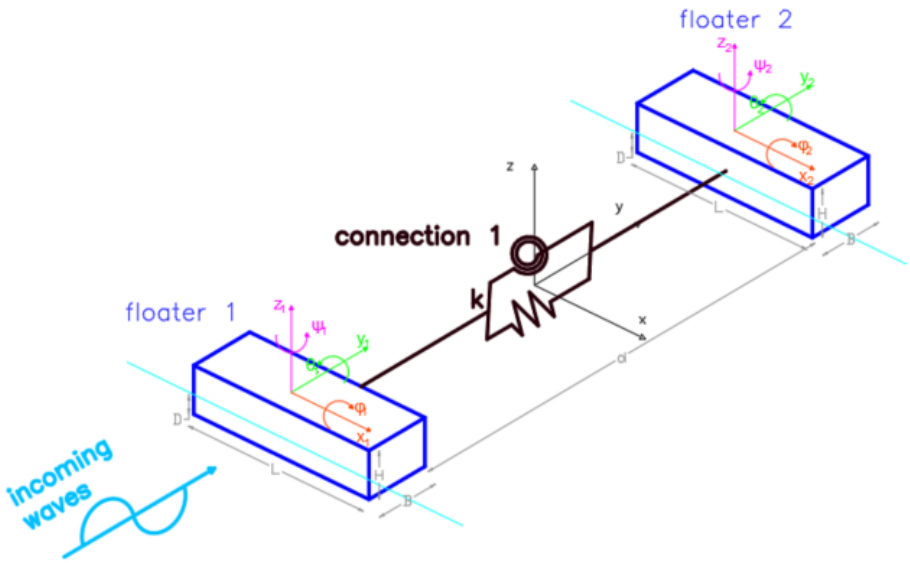

Figure 2.3: Configuration of two interconnected floating bodies

The two bodies are considered rigid, they have the same dimensions and these are: length L, width B, total height H and draft D. They are placed in a distance d and are connected with 3 translational and 3 rotational springs with spring stiffness k. The connection point for both floaters is set to be at the waterline and exactly at half of the length. Three system of coordinates can be distinguished as well: a global system of coordinates in the middle point of the connection and two local coordinate systems at the center of gravity of each floater. Each floater is subjected to 6 DoF denoted as $x_{1,2}$, $y_{1,2}$, $z_{1,2}$, $\phi_{1,2}$, $\theta_{1,2}$ and $\psi_{1,2}$. The incoming waves are perpendicular to the largest dimension of the floaters and are called beam waves.
The connection introduces a new component to the equation of motion and this is the connection stiffness matrix denoted as $\boldsymbol{K_{conn}}$. The purpose of this matrix is to couple the relative motions between the two floaters as transferred through the connection points. This approach was also used in [49]. Since this system entails 6+6 DoF, the $\boldsymbol{K_{conn}}$ will be a linear 12x12 matrix. For the determination of each individual entry, the Euler-Lagrange method will be used.
The potential energy for the system of 6 springs and two connection points can be described by Equation 2.40.

$$V = \frac{1}{2}(k_x(\Delta x_c)^2 + k_y(\Delta y_c)^2 + k_z(\Delta z_c)^2 + k_\phi(\Delta \phi_c)^2 + k_\theta(\Delta \theta_c)^2 + k_\psi(\Delta \psi_c)^2) \tag{2.40}$$

Where the relevant displacement is given be Equation 2.41.

$$\begin{aligned}
\Delta_{x,c} &= x_{1,c} - x_{2,c} \\
\Delta_{y,c} &= y_{1,c} - y_{2,c} \\
\Delta_{z,c} &= z_{1,c} - z_{2,c} \\
\Delta_{\phi,c} &= \phi_{1,c} - \phi_{2,c} \\
\Delta_{\theta,c} &= \theta_{1,c} - \theta_{2,c} \\
\Delta_{\psi,c} &= \psi_{1,c} - \psi_{2,c}
\end{aligned} \tag{2.41}$$

The location of the connection point with respect to the local coordinate system of each floater can be expressed by the location matrices as presented in Equation 2.42.

$$\begin{bmatrix} x_{c,1} \\ y_{c,1} \\ z_{c,1} \end{bmatrix} = \begin{bmatrix} 0 \\ B/2 \\ 0 \end{bmatrix} \qquad \begin{bmatrix} x_{c,2} \\ y_{c,2} \\ z_{c,2} \end{bmatrix} = \begin{bmatrix} 0 \\ -B/2 \\ 0 \end{bmatrix} \tag{2.42}$$

The relative displacement of each connection point after the translations and rotations of the two floaters can be described by Equation 2.43.

$$u_{c,i} = \begin{bmatrix} x_{c,i} \\ y_{c,i} \\ z_{c,i} \\ \phi_{c,i} \\ \theta_{c,i} \\ \psi_{c,i} \end{bmatrix} + R_{\phi,\theta,\psi} \begin{bmatrix} x_{c,i} \\ y_{c,i} \\ z_{c,i} \end{bmatrix} - \begin{bmatrix} x_{c,i} \\ y_{c,i} \\ z_{c,i} \end{bmatrix} \tag{2.43}$$

Where $i = 1, 2$ denotes the number of the floater and $R_{\phi,\theta,\psi}$ is the rotation matrices for the 3 respective rotations.
According to the Euler-Lagrange method, the connection stiffness matrix $\boldsymbol{K_{conn}}$ is described by Equation 2.44.

$$K_{conn}(u_j) = \frac{\partial V}{\partial u_j} \tag{2.44}$$

Where V is the kinematic potential as given in Equation 2.40 and $j = 1..12$ corresponds to each and every DoF.
In order to obtain the final form of the connection stiffness matrix, the following linearization assumptions are adopted:

- small angle approximation: $sin(\theta) = \theta$ and $cos(\theta) = 0$
- quadratic terms of the degrees of freedom are set to zero
- multiplications of the form $u_j \cdot sin(u_i)$, where i, j are different degrees of freedom, are also set to zero

Taking all the above into consideration, the 12x12 $\boldsymbol{K_{conn}}$ for the case of two connected floating bodies and the layout of Figure 2.3 can be calculated as follows:

$\boldsymbol{K_{conn}}$= 2·

$$\begin{bmatrix}
k_x & 0 & 0 & 0 & 0 & -\frac{B}{2}k_x & -k_x & 0 & 0 & 0 & 0 & -\frac{B}{2}k_x \\
0 & k_y & 0 & 0 & 0 & 0 & 0 & -k_y & 0 & 0 & 0 & 0 \\
0 & 0 & k_z & \frac{B}{2}k_z & 0 & 0 & 0 & 0 & -k_z & \frac{B}{2}k_z & 0 & 0 \\
0 & 0 & \frac{B}{2}k_z & k_\phi + \frac{B^2}{4}k_z & 0 & 0 & 0 & 0 & -\frac{B}{2}k_z & -k_\phi + \frac{B^2}{4}k_z & 0 & 0 \\
0 & 0 & 0 & 0 & k_\theta & 0 & 0 & 0 & 0 & 0 & -k_\theta & 0 \\
-\frac{B}{2}k_x & 0 & 0 & 0 & 0 & k_\psi + \frac{B^2}{4}k_x & \frac{B}{2}k_x & 0 & 0 & 0 & 0 & -k_\psi + \frac{B^2}{4}k_x \\
-k_x & 0 & 0 & 0 & 0 & \frac{B}{2}k_x & k_x & 0 & 0 & 0 & 0 & \frac{B}{2}k_x \\
0 & -k_y & 0 & 0 & 0 & 0 & 0 & k_y & 0 & 0 & 0 & 0 \\
0 & 0 & -k_z & -\frac{B}{2}k_z & 0 & 0 & 0 & 0 & k_z & -\frac{B}{2}k_z & 0 & 0 \\
0 & 0 & \frac{B}{2}k_z & -k_\phi + \frac{B^2}{4}k_z & 0 & 0 & 0 & 0 & -\frac{B}{2}k_z & k_\phi + \frac{B^2}{4}k_z & 0 & 0 \\
0 & 0 & 0 & 0 & -k_\theta & 0 & 0 & 0 & 0 & 0 & k_\theta & 0 \\
-\frac{B}{2}k_x & 0 & 0 & 0 & 0 & -k_\psi + \frac{B^2}{4}k_x & \frac{B}{2}k_x & 0 & 0 & 0 & 0 & k_\psi + \frac{B^2}{4}k_x
\end{bmatrix}$$

Now, Equation 2.39 can be expanded for the system of two interconnected floaters and is defined by Equation 2.45.

$$\tilde{u}(\omega)(-\omega^2(\boldsymbol{M} + \boldsymbol{A}(\omega)) + i\omega\boldsymbol{B}(\omega) + \boldsymbol{C} + \boldsymbol{K_{conn}}) = \tilde{F_w}(\omega) \tag{2.45}$$

Where,

- $\tilde{u}$ is the complex motion vector, $\tilde{u}(\omega) = \begin{bmatrix} \tilde{x_1} & \tilde{y_1} & \tilde{z_1} & \tilde{\phi_1} & \tilde{\theta_1} & \tilde{\psi_1} & \tilde{x_2} & \tilde{y_2} & \tilde{z_2} & \tilde{\phi_2} & \tilde{\theta_2} & \tilde{\psi_2} \end{bmatrix}^T$
- $\boldsymbol{M}$ is the mass matrix (12x12)
- $\boldsymbol{A}$ is the added mass matrix (12x12)

- $\boldsymbol{B}$ is the hydrodynamic damping matrix (12x12)
- $\boldsymbol{C}$ is the hydrostatic stiffness matrix (12x12)
- $\boldsymbol{K_{conn}}$ is the connection stiffness matrix (12x12)
- $\tilde{F_w}$ is the complex wave exciting force and moment vector

2.6 Expansion to Multiple Interconnected Bodies

The procedure described in Section 2.5 can be further developed to account for multiple floating bodies. Every new added body will introduce 6 more DoF and therefore all matrices have to be adjusted accordingly. For example, 4 interconnected, with the same single connection, bodies will result into matrices of dimensions 24x24. The methodology is the exact same, however with an important increase in computational time.

2.7 Drift Forces

2.7.1 Wave Loads

Offshore structures exposed to waves experience different type of loads and have consequently different responses. Firstly, there are loads that are linearly proportional in amplitude to the wave amplitudes and are therefore called first order wave forces. Section 2.2 included a thorough analysis of these loads.
Next to these loads, there are other wave load components that apply forces which are proportional to the square of the wave amplitude and are called second order wave forces [52]. The existence of these non-zero mean components of the total wave force acting on a floating vessel was initially reported by [98] during experiments of a rolling vessel in regular beam waves. It was noted that the vessel was subjected to a mean sway force which was at first explained as the capability of the vessel to partially reflect the incoming wave. These second order wave forces have frequencies that are either higher or lower than the frequencies of the waves.
The low frequency second order wave forces present frequencies which come as a result of the presence of wave groups in irregular waves. These forces can be further analyzed into two different components. The first component is a time-varying force while the second one is a non-zero mean force which is well known as wave drift force. This name comes as a result of the tendency of a freely floating vessel to drift in the direction of the propagating waves due to the influence of these mean second order forces. It has been observed that low-frequency components can significantly influence moored vessels which in general have low natural frequencies. On top of that, at these low frequencies damping is rather small which also enables large surge and sway motions. As a result, the mooring system should be suitably designed to withstand these potentially large motions.
The high frequency second order wave forces contain frequencies that occur after the summation of different wave frequencies and are in the order of double the frequency of the waves. It can be said that the effect of these sum frequencies on the horizontal motions response of moored structures is generally small. However, this could change in the case of very stiff structures.
For the purpose of this project, further attention would be paid to the estimation of the mean drift forces as they will be the most influential for the design of a mooring system.

2.7.2 Approaches

When it comes to the calculation of the wave drift force there are two well-known formulations and a third one which was later proposed and tried to offer more advantages. The first one was introduced by Maruo [68] and extended afterwards by Newman [77] and is the "far-field" method, which is based on momentum considerations. The second one is the so called "near-field" method which was proposed by Pinkster & van Oortmerssen [79] and is based on the direct pressure integration of all pressure contributions on the wetted hull of the body. The last approach is based on the Lagally formulation and was introduced by Guével & Grekas [38]. The first two approaches will be further analyzed while the latter one is only mentioned as it's use has not been widely expanded.

2.7.3 Far-Field Approach

The main idea of the far-field approach is the consideration of the contribution to the rate of change of momentum through all boundaries of the control volume Ω. Figure 2.4 gives an overview of the examined area and the corresponding boundaries. Even though Maruo [68] was the first to work on this approach, his results were lacking satisfactory verification with experimental results. It was [58] who using the theory of Maruo obtained analytical results on the mean horizontal wave force and proved that they were in reasonable correlation with measured data. Later on, [31] compared the results obtained from a modified version of the three-dimension far-field approach with experimental results. The comparison regarded a box shaped barge in regular waves and the two sets of results proved to be in good comparison.

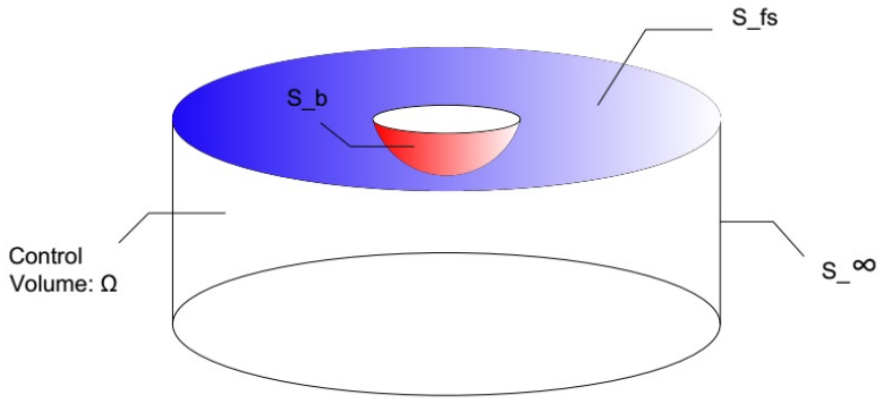

Figure 2.4: Far-Field approach

Besides the control volume we can distinguish four more elements.

- S_b: under water body surface
- S_{fs}: water free surface
- S_∞: cylindrical surface surrounding control volume at infinite distance
- Infinite water depth assumption is made and therefore bottom is neglected

The average wave force on the floating body can be expressed by Equation 2.46 as given by [104].

$$\begin{pmatrix} \overline{F_x} \\ \overline{F_y} \end{pmatrix} = -\rho \iint_{S_\infty} \frac{p}{\rho}\vec{n} + \begin{pmatrix} u \\ v \end{pmatrix} V_n dS_\infty \tag{2.46}$$

In order to use the previous equation the potential should be solved at infinity in order to estimate the fluid velocity and fluid pressure at infinity. It must be noted here that this expression does not take into account first order wave forces as they average zero over one period.
As we have already seen, any type of potential, either radiation or diffraction, can be expressed by Green's theorem at any point (x,y,z) of the domain by Equation 2.47.

$$\phi_j(x,y,z) = \frac{1}{4\pi} \iint_{S_b} G\frac{\partial \phi_j}{\partial n} - \phi_j \frac{\partial G}{\partial n} dS_b \tag{2.47}$$

Where G is Green's function which dictates how potentials are transferred throughout the domain as a result of the presence of the body. So, it naturally follows that an approximation of Green's function at infinity is the next step. This has already be done by Newman [77] and is described in Equation 2.48.

$$G = 2(\frac{2\pi k}{R})^{1/2} e^{k(z+\zeta)+i(kR+\frac{\pi}{4})} \tag{2.48}$$

Where,

- R is the horizontal distance between a point on the body surface and the point of the domain at which the function needs to be estimated
- ζ is the vertical position of a point on the body surface

Finally, a substitution of Equation 2.48 into Equation 2.47 can yield the potential at infinite distance from the body. This is described by Equation 2.49.

$$\phi_j(x,y,z) = (\frac{k}{2\pi R_0})^{1/2} e^{k(z+\zeta)+i(kR_0+\frac{\pi}{4})} H(\pi+\theta) \tag{2.49}$$

Where, $H(\pi+\theta)$ is the complex Kochin function and is unique for every geometry for every radial direction (θ) around the body. With simple words, Kochin function is a directional function that enables the transfer of the potential from the body surface to a large distance R_0 away from the body.

Finally, with the substitution of the following equations (Equation 2.50-2.54) into Equation 2.49, the derivation of the horizontal drift forces based on the far-field approach is completed and described by Equation 2.55.

$$x = R_0 cos\theta \tag{2.50}$$

$$y = R_0 sin\theta \tag{2.51}$$

$$p = -\rho Re\{-i\omega\phi_j e^{-i\omega t}\} - \frac{1}{2}\rho|\vec{V}^2| - \rho g z \tag{2.52}$$

$$V_R = Re\{\frac{\partial\phi_j}{\partial R} e^{-i\omega t}\} \tag{2.53}$$

$$V_\theta = Re\{\frac{1}{R}\frac{\partial\phi_j}{\partial\theta} e^{-i\omega t}\} \tag{2.54}$$

$$\begin{pmatrix}\overline{F_x}\\ \overline{F_y}\end{pmatrix} = \frac{\rho k^2}{8\pi}\int_0^{2\pi} |H(\theta)^2| (\begin{pmatrix}cos\theta\\ sin\theta\end{pmatrix}) d\theta + \frac{1}{2}\rho\omega A(\begin{pmatrix}cos\beta\\ sin\beta\end{pmatrix}) Im\{H(\pi+\beta)\} \quad [\text{N m}^{-2}] \tag{2.55}$$

It is obvious from the last formula that for the calculation of wave drift forces with the far-field approach, the main input needed is the Kochin functions with the appropriate resolution in radial direction (θ).

According to [76], the relationship between the Kochin function and the velocity potential is given by Equation 2.56.

$$\phi_X(M) = \frac{cosh(k(z+h))}{cosh(kh)} \cdot \sqrt{\frac{k}{2\pi r}} e^{i(kr-\frac{\pi}{4})} H_X(\theta) \tag{2.56}$$

With,

- (r,θ,z) the cylindrical coordinates of M
- perturbation potential $\phi_P = \phi_D + \phi_R$
- $\phi_R = -i\omega\sum_{j=1}^{6} \tilde{X_j}\cdot\phi_j$
- X_j and ϕ_j the motions and radiation potential for the DoF j
- $X_j(t) = Re(\tilde{X_j}\cdot e^{-i\omega t})$

Due to the inherent phase conventions of NEMOH code ,which is the main software used in this project, the Kochin function per frequency is described by Equation 2.57.

$$\tilde{H}(\theta,\omega) = \tilde{H_D}(\theta,\omega)e^{i\frac{\pi}{2}} - i\omega\sum_{j=1}^{6}\tilde{X_j}(\omega)\cdot\tilde{H_{R_j}}(\theta,\omega)e^{i\frac{\pi}{2}} \tag{2.57}$$

Where,

- $\tilde{H_D}(\theta,\omega)$ is the Kochin function associated with the diffracted potential for wave frequency ω

- $\tilde{H}_R(\theta, \omega)$ is the Kochin function associated with the radiation potential for wave frequency ω

Finally, the horizontal drift forces F_{drift} per wave amplitude can be calculated for each wave frequency of the incident wave field as Equation 2.58 [21]:

$$\begin{pmatrix} F_{drift,x}(\omega) \\ F_{drift,y}(\omega) \end{pmatrix} = -2\pi\rho A\omega(\begin{pmatrix} cos\beta \\ sin\beta \end{pmatrix})Im(\tilde{H}(\beta,\omega)) - 2\pi\rho\frac{k(k_0h)^2}{h[(kh)^2-(k_0h)^2+k_0h]} \cdot \int_0^{2\pi} |\tilde{H}(\theta,\omega)|^2 \begin{pmatrix} cos\theta \\ sin\theta \end{pmatrix} d\theta \tag{2.58}$$

With,

- $\tilde{H}(\theta, \omega)$ is the complex Kochin function without time dependence at wave frequency ω and incidence θ, as described by Equation 2.57, expressed in $[m^2/s]$
- β is the incident angle of waves
- $k_0 = \frac{\omega^2}{g}$ is the deep water wave number
- $k \cdot tanh(kh) = \frac{\omega^2}{g}$ is the wavenumber at the water depth considered
- h is the water depth
- A is the wave amplitude

2.7.4 Near-Field Approach

As was mentioned earlier, the near-field approach is based on the direct pressure integration of the wetted surface of the body. Before diving into the equations that govern this method it is necessary to present the system of coordinates used for it (Figure 2.5).

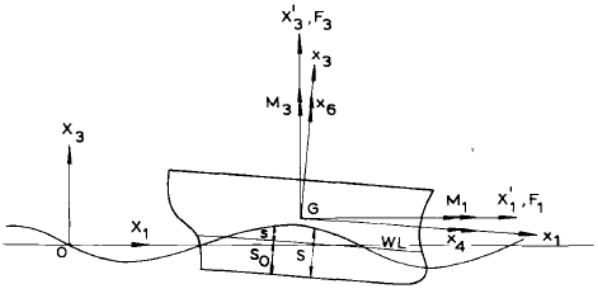

Figure 2.5: System of coordinates for the near-field approach [79]

Three different systems of co-ordinate axes can be distinguished. The first one is a right-handed earth-bound system of $O - x_1 - x_2 - x_3$ with O being the origin, X_1 and X_2 axes in the mean free surface of the sea and X_3 defined positive in the upward direction. Any given point in space can be described by the vector $\vec{X} = (X_1, X_2, X_3)$.
The second one is a right-handed system $G - x_1 - x_2 - x_3$ body-bound axes with origin the center of gravity of the body G. Again, the $G - x_3$ axis is defined positive in the upward direction and the x_1 axis in the longitudinal direction. In the mean position of the freely floating vessel this axes system is parallel to the earth bound system. This system of axes is exclusively defining the surface of the hull. A position vector $\vec{x} = (x_1, x_2, x3)$ can define any point of the body surface in this body-bound axes system. Additionally, an outward point normal vector $\vec{n} = (n_1, n_2, n_3)$ is defining the orientation of any surface element in this system of coordinates.
Finally, there is a third system of coordinates $G(X_1', X_2', X_3')$ which is a moving axes system with its origin in the mean position of the center of gravity G, of the body. This system has axes which are always parallel to the earth-bound system. This means that this system does not translate or rotate with the ship's motions, with the exception of the forward vessel speed if present.

The floating body is exposed to the fluid force, with respect to the $G(x, y, z)$ system of axes, and can be described by Equation 2.59 [52].

$$\vec{F} = -\iint_S p \cdot \vec{N} \cdot dS \tag{2.59}$$

Where,

- S is the instantaneous wetted surface
- $\vec{N}$ is the instantaneous normal vector to the surface element dS relative to the $G(x, y, z)$ system of axes

Figure 2.6 presents the separation of the the wetted surface into two parts: a constant part S_0 up to the static hull waterline and an oscillating part s, the splash zone between the static hull waterline and the wave profile along the body.

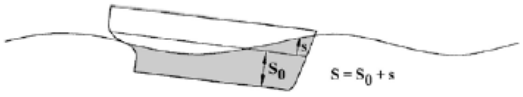

Figure 2.6: Wetted surface [52]

Expanding Equation 2.52 to the non-linear Bernoulli equation and with the use of Taylor's expansion, after adopting the assumption of small-first order- wave frequency motions, the pressure in the mean position of the vessel can be expressed by Equation 2.60 and the normal vector $\vec{N}$ by Equation2.64

$$p = p^{(0)} + \epsilon p^{(1)} + \epsilon^2 p^{(2)} \tag{2.60}$$

With,

- hydrostatic pressure:

$$p^{(0)} = -\rho g \vec{X}_3^{(0)} \tag{2.61}$$

- first order pressure:

$$p^{(1)} = -\rho g \vec{X}_3^{(1)} - \rho \frac{\partial \Phi^{(1)}}{\partial t} \tag{2.62}$$

- second order pressure:

$$p^{(2)} = -\frac{1}{2}\rho(\vec{\nabla}\Phi^{(1)})^2 - \rho\frac{\partial^2 \Phi^{(2)}}{\partial t^2} - \rho(\vec{X}^{(1)} \cdot \nabla \frac{\partial \Phi^{(1)}}{\partial t}) \tag{2.63}$$

$$\vec{N} = \vec{n} + \epsilon R^{(1)} \cdot \vec{n} \tag{2.64}$$

with $R^{(1)}$ being the linearized rotation transformation matrices as given by Equation 2.65.

$$\vec{R}^{(1)} = \begin{bmatrix} 0 & -\dot{x}_6^{(1)} & +\dot{x}_5^{(1)} \\ +\dot{x}_6^{(1)} & 0 & -\dot{x}_4^{(1)} \\ -\dot{x}_5^{(1)} & +\dot{x}_4^{(1)} & 0 \end{bmatrix} \tag{2.65}$$

Using all the above and substituting them in Equation 2.59, the fluid force on the body is given by Equation 2.66.

$$\begin{aligned} \vec{F} = &-\iint_{S_0} (p^{(0)} + \epsilon p^{(1)} + \epsilon^2 p^{(2)}) \cdot (\vec{n} + \epsilon \vec{N}^{(1)}) \cdot dS \\ &-\iint_s (p^{(0)} + \epsilon p^{(1)} + \epsilon^2 p^{(2)}) \cdot (\vec{n} + \epsilon \vec{N}^{(1)}) \cdot dS \end{aligned} \tag{2.66}$$

Equation 2.66 is the basis for the calculation of the second order wave forces with the direct pressure integration method. The exact derivations can be found in [52] but will not be included in this report as they are out of scope. The total second order fluid force is made of three separate contributions as can be seen in Equation 2.67.

$$\begin{aligned}\vec{F}^2 &= \vec{F}_A^2 + \vec{F}_B^2 + \vec{F}_D^2 \\ &= m \cdot R^{(1)} \cdot \vec{\ddot{X}}_G^{(1)} \\ &+ \iint_{S_0} \{\frac{1}{2}\rho(\vec{\nabla}\Phi^{(1)})^2 + \rho\frac{\partial\Phi^{(2)}}{\partial t} + \rho\vec{X}^{(1)} \cdot \vec{\nabla}\frac{\partial\Phi^1}{\partial t}\} \cdot \vec{n} \cdot dS \\ &- \oint_{wl} \frac{1}{2}\rho g(\zeta_r^{(1)})^2 \cdot \vec{n} \cdot dl\end{aligned} \tag{2.67}$$

The first component ($\vec{F}_A^2$) of Equation 2.67 includes products of the first order pressures and the first order oscillatory components over the constant part S_0.
The second component ($\vec{F}_B^2$) comes after the direct integration of the second order pressure over S_0.
Finally, the last component ($\vec{F}_D^2$) contains the contribution of the first order pressures over the oscillatory part s.
Figure 2.7, presents the results of the normalized drift force for a floating sphere and also gives the individual contributions of every component mentioned earlier.

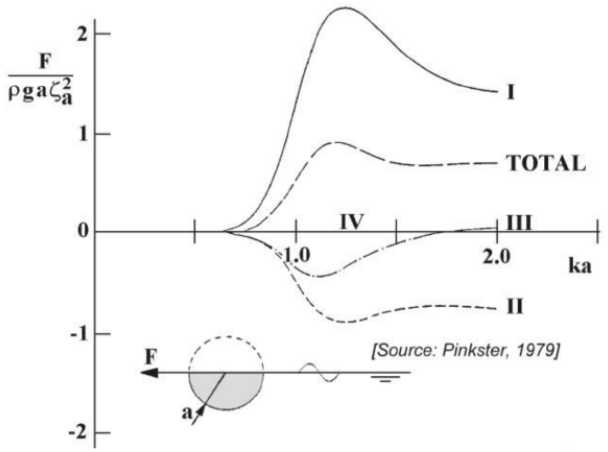

Figure 2.7: Contributions of pressure integration with near-field approach [79]

Where,

- I is the relative wave height contribution:

$$-\frac{1}{2}\rho g \oint_{wl} \frac{1}{2}\rho g(\zeta_r^{(1)})^2 \cdot \vec{n_1} \cdot dlg$$

- II is the contribution from the pressure drop due to velocity squared:

$$+\frac{1}{2}\rho \iint_{S_0} \{\frac{1}{2}\rho(\vec{\nabla}\Phi^{(1)})^2 \cdot \vec{n_1} \cdot dS$$

- III is contribution from pressure due to the product of gradient of first order pressure and first order motion:

$$+\rho \iint_{S_0} \vec{X}^{(1)} \cdot \vec{\nabla}\frac{\partial\Phi^1}{\partial t}\} \cdot \vec{n_1} \cdot dS$$

- IV is contribution due to product of pitch motion and heave inertia force:

$$+m \cdot x_5^{(1)} \cdot \vec{\ddot{X}}_3^{(1)}$$

It is apparent that contribution I is dominant, with the rest only tending to reduce its effect. The contributions of second order potential is zero for regular waves.
The following figures show results that were used to validate the near-field approach for the calculation of horizontal drift forces [21, 52]. Figure 2.8a presents the mean horizontal wave drift force on a floating sphere

with 1m radius at infinite water depth while Figure 2.8b the horizontal force for a barge with dimensions L=150m, B=50m, D=10m at 50m water depth. It can be said that this method gives sufficiently accurate results and allows for the estimation of the mean drift fore.

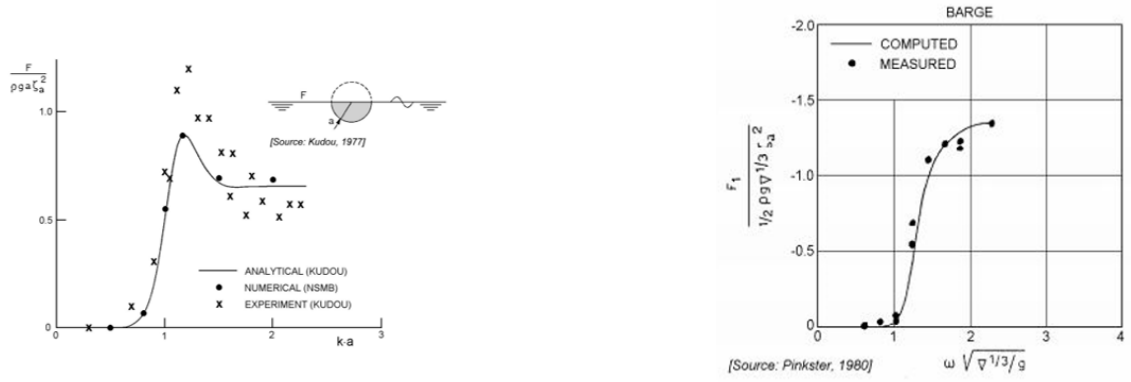

(a) Validation for a sphere at infinite water depth [52]

(b) Validation for a barge at 50m water depth [79]

Figure 2.8: Near-field approach validation

2.7.5 Selection of Approach

In Sections 2.7.3 and 2.7.4, a thorough presentation of the far and the near field approach respectively has been performed. The first one gives the mean drift force on a floating body by evaluating the disturbances resulting from the body at infinity. The latter uses a direct pressure integration over the instantaneous body surface and considers also second order terms. It could be said that if accuracy and the full quadratic transfer functions are seeked, the near-field approach is the most appropriate method. However, for this project, the far-field approach is adopted for two main reasons:

- for the estimation of the mooring force, the mean drift force is sufficient
- the selected software is suitable for the direct use of Kochin functions

3 | Implementation

This chapter can be mainly divided into three different sections. The first section regards the considerations behind the selection of the base case design for the layout of the hybrid power park. After that, the environmental conditions at the location of the Delta21 lake will be presented. Finally, the methodology that is adopted in the current project will be explained with an explanation regarding the software used.

3.1 HPP layout

In order to come to an initial layout for the HPP, there are multiple aspects that could be used to define the share of each energy resource. For the needs of this project, this selection will be limited to two main components: the levelized cost of solar and wind energy as well as the annual energy production.

3.1.1 Solar Panels Cost Breakdown

In this first stage, it is valuable to have a look at the various components that consist the investment costs for a stand-alone system of solar panels. The capital expenditures can be further divided in 3 main parts as presented in Figure 3.1. This data was adopted by [81] and further modified by [9].

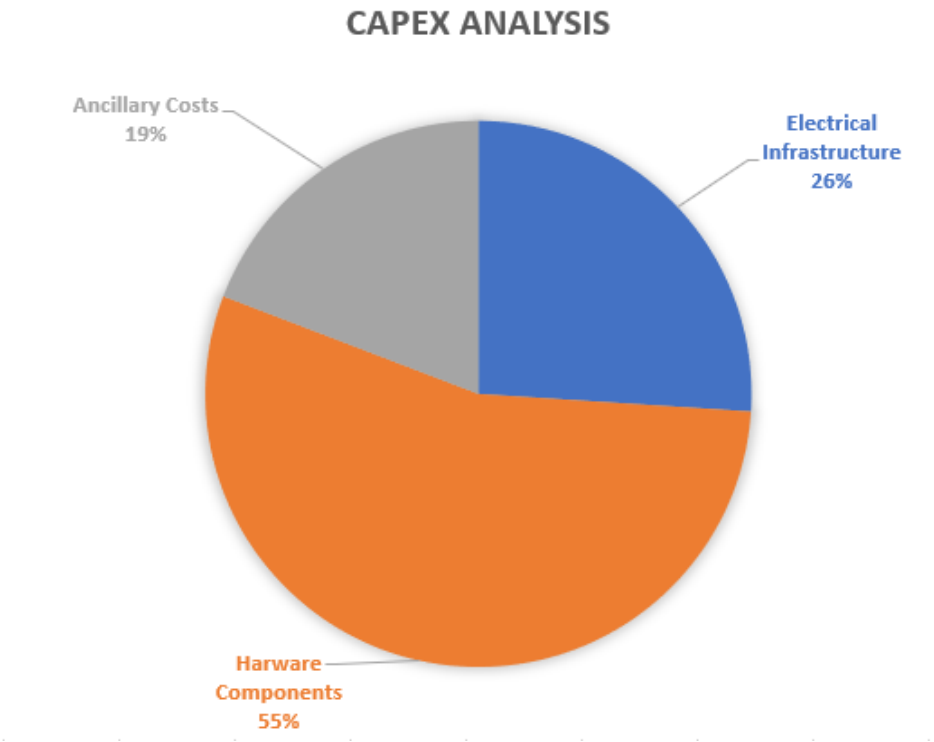

Figure 3.1: Photovoltaic Panels CAPEX analysis [81]

From Figure 3.1 it is obvious that the hardware components (modules and mounting system) comprise the most expensive unit. For floating PV panels, the mounting system is consisting of the floaters, the mooring

lines and the anchoring system. After the analysis of the share of the costs, a further presentation of the values themselves is performed in Table 3.1.

Component	Cost
Hardware Components	€0.35/W
Electrical Infrastructure	€0.17/W
Ancillary Costs	€0.12/W
CAPEX	€0.63/W
OPEX	€0.0075/W

Table 3.1: PV Capex & Opex [81]

As seen in Table 3.1, the operational expenditures account for 1.2% of the capital costs. The main reason for these low operational and maintenance costs are the competitive pressures and improvements in the reliability of the technology which have resulted in system designs that are optimized to reduce O&M costs. In addition, improved strategies that take advantage of a range of innovations have also driven down O&M costs and reduced downtime. Such innovations stretch from robotic cleaning to 'big data' analysis of performance to identify issues and initiate preventative interventions ahead of failures [48].

3.1.2 Offshore Wind Turbines Cost Breakdown

The same estimation as done previously for the solar panels can be done for a standalone system of offshore wind turbines. Firstly, an analysis of the different components of the capital expenditures is presented in Figure 3.2 and in Table 3.2. Once again, the same three main categories have been selected to allow for a direct comparison.

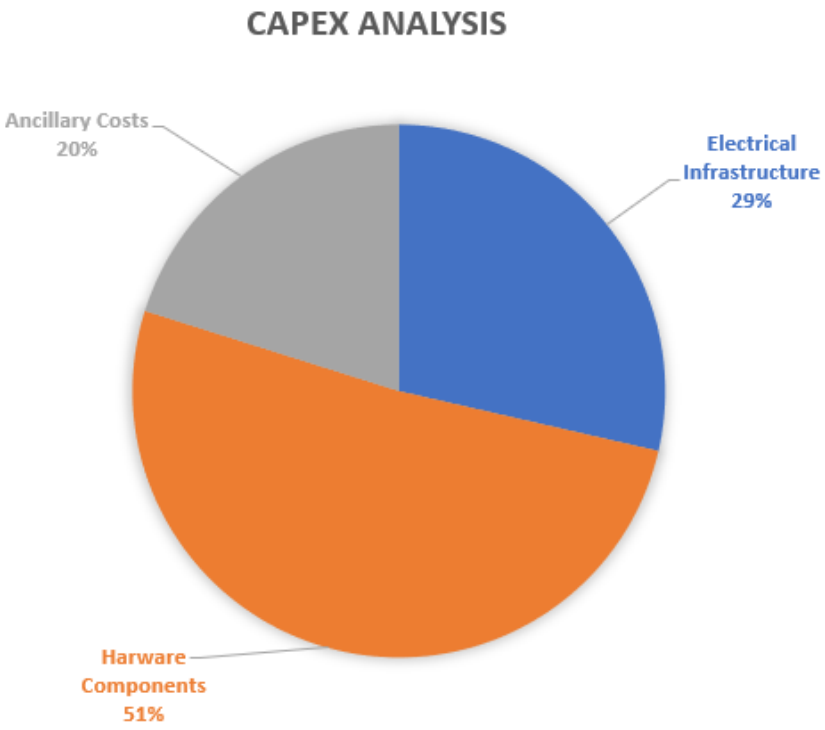

Figure 3.2: Offshore Wind Turbines CAPEX analysis [86]

Component	Cost
Hardware Components	€1.31/W
Electrical Infrastructure	€0.73/W
Ancillary Costs	€0.51/W
CAPEX	€2.55/W
OPEX	€0.088/W

Table 3.2: Wind Capex & Opex

For a standalone wind park, the data from Table 3.2 reveals that the operational expenditures are 3.5% of the capital costs. According to [48], these costs remain high due to the fact that accessing the wind site to perform maintenance on turbines is heavily influenced by weather conditions and the availability of skilled personnel and specialized vessels. In this perspective, the location of the Delta21 lake seems favorable since it is really close to the shore, is in shallow water depths and finally offers mild environmental conditions (small wave heights).

Moreover, it is observed that the initial investment of the turbine itself as well as the support structure and foundation are the most influential cost parameters accounting for 51%.
When compared to a standalone solar park, even though the allocation of the capital costs is similar, the total capital costs of solar are only 25% of wind.

With the values for the capital and operational expenditures known, a fist estimation of the Levelized Cost of Energy (LCOE) is possible. LCOE is an index that uses the overall costs and the energy production and gives an insight of how expensive the system under consideration is (expressed in €/MWh). The following formula is used for the estimation of LCOE:

$$LCOE = \frac{\textit{NPV of Total Costs Over Lifetime}}{\textit{NPV of Electrical Energy Produced Over Lifetime}} = \frac{\sum \frac{(I_t + M_t + F_t)}{(1+r)^t}}{\sum \frac{E_t}{(1+r)^t}}$$

With,

- I: the initial cost of investment
- M: maintenance and operations expenditures
- F: fuel expenditures (if applicable)
- E: sum of electricity produced
- r: discount rate
- t: the lifetime of the project

3.1.3 HPP LCOE

Before looking at the combined LCOE for the hybrid power plant, it is necessary to estimate the LCOE for the individual resources. As it expected that the project of Delta21 could be actualized around 2030, projected values of the capital expenditure will be used.
According to IRENA's report for the forthcoming trends and the future of solar PV panels [46], a reduction of the installation costs is expected by 2030 that can reduce the CAPEX to €0.52/W (average value).This means that the levelized cost of energy is sensitive towards the available technologies and consequently the available prices of the industry. Therefore, the actual construction date of the project is important as it will define mainly the initial investment costs. An analytical calculation of the LCOE can be found in Appendix A.To perform this calculation, a few assumptions need to be made.These are presented in Table 3.3.

Component	Value
Year of construction	2030
Installed Capacity	250W/m^2
Degradation of the panels	0.5%
Discount rate	6%
Project lifespan	30 years
LCOE	€45.77/MWh

Table 3.3: LCOE analysis for PV panels

Looking at the trends of offshore wind and in particular in the estimations of the capital costs reduction by 2030, a significant decrease is expected [47]. After estimating the operational and capital costs, a first calculation of the LCOE for the wind turbine can be achieved, with the approximations/assumptions presented in Table 3.4. This value is in good agreement with a conservative approach found in [17]. Again, a more analytical presentation of the LCOE calculation can be found in Appendix A.

Component	Value
Year of construction	2030
Installed Capacity	128kW/turbine
Degradation of the wind turbines	0.5%
Discount rate	6%
Project lifespan	30 years
LCOE	€50.00/MWh

Table 3.4: LCOE analysis for the wind turbines

From Tables 3.3 and 3.4 it is becoming obvious that the levelized cost of energy is lower for a standalone solar park than a standalone wind park, with the latter being 9.2% more expensive. If these two systems are combined and integrated with a large storage unit, the following benefits can occur:

- the integration of floating solar units and offshore wind turbines can increase the capacity factor of the main export cable and lead to an overall capital cost reduction, according to [17]
- the addition of the storage function, through the use of energy lake, can lead to 10-15% reduction of the overall capital expenditures, as demonstrated by the Delta21 organization [7]
- the energy production can be evenly distributed to the two resources, leading to a low variability index [62] and consequently to a flatter and smoother output

For this project, the installed power share is selected to be 21.7% of wind and 78.3% of solar. This results into an energy production share of 43.9% for wind and 56.1% for solar. This would lead to a combined LCOE of 47.62 €/MWh, which could be further reduced according to the three bullet-points mentioned above.
This configuration is adopted in order to visualize the potential synergy of mooring the floating panels on the wind turbines, but it could be further optimized to meet the potential objectives of cost minimization, energy maximization, reduction of shadow effects or output variability.

3.1.4 Base Case Design

After the analysis in Section 3.1.3, the base case design can be defined. Even though the available surface of the lake is approximately 43 km^2, as a first step the design is going to be focused in a rectangle of 1 km^2. In this way, it would be easier to make comparisons with other projects and investigate up to what extend this design can be up-scaled to maximize the energy production. During this early stage, the considerations that were mainly accounted for are:

- spacing between the turbines is set to be just around 3 rotor diameters, which is the distance provided by DWD to minimize wake losses
- every wind turbine and every solar boat must be easily accessible for maintenance
- the wind is considered omnidirectional allowing for same wind turbine spacing in the two main directions
- a minimum distance between the tower of the wind mills and the solar boats must be set, in order to limit the shadow effects and also leave sufficient space for the mooring lines

All the above can be observed in Figure 3.3 while a representation of the side view in Figure 3.4. At this design stage, it is assumed that a mooring line can be attached at the tower of the wind turbine and then connected to a fairlead point at the solar boat. In this way, the mooring system and the floating solar unit can follow the water level fluctuations of the lake. The technical design of the connection is out of the scope of this project. However, together with its economic impact, they are two factors that should be later investigated.

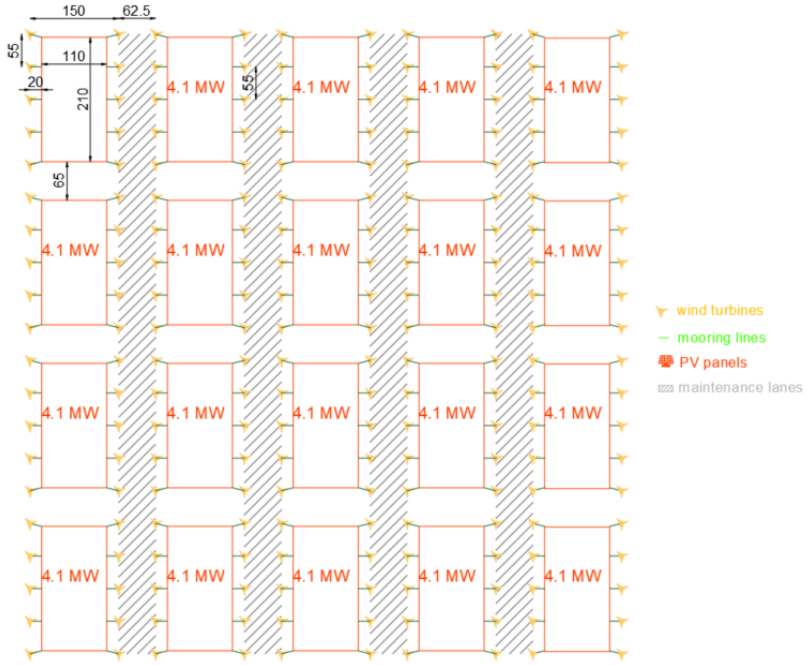

Figure 3.3: Base Case Design Layout (distances in meters)

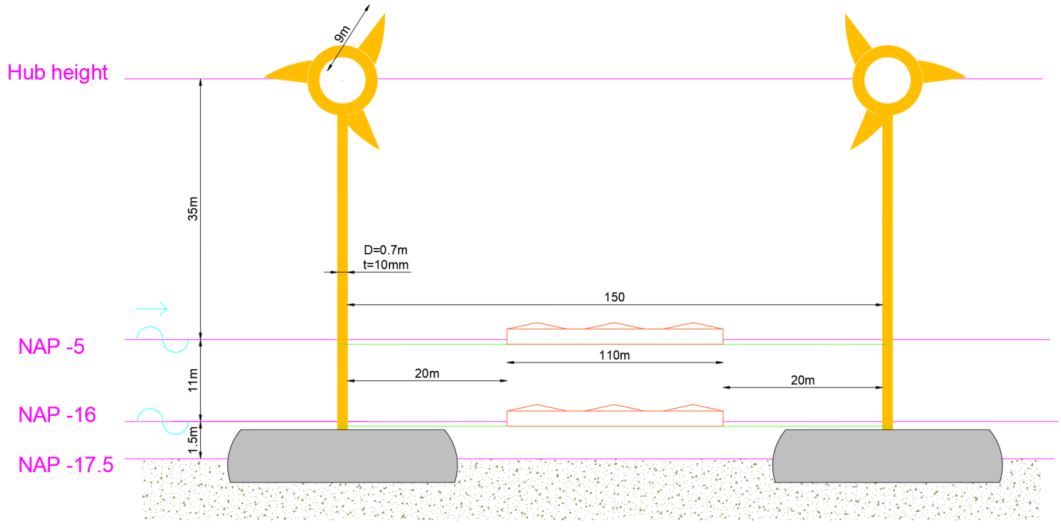

Figure 3.4: Impression of side view

All assumptions adopted for a first estimation of the installed capacity and the energy outcome are represented in Table 3.5.

Wind	
Rotor diameter	18 m
Turbine spacing	55>3D =54 m
Total number of turbines	200
Installed power	128.0kW/turbine
Total wind installed power	25.6 MW/km^2
Generator efficiency	97.8%
System Losses	7.5%
Energy produced [11]	377 MWh/turbine
Total wind energy production	75.4 GWh/year
Capacity factor	0.336
share of installed power	21.7%
share of energy production	43.9%

Solar	
Area per solar unit	23,100 m^2
Excluding walkways (assumed 20%)	18,480 m^2
Total area of solar park	369,600 m^2
Power installed [9]	250 W/m^2
Total solar installed power	92.4 MW/km^2
Tilt angle	12^o
System Losses	10.0%
Energy produced [16]	1041.62 kWh/kW
Total solar energy production	96.2 GWh/year
Capacity factor	0.119
share of installed power	78.3%
share of energy production	56.1%
Combined specific yield	118 MW/km^2
Combined energy output	171.7 GWh/year

Table 3.5: Estimation of installed capacities and energy output per resource

3.2 Environmental Loading

This section will give a presentation regarding the prevailing wind and wave conditions in the Energy Storage Lake of Delta21. The location of the lake will be at the north-west of the Tweede Maasvlakte and can be described by the coordinates: 52°00'N, 03°40° E.

3.2.1 Wind Data

With hindcasted wind data retrieved from [44], the wind characteristics can be seen in Figure 3.5. It must be noted that wave data of the last 28 years over the area under examination was used for the generation of wind data.

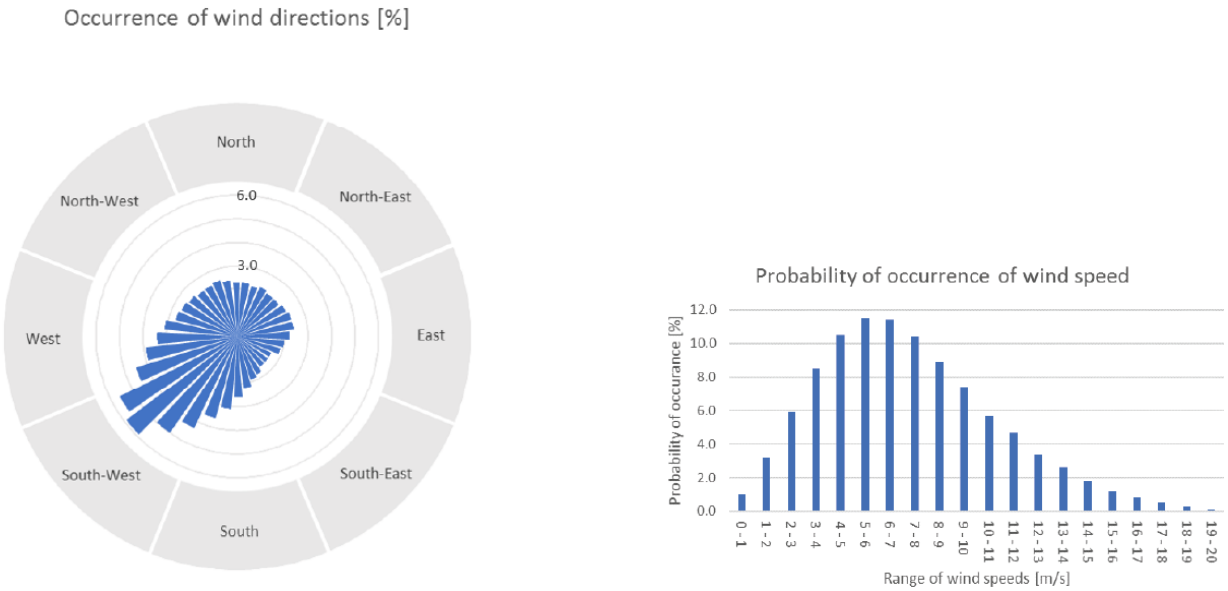

(a) Probability of the wind direction[10]

(b) Probability of the wind speed[10]

Figure 3.5: Predominant wind direction and wind speed for the location of the ESL

Besides the predominant wind conditions, according to [102] it is important to assess the mean 1-hour wind speed for a 50-year return period, in order to statically calculate the environmental loading. This assessment has been performed in [29], where a value of 29.9m/s at a height of 10 meters has been found. To accordingly translate this value to the actual height of the wind panels Equation 3.1 is used.

$$U(h) = U(h_{ref})(1 + \frac{\ln(\frac{h}{href})}{\ln(\frac{h}{z_0})}) \tag{3.1}$$

Where,

- h_{ref} is the reference height (10m) at which the wind speed is known
- h is the height at which the wind is acting on the solar panels (0.5m)
- z_0 is the roughness parameter, here estimated as 0.01 which corresponds to the upper limit of an open sea with waves and of a coastal area as there are dunes at the perimeter [23]

Substituting the aforementioned values in Equation 3.1, it is found that the 50-year 1-hour wind speed at a height of 0.5m is 15.2m/s.

3.2.2 Wave Model

Ocean waves can be modelled by the superposition of a number of regular waves (Figure 3.6). This superposition can be later modelled as a wave spectrum. For the construction of this wave spectrum two different variables must be known and these are: the significant wave height and the peak period. However, in order to estimate these values the wind speed and the available fetch, meaning the available area for the waves to developed, must also be known.

According to [39], the significant wave height H_{m0} and the peak period T_p can be calculated based on the dimensionless significant wave height $\tilde{H}_{m0}$ (Equation 3.2) and the dimensionless period $\tilde{T}_p$ (Equation 3.5) respectively. This method was first introduced by [112] in an attempt to match empirical data with measured ones for a lake with 10km width and 20km length.

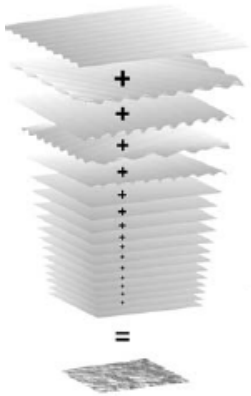

Figure 3.6: Superposition of harmonic waves with random amplitudes, directions and phases[39]

$$H_{m0} = \tilde{H}_{m0}\frac{U_{10}^2}{g} \tag{3.2}$$

where,

- g is the gravitational acceleration
- U_{10} is the wind speed 10m above still water level
- $\tilde{H}_{m0}$ is given by Equation 3.3

$$\tilde{H}_{m0} = \tilde{H}_{\infty}(tanh(k_1\tilde{F}^{m_1}))^p \tag{3.3}$$

where, $\tilde{H}_{\infty}, k_1, m_1, p$ are constants and their values are given in Table 3.6. $\tilde{F}$ is the dimensionless fetch and can be calculated according to Equation 3.4.

$$\tilde{F} = F\frac{g}{U_{10}^2} \tag{3.4}$$

Regarding the peak period the following relationships can be used:

$$T_p = \tilde{T}_p\frac{U_{10}}{g} \tag{3.5}$$

where, $\tilde{T}_p$ is given by Equation 3.6.

$$\tilde{T}_p = \tilde{T}_{\infty}(tanh(k_2\tilde{F}^{m_2}))^q \tag{3.6}$$

and $\tilde{T}_{\infty}, k_1, m_1, p$ are constants and their values are given as previously in Table 3.6.

Wave height		Peak period	
Constant	Value	Constant	Value
$\tilde{H}_\infty$	0.24	$\tilde{T}_\infty$	7.69
k_1	$4.14 \cdot 10^{-4}$	k_2	$2.77 \cdot 10^{-7}$
m_1	0.79	m_2	1.45
p	0.572	q	0.187

Table 3.6: Constant values for the calculation of wave height and peak period [39]

For the specific case of the Delta21 energy storage lake, the fetch is not constant. Therefore, this value ranges from 1 to 6km to capture the influence of the fetch in the corresponding wave height and period. Another important aspect is that once the lake has been filled in (partially) with floating solar panels, the available fetch will be further reduced due to the existence of these structures. This influence will not be taken into account in this project.

Now, with the provided equations it is possible to calculate the significant wave height and wave period for different wind speeds and different available fetches. This is presented in Table 3.7.

Wind speed [m/s]	F=1km		F=3km		F=6km	
23.4 (1-year max)	H=0.57m	Tp=2.38s	H=0.94m	Tp=3.20s	H=1.29m	Tp=3.87s
26.8 (10-year max)	H=0.66m	Tp=2.54s	H=1.09m	Tp=3.41s	H=1.49m	Tp=4.12s
30 (50-year max)	H=0.75m	Tp=2.67s	H=1.24m	Tp=3.60s	H=1.70m	Tp=4.34s

Table 3.7: Influence of wind speed and fetch on peak period and significant wave height

After calculating the significant wave height and the peak period it is possible to generate the corresponding wave spectrum. There are two main types of spectra: the first is called JONSWAP and the second is the Pierson-Moskowitz (PM). The latter one is assumed to represent fully developed conditions in deep water. Additionally, the JONSWAP spectrum was developed for wind generated waves in the North sea, and is therefore closer to the environmental conditions of the ESL of Delta21. Finally, for this project the JONSWAP spectrum will be used. The assumption of deep water has to be adopted also for this case.

The JONSWAP wave spectrum can be described by Equation 3.7 according to [39].

$$E_{JONSWAP}(f) = \alpha g^2 (2\pi)^{-4} exp[-\frac{5}{4}(\frac{f}{f_{peak}})^{-4}]\gamma^{exp[-\frac{1}{2}(\frac{\frac{f}{f_{peak}}-1}{\sigma})^2]} \tag{3.7}$$

where,

- f is the wave frequency
- α is the energy scale parameter (Equation 3.8)
- g is the gravitational acceleration
- $\gamma = 3.3$ and σ (Equation 3.9) are shape parameters

$$\alpha = 0.0317 \tilde{f}_{peak}^{0.67}, \quad (\tilde{f}_{peak} = \frac{1}{\tilde{T}_{peak}}) \tag{3.8}$$

$$\sigma = 0.07 \text{ for } f \leq f_{peak} \text{ and } \sigma = 0.07 \text{ for } f > f_{peak} \tag{3.9}$$

With all information known now, it is possible to represent the wave spectrum as a function of radial frequency. The information that this graph provides is where the most wave energy will be present for the specific environmental conditions. As it is made clear from Figure 3.7, for the energy storage lake almost no wave energy is expected after 6rad/s.

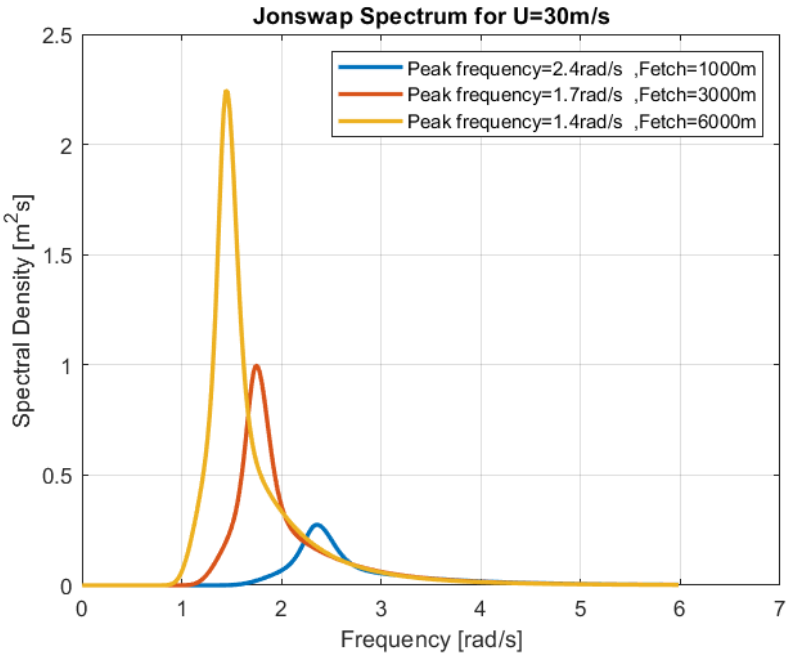

Figure 3.7: JONSWAP wave spectrum for wind speed of 30m/s and multiple fetches

3.2.3 Wind Loads on Solar Panels

This section will give an overview of the analytical method used for the calculation of wind loads on the solar panels themselves as well as the part of the floaters that stands above the waterline. The basis for these calculations was introduced in [43].

According to [24], an incoming wind is exerting a steady wind load on any floater, and this load can be described by Equation 3.10.

$$F_{wind} = \frac{1}{2}\rho V^2 A C_d C_s \tag{3.10}$$

Where,

- ρ is the density of the air
- A is the area exposed to the flow
- V is the flow velocity (at the corresponding height)
- C_s is the sheltering coefficient to account for the presence of multiple objects
- C_d is the drag coefficient and depends on the shape and surface roughness of the considered object

This formula even though it has been developed for other cases, is still applicable for the floating solar units since the background theory is valid. Two main directions of the wind will analyzed, namely $0°$ and $90°$, and this effects the projected area of the object along the wind direction. This also leads to changes in the drag coefficient.
As it is introduced by [53], the first row of panels and floaters will be the affected the most by the wind. The rows behind it, will be exposed to a reduced wind load due to the presence of the first row. This phenomenon is captured by the sheltering coefficient. Even though such an assumption can be used for this early stage of the design, it should be followed by thorough CFD calculations to properly capture this interaction.
All the analytical calculations and the corresponding coefficients can be found in Appendix B.

3.2.4 Wind Turbine Forces

As was stated in Chapter 1, the end goal of the thesis is the comparison of the potential force imposed by the mooring line with the forces already acting on the wind turbine. This section provides a presentation of the forces that would normally act on the wind turbine, without any further components from the mooring system. These forces are:

- Thrust force acting on the hub height
- Wind force acting on the ring and the blades
- Distributed wind force acting of the tower of the wind turbine
- Wave and current force acting on the submerged part of the wind turbine

The first three components are provided as input from Dutch Wind Design, after performing the required calculations. The maximum thrust force is stimulated at 2.5 $\times$ the average wind speed according to NEN-EN-61400-2. This value is also used for the calculation of the rest of the wind loads. The last component is calculated with the use of Morison equation for a peak period of 3.5s in accordance with Figure 3.7, a current velocity of $1m/s$ as estimated for a location close to the pumping station and a wave height of $1.25m$ as follows from Table 3.7. All of the aforementioned data are presented in Figure 3.8.

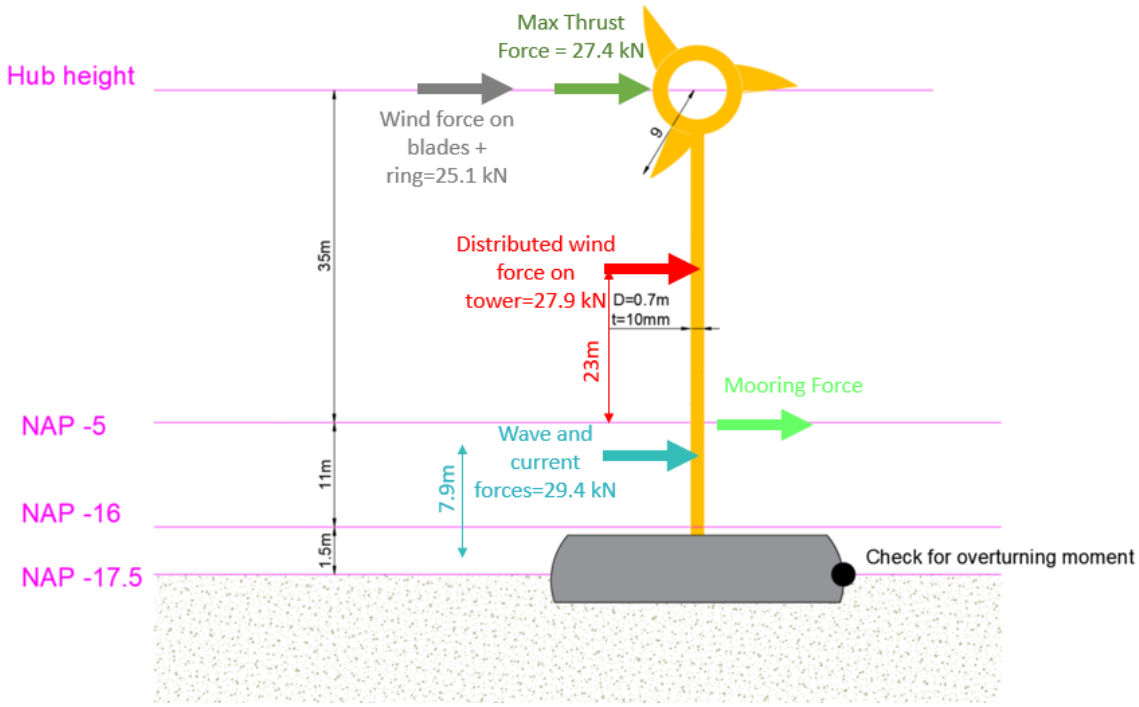

Figure 3.8: Wind turbine forces [11]

3.3 Methodology

This section gives an overview of the method used for this project. It begins with the presentation of the structure under analysis and the intermediate steps towards the calculation of drift forces follow.

3.3.1 Geometry Generation

The first step towards the estimation/calculation of the forces acting on the floating solar units is breaking down the problem into a smaller one that can be tackled. For this purpose, the analysis starts with modelling the floating solar boat that GroenLeven has introduced into the market (Figure 3.9).

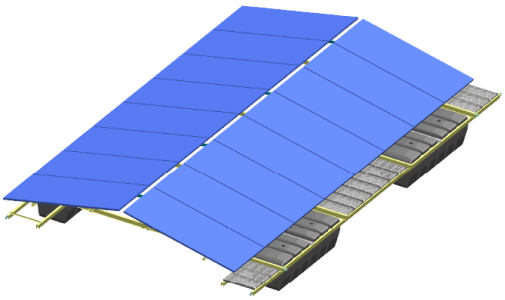

Figure 3.9: GroenLeven's floating solar boat

Three different components can be distinguished from the solar boat: 16 photovoltaic modules with an inclination of approximately $12°$, 4 plastic floaters that are the only part of the boat in contact with the water and finally the metallic frame that keeps all these parts together. Since for this project the focus is set to the hydrodynamic behavior of the floating units, the plastic floaters are the single most important element. The loading of the wind on the solar panels was exclusively treated in Section 3.2.3.

For the generation of the required geometry, the open software SALOME [13] is used. SALOME is a platform suitable for numerical simulations and it is developed by Open Cascade (France). It is well known for the simplicity and speed for the creation of various geometry models and sophisticated meshing. An illustration of the meshed floater is shown in Figure 3.10. A rectangular shape is assumed for the modeling of the floater with dimensions that can be found in Table 3.8. The last two rows include the distances between the floaters of the solar boat in the two main directions. The next steps regard the expansion of the geometry from a single floater to a system of four floaters with the main system of coordinates located in the middle.

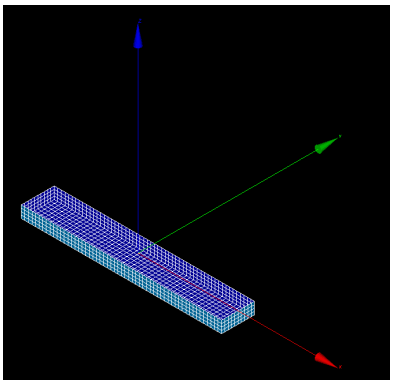

Figure 3.10: Mesh generation with SALOME

Length	2.100m
Width	0.588m
Draft	0.360m
Total Height	0.630m
x- offset	2.820m
y-offset	4.226m

Table 3.8: Floater's dimension

3.3.2 Hydrodynamic Simulations

After defining the dimensions of the floater and the wave spectrum, for a range of wave frequencies between 0.1 and 6rad/s, the ratio of the width of the structure over the wave length ranges from 10^{-5} to 0.35. According to Figure 2.1, this means that for the shorter waves the structure is not considered slender anymore, making the diffraction approach the most suitable.
In order to apply the theory presented in Section 2.2 for the calculation of the first order wave forces, use of NEMOH will be made. NEMOH is the world's first open source Boundary Element Method (BEM) code developed in 2014 by Ecole Centrale de Nantes [76]. It is dedicated to the computation of first order wave loads on offshore structures. The approach it has adopted decouples the resolution of the linear free surface Boundary Value Problem (BVP) and the definition of the boundary condition on the body. In this way, it is easier to deal with flexible structures, hydroelasticity, generalized modes and unconventional degrees of freedom. However, for this project the analysis is restrained to rigid floaters. The BVP is solved in frequency domain with

the advantage of smaller computational time and sufficient accuracy. NEMOH can be separated into 3 different components with 3 different operations as follows:

- preProcessor: reads and prepares the mesh; prepares the vectors of body conditions; prepares the vectors of integration rules for the calculation of the forces
- Solver: for each vector of body condition solves the BVP for the potential; calculates the forces according to the integration rules; calculate the wave elevation and the far-field coefficients
- postProcessor: gives the hydrodynamic coefficients; generate files for the wave elevation

The outputs that NEMOH can produce are the following:

- Radiation coefficients
- Excitation force coefficients
- Diffraction force coefficients
- Froude-Krylov forces
- Impulse response force and added mass
- Visualization of the mesh

All the aforementioned elements are presented in the overview shown in Figure 3.11.

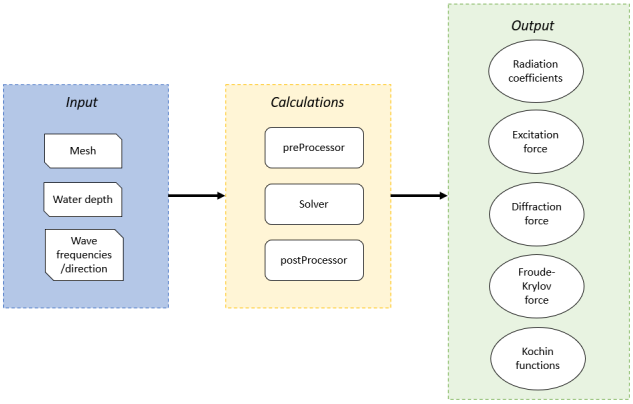

Figure 3.11: Overview of the work-flow of NEMOH

3.3.3 Kochin Function

Among the other post processing possibilities that NEMOH can offer, Kochin functions for every frequency and any angle resolution can be provided. The output files are stored in the format of Kochin.X.dat, with X corresponding to the frequency under examination (Figure 3.12). Again, it is important to note down that due to the structure of NEMOH, there are seven different output files, one for the solution of diffraction problem and six for every radiation problem. This file needs to be further processed in order to get the final horizontal drift forces. The different Kochin functions that stem from the solution of the radiation and diffraction potential need to be combined to generate the total Kochin function $H(\theta)$.
And this is the main input for the calculation of drift forces as described in Section 2.7.3, in combination with RAO as presented in the next Section.

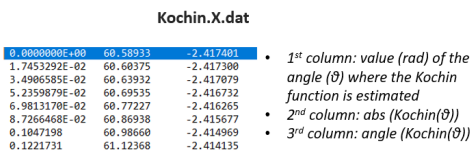

Figure 3.12: NEMOH output for Kochin functions

3.3.4 Response Amplitude Operator

As was presented in Section 2.2, the motions of two connected floaters in all 12 DoF can be described by Equation 2.45. However, it is common for the offshore applications to express the motion of a floating structure as motion per meter amplitude for a number of different frequencies. This can be performed through the so called Response Amplitude Operators (RAO) as expressed in Equation 3.11.

$$RAO(\omega) = |\frac{\tilde{u}}{\zeta_w}| = |\tilde{F_w} \cdot Inv(-\omega^2(M + A(\omega)) + i\omega B(\omega) + K_{conn})| \quad [m/m] \tag{3.11}$$

As it is obvious, the RAO contains information about the amplitude of the motion in all DoF per wave amplitude. All the results coming from NEMOH are already scaled with respect to the incoming wave. Besides the amplitude of the motion, another valuable element is the phase angle ϵ which expresses the phase difference of each motion with respect to the phase of the wave. The phase angle can be easily calculated with the use of Equation 3.12.

$$\epsilon(\omega) = arg(\frac{\tilde{u}}{\zeta_w}) = arg(\tilde{F_w} \cdot Inv(-\omega^2(M + A(\omega)) + i\omega B(\omega) + K_{conn})) \quad [rad] \tag{3.12}$$

3.3.5 Irregular Frequencies

When the a numerical tool is used to deal with a mathematical problem, it is possible that there are a few occasions where discrepancies may occur. This is also the case for the use of NEMOH. As it is explained in [31], an infinite number of of discrete frequencies cause the three-dimensional source technique to break down for a surface piercing body. These frequencies are called irregular frequencies and they do not capture a physical phenomenon, rather they consist an inherent problem of these kind of solvers. NEMOH requires the geometry of only the submerged part of the floating body, and this has a result that for these frequencies there is a fictitious fluid motion inside the body, with the same free-surface condition as outside the body. This results into a mathematical issue, since at the irregular frequencies, for the unknown source densities, the determinant of the coefficient matrix goes to zero when the number of unknowns goes to infinity. This consequently leads to large peaks in the calculated hydrodynamic coefficients as well as the force coefficients.
Until now, NEMOH has not been reinforced with a tool to deal with the irregular frequencies and therefore have to be manually removed during the post processing of the results. This can be easily achieved using Equation 3.13, as was introduced by [45].

$$\begin{aligned} &\widehat{\omega}_{\alpha\beta} = \sqrt{g\gamma \coth(\gamma T)} \\ &\gamma^2 = (\frac{\alpha\pi}{L})^2 + (\frac{\beta\pi}{B})^2, \quad \alpha = 1, 2, 3... \quad \beta = 1, 2, 3... \end{aligned} \tag{3.13}$$

Where L is the length of the rectangular box, B is the width and T is the draft.
After the identification of the irregular frequencies, the affected areas are removed during the post-processing of the results in MATLAB. After that, a smoothing function is used to interpolate the removed results. For this project, the build in function of smoothingspline is used, with the automatically selected smoothing parameter from the software itself. The importance of the removal of irregular frequencies will be also presented for the validation cases. However, for the floater used for the solar boat, the first irregular frequency is located out of the range of frequencies that are being analyzed as defined by its geometry.

3.3.6 Expansion of the Model

As it was mentioned multiple times until now, the fragmentation of the initial problem into smaller blocks was pursued, in order to have smaller and easy to deal with problems. This is why until now the two geometries analyzed have been a single floater and two connected floaters. Figure 3.13 presents the expansion of the simulation model that perfectly matches with the original solar boat.

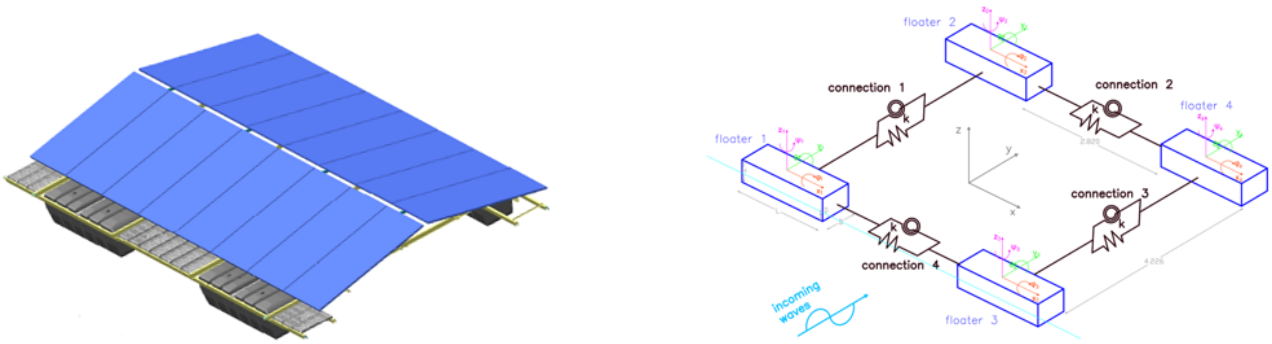

(a) Original solar boat (b) Simulation model

Figure 3.13: Expansion of the simulation model to full geometry

As it is now clear, the simulation model consists of 4 floaters with dimensions given in Table 3.8 and the corresponding horizontal offsets. Every floater is connected with the other two through a system of 6 springs as presented in Section 2.5, with very high stiffness which represents a rigid connection. The location of the main system of coordinates is selected exactly in the middle and plays an important role for the calculation of the resulting moments by NEMOH.
For the needs of this project, the only direction for the incoming waves that will be analyzed is perpendicular to x-axis. This assumption is required to guarantee that the execution time will stay within the limits of the project. However, it also leads to the higher wave loading and thus yields the most conservative results for the drift forces.

3.3.7 Drift Force Density

As was shown in Figure 3.7, the JONSWAP spectrum can be used to express the energy density of the wave in $[m^2 s]$ for every frequency analyzed. According to [39], this is described by Equation 3.14.

$$E(\omega) = \frac{1}{\Delta\omega}\frac{1}{2}\zeta_\alpha^2 \tag{3.14}$$

Where, $\Delta\omega$ is the frequency step used in NEMOH and ζ_i is the wave amplitude. From this relationship, the density of $\frac{\zeta_\alpha^2}{\Delta\omega}$ (Figure 3.14) can be generated with the appropriate transformations.

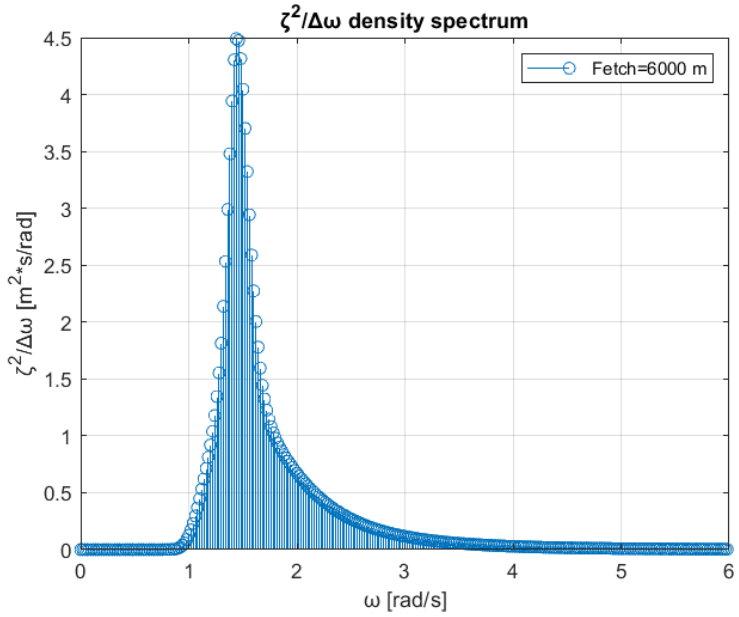

Figure 3.14: $\zeta_\alpha^2/\Delta\omega$ density spectrum

The far-field approach gives as output the Quadratic Transfer Function (QTF) of wave drift force expressed in $[N/m^2]$ for every wave frequency. Beginning from Equation 3.14, the components of drift force for every wave frequency can be defined as follows:

$$\begin{aligned} E(\omega) &= \frac{1}{\Delta\omega}\frac{1}{2}\zeta_\alpha^2 \\ \frac{\zeta_\alpha^2}{\Delta\omega} &= 2 \cdot E(\omega) \\ \frac{F_{drift}}{\Delta\omega} &= \frac{\zeta_\alpha^2}{\Delta\omega} \cdot QTF \\ F_{drift,total} &= \int_0^\infty \frac{F_{drift}}{\Delta\omega} d\omega \quad [N] \end{aligned} \tag{3.15}$$

The above formula shows that by using the wave energy density spectrum, it is possible to calculate the drift force at each wave frequency. Then, the total drift force is the summation of all individual components. This sequence of calculations is actually enabling to fully incorporate the local environmental conditions in the estimation of drift forces.

3.3.8 Overview of the Model

After reviewing all individual components, the overview of the model that this thesis is using to answer the main research question is provided in Figure 3.15.

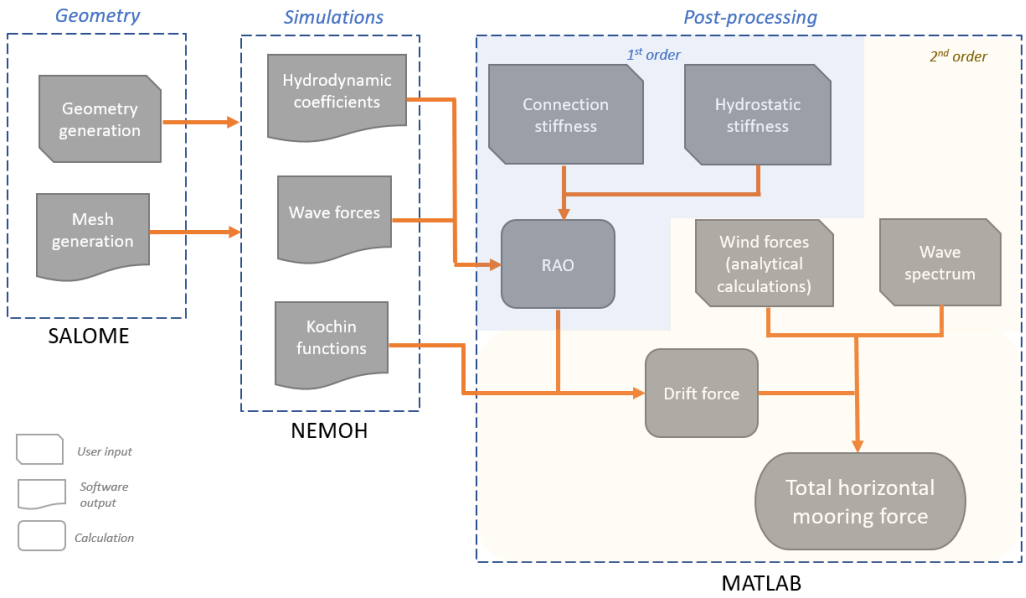

Figure 3.15: Overview of the workflow for the calculation of the horizontal mooring force

As becomes obvious from the figure above, the methodology is mainly divided into 3 sub-stages regarding the 3 different software used.
Initially the geometry is required as input in SALOME to generate the associated mesh. These two outputs are now used as input in NEMOH, which takes the next step and calculates hydrodynamic coefficients, wave exciting forces and Kochin functions.
The user has to manually insert the hydrostatic and connection stiffness matrices, which can be combined with the added mass and damping coefficients, as well as the wave exciting forces, to generate the RAOs for every wave frequency analyzed.
Now, with the RAOs already computed and the Kochin functions given as output from NEMOH, the two components of the horizontal drift force can be calculated with the far-field approach. The wind loads acting on the solar panels and the free board of the floaters are calculated with the use of analytical calculations.
The wave energy density spectrum can be transformed to wave amplitude square spectrum and the multiplication with the wave drift force QTF [N/m^2] yields the drift force spectrum distribution over the range of wave frequencies.
The total horizontal mooring force can be estimated as the summation of the wave drift forces and the wind forces. The last step is the comparison of this force with the forces already acting on the wind turbine, with a simultaneous check on the effect on the overturning moment.

4 | Validation

This chapter presents four different reference cases which were used for the validation of the model. These cases include: a single barge, two adjacent barges, two interconnected barges, drift forces with the far-field approach on a sphere and a barge. The selection of these cases has been done to follow the gradually expanded model. So, as it was already presented in Chapter 3, the first block is a single floater, the next one is two floaters placed in close proximity and the third one is two floaters mechanically connected. The last block is the calculation of the drift forces. By checking each building block of the model, it is reassured that the model is producing accurate and reliable results.

4.1 Validation for a Single Barge

For the first and second validation case, the reference data that was used come from a study performed by Sun et al. [97] and was focused on the analysis of the first and second order wave forces due to resonant waves between two adjacent barges. In addition, another boundary element method software called DIFFRACT was used for the generation of the mesh as well as the hydrodynamic calculations. The configuration that was used for the analysis is indicated in Figure 4.1. For the first validation case, the configuration includes only a single barge. The analytical properties of the rectangular boxes-barges are presented in Table 4.1. The inclusion of a term for additional roll damping was made to represent the effects of viscosity, and the value was calculated based on empirical models.

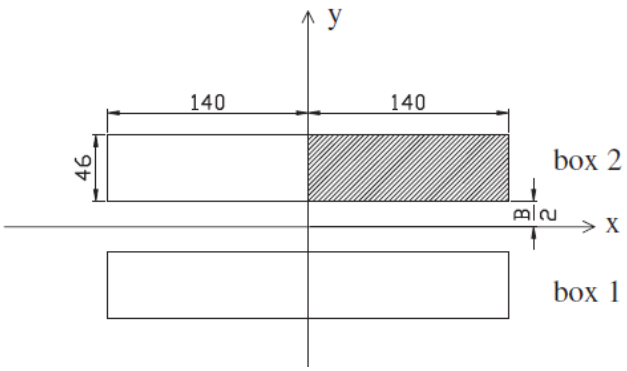

Figure 4.1: Configuration of the system for validations case 1 and 2 [97]

Property	Value	Unit
Length	280	m
Width	46	m
Draft	16.5	m
Vertical centre of gravity	16.5	m
Additional roll damping	$3.562 \cdot 10^9$	Nm/(rad/s)

Table 4.1: Properties of the barge for validation case 1

4.1.1 Convergence Study

The first action towards the validation of the results of the model regards the number of the panels. As was presented in Section 3.3.1, the generation of the mesh can be achieved with multiple number of panels that are given as input from the user. In order to check which number of panels gives sufficient results, different simulations were performed. As it is illustrated in Figures 4.2 -4.4, the number of panels has a significant effect on the calculated wave exciting forces. More specifically, the simulations were performed for 6 different total number of panels. The frequency range selected and presented here is the same as used in the original study. It is important to note down here that any increase in the number of panels is accompanied with a drastic increase in execution time. The corresponding execution time for every case is shown in Table 4.2.

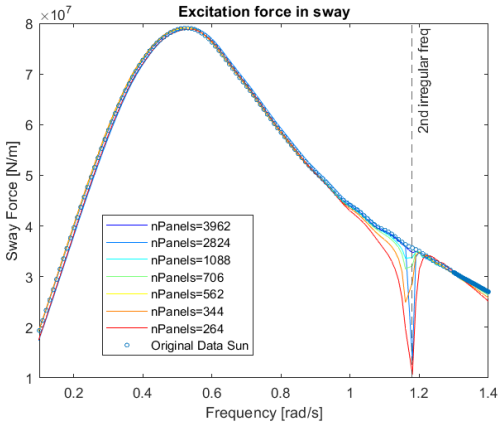

Figure 4.2: Convergence of sway force of a single barge

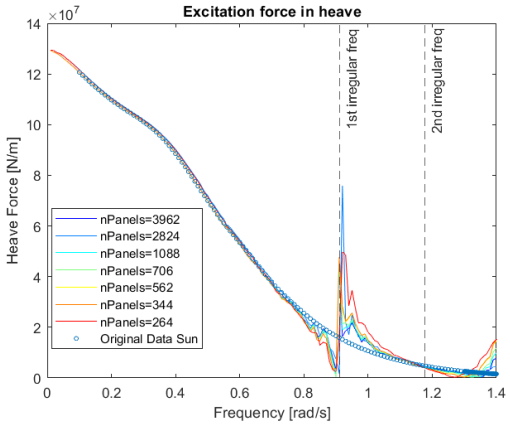

Figure 4.3: Convergence of heave force of a single barge

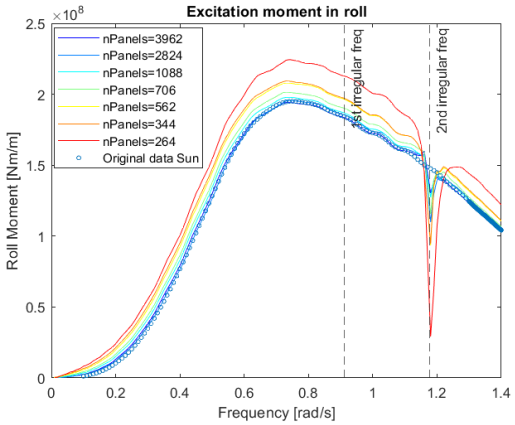

Figure 4.4: Convergence of roll moment of a single barge

Number of panels	Execution time (min)
264	2.6
344	3.0
562	3.6
706	6.2
1088	18.1
2824	180.1
3962	656.4

Table 4.2: Execution time for various number of panels

As is obvious from Figure 4.2 and Figure 4.3, the accuracy of model is not significantly influenced by the selected panels. There are however two areas where extreme discrepancies compared to the reference data

occur. As the dashed lines indicate these are the areas around the irregular frequencies and will be treated in Section 4.1.2. Now, if attention is turned to Figure 4.4, it is apparent that high inaccuracies are documented along the whole band of frequencies for every case of panels. After 1088 panels however, it looks like the results have converged and are in good agreement with the reference data.
If this observation is counter-checked with the data of Table 4.2, it is completely justified to select 1088 panels for the analysis. In the end, it is a trade-off between accuracy and computational time, with the case of 1088 panels being the most favorable. Therefore, results of following sections are generated for barges simulated with a mesh of 1088 panels. This number of panels results to division of length, width and draft to 56, 10 and 4 panels respectively. The minimum wavelength that corresponds to the maximum frequency $\omega = 1.4rad/s$ is 31m. This means that the ratio of the panel length (5m) over the minimum wavelength is 6.2.

4.1.2 Removal of Irregular Frequencies

As was already mentioned in Section 4.1.1, the areas close to irregular frequencies present high discrepancies with the reference data. In Section 3.3.5, the analytical equations for tracking down these frequencies were presented. With the use of these formulas, the first three irregular frequencies are found to be: 0.91rad/s, 1.17rad/s and 1.42rad/s. The most important value is the one of the first irregular frequency as it is certain that no more irregular frequencies will be found below this value. Another comment that seems interesting is that not every irregular frequency is influencing the excitation in every degree of freedom. So, sway force is affected by the second irregular frequency, heave force is affected by the first and third while roll moment is only affected by the second.
After the detection of the problematic frequencies, their values are removed and the data are smoothed with a built-in function of MATLAB as explained in Section 3.3.5. The results of the exciting forces on the barge, after the removal of irregular frequencies and for 1088 number of panels are presented in Figures 4.5-4.7. The results calculated from the model in NEMOH are in great agreement with the results published from Sun et al.

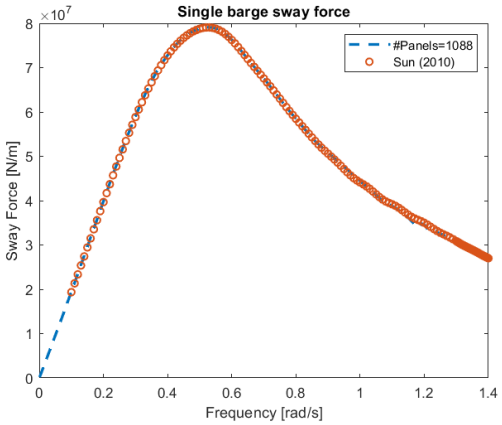

Figure 4.5: Sway force on a single barge

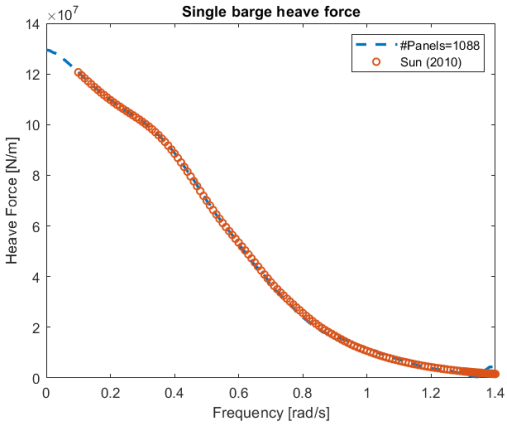

Figure 4.6: Heave force on a single barge

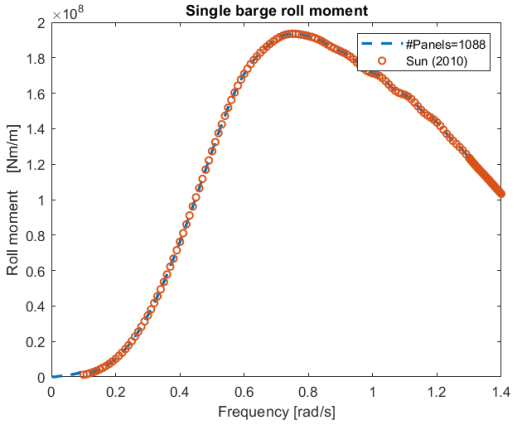

Figure 4.7: Roll moment on a single barge

4.1.3 RAOs of a Single Barge

After the validation of the wave forces that are exciting the barge, the next step includes the validation of the motions due to these forces. These motions are expressed through the response amplitude operators, which was thoroughly explained in Section 3.3.4. The RAOs give information about the motion of the barge at every DoF per wave amplitude. Figures 4.8 and 4.9 validate that the motions of the barge computed with NEMOH are in great agreement with the reference data. No comparison is possible for the roll RAO since data was not published for this.

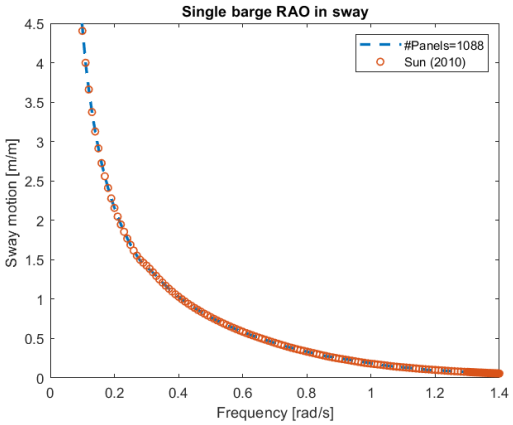

Figure 4.8: Sway RAO of a single barge

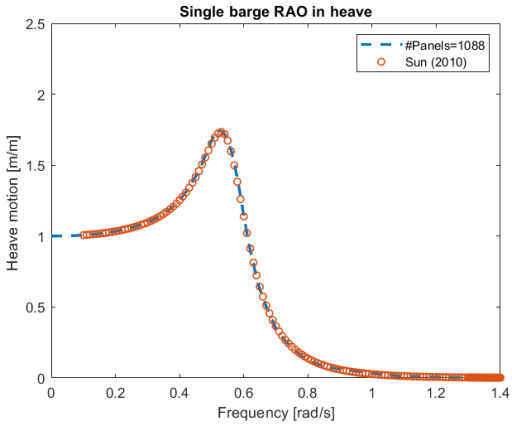

Figure 4.9: Heave RAO of a single barge

4.2 Two Adjacent barges

After verifying the accuracy of the model for the case of a single barge, the next building block towards the representation of the full solar boat, is the case of two barges placed in close proximity. The two adjacent barges share the same properties are presented in Table 4.1 and their configuration is shown in Figure 4.1. The spacing between the barges is set to be 18m. The purpose of this case is to capture the hydrodynamic interaction of two bodies when placed close to each other. At first, the comparison and the validation of the forces between a single and two adjacent barges is presented in Figures 4.10-4.12.

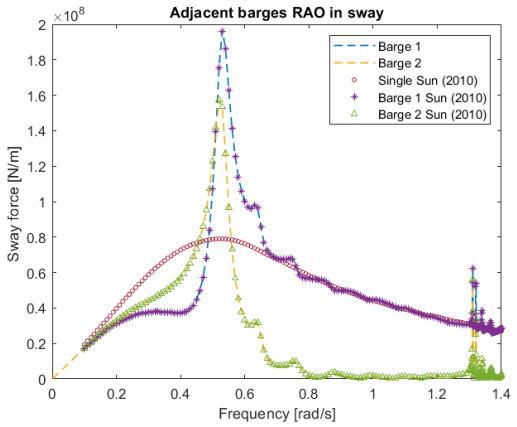

Figure 4.10: Sway force for a single and two adjacent barges

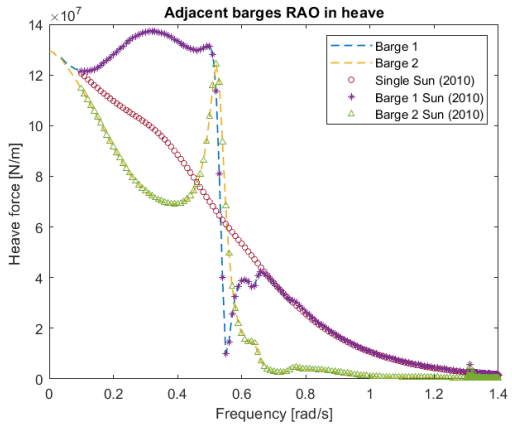

Figure 4.11: Heave force for a single and two adjacent barges

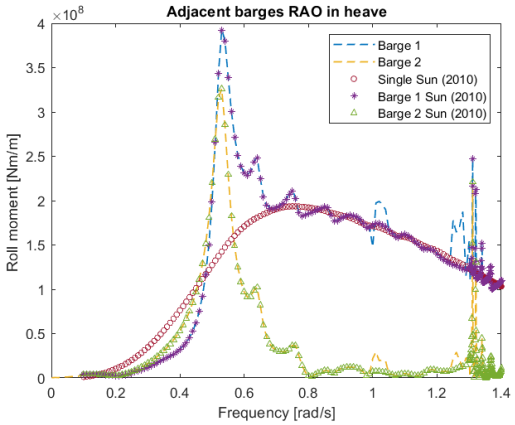

Figure 4.12: Roll moment for a single and two adjacent barges

First of all, the results of the figures above, show that NEMOH is correctly used for the case of two adjacent barges and the wave exciting forces are in great agreement. Moreover, a new peak about 0.58rad/s has occurred for sway force for the case of two barges. Barge 1 is the barge considered upwave of Barge 2 in this analysis. The value at the peak has became larger than double of the force acting on a single barge. Barge 1 is still experiencing about 16% larger horizontal force along y-axis as can be seen in Figure 4.10. Same peaks have been developed also for the heave force and roll moment. Interestingly enough, in both Figures 4.10 and 4.12, after the aforementioned pick, the second barge is experiencing almost zero excitation in sway and roll respectively. As the frequencies are increasing and thus the wave length is decreasing, it seems like the first barge is absorbing more energy of the waves and thus reducing the effect behind it. Even though this trend is continuing, a spike of excitation appears around 1.3rad/s. As it is explained in [97], this happens due to a trapped standing wave in the gap between the two barges.
Once the wave forces exerted on two barges have been validated, the next component that needs validation are the motions of the two barges. These motions are illustrated in Figures 4.13 and 4.14. Again, a comparison between a single and two barges is included. The RAO in roll has been left out since no reference data where included in the report published by Sun et al.

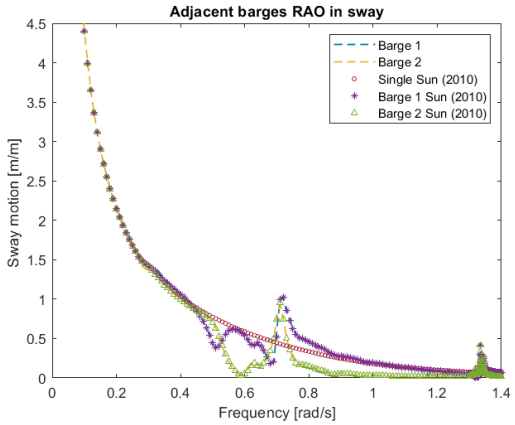

Figure 4.13: Sway RAO per wave amplitude for two adjacent barges

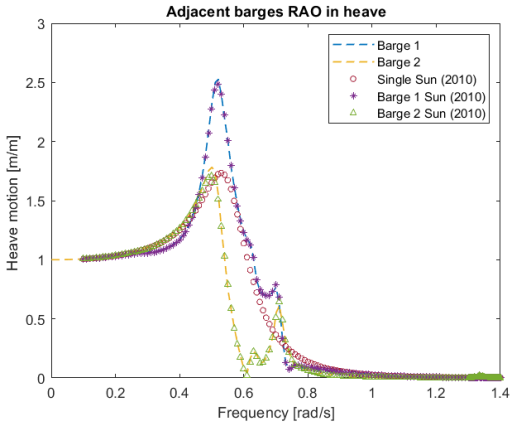

Figure 4.14: Heave RAO per wave amplitude for two adjacent barges

The results show that the case of two barges placed in small proximity has been correctly implemented through the model. Throughout the whole frequency range, the agreement of the published and calculated results is good. Next to that, the peak that was observed in the force plots is not influencing the motion in sway and only a higher vertical motion is noticed for the barge that is placed upwave.

4.3 Two Connected Barges

Until this point, the validity of the model has been checked for two cases: a single body and two adjacent bodies. The next block towards the representation of the full solar boat is the mechanical connection of two bodies. For this reason, a study published again by Sun et al. [96] and was mainly focused on the responses of interconnected floating bodies will be used for reference. Data made available by Newman in 1994 [77] are also included. The configuration of the system is presented in Figure 4.15. The barges are considered to have a rectangular shape and mass is distributed uniformly. Once again DIFFRACT has been used for meshing the geometries and the analysis is focused only in head waves (waves propagating along the x-axis).

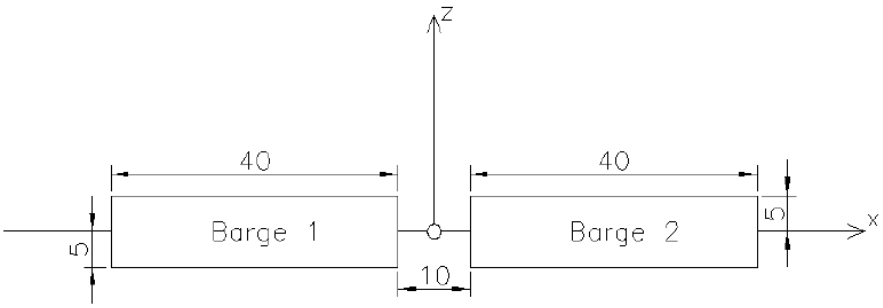

Figure 4.15: Configuration of the system for validation case 3 [96]

4.3.1 Hinge Connection

The first validation case regards the connection of the two barges with a bar of 10m length, which has a hinge half way along. As a consequence, it allows rotation around y-axis. In the model developed in this project where the connection is represented with the use of springs, this type of connection is achieved by setting the spring stiffness around y-axis to be zero. Figures 4.16 and 4.17 present the results of the model as well as the reference data. Figure 4.16 illustrates the vertical motion of the hinge per wave amplitude for a range of periods, while Figure 4.17 illustrates the vertical force acting on the hinge per wave amplitude. For the model, the middle point of the connection can be calculated using the motions of either barge 1 or barge 2. The figures include both results as a safety check that the springs model is correctly implemented. The results seem to be in good agreement.

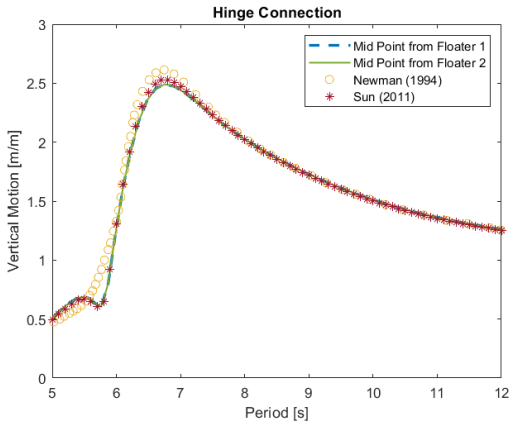

Figure 4.16: Vertical motion of hinge connection

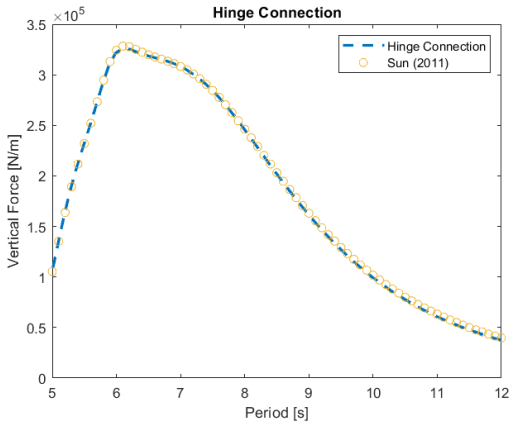

Figure 4.17: Vertical force of hinge connection

4.3.2 Rigid Connection

The second validation case regarding the connection regards a rigid connection. The methodology followed is the exact same as in Section 4.3.1. This time however, the stiffness of the rotational spring around y-axis is set to 10^9 rad/m in order to prevent any rotation. This type of connection is also the one that exists between the various floaters of the solar boat. The two same results concerning the motion and the force per wave amplitude

on the connection are presented in Figures 4.18 and 4.19. Finally, Figure 4.20 shows the interesting fact that the vertical forces at the connection are the same regardless of the presence or absence of the hinge. The vertical forces in the connection are the summation of wave exciting forces, inertia forces due to the responses of the vessels and finally due to hydrodynamic radiation forces. The wave forces remain the same for both cases. However, the other components are linked to modes of response that are either symmetric or anti-symmetric with respect to the vertical plane. Due to the symmetry of the geometry of the problem, the responses in the symmetric and anti-symmetric modes are coupled. The insertion of the hinge on the plane of symmetry only affects the symmetric modes of response. The vertical force however is only affected by the anti-symmetric modes and therefore the force is unaffected.
In conclusion, computed results of the model are in good agreement with the reference data.

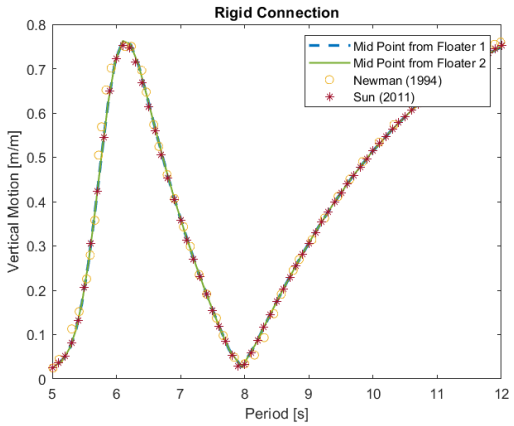

Figure 4.18: Vertical motion of rigid connection

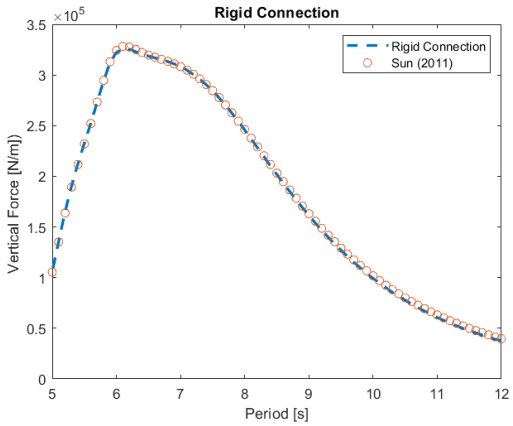

Figure 4.19: Vertical force of rigid connection

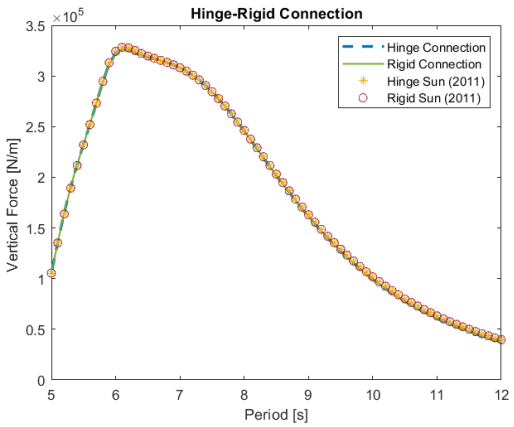

Figure 4.20: Vertical force on a hinge and a rigid connection

4.4 Drift Forces

The last validation case regards the calculation of the drift forces with the use of the far-field approach. A thorough explanation of the approach as well as the formulas that govern it can be found in Section 2.7.3. Two different cases were selected to compare the results and these are a floating sphere and a barge.

4.4.1 Drift Forces on a Sphere

The first case entails a floating sphere with a radius of 1m located in water of infinite depth. The reference data were published from Kudou in 1977 [58] and were calculated with the use of analytical formulas. For the hydrodynamic simulations, 1580 panels were used, which resulted to a ratio of minimum wavelength over panel length (0.05m) equal to 49.4 (compared to 6.2 for the single barge). As Figure 4.21 confirms, the model

is correctly predicting the drift force acting on the sphere. The vertical axis is has been normalized and is non-dimensional while another normalization has been used for the horizontal axis as the multiplication of the wave number k with the radius of the sphere R.

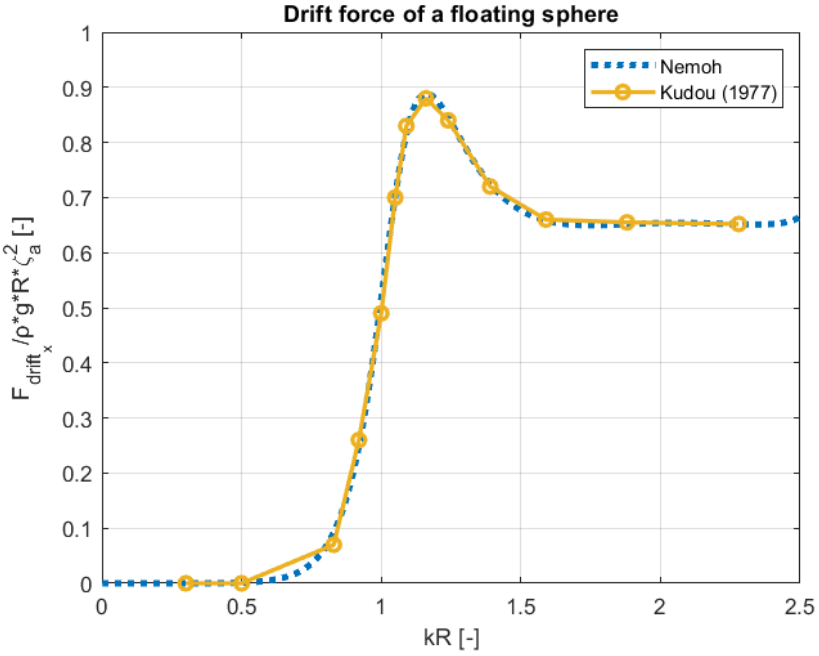

Figure 4.21: Drift forces on a floating sphere

4.4.2 Drift Forces on a Barge

Another case used for the validation of the model is the one of barge exposed in head waves as published by Pinkster in 1980 [79]. In his study he used analytical formulas of the near-field approach which he verified with experiments. The barge has a length of 150m, a width of 50m, a draft of 10m and a displacement of 73,750m^3. The results were produced for a water depth of 50m and the directions of the waves was perpendicular to y-axis (head waves). Figure 4.22 presents the comparison of the computed and the reference data in terms of normalized drift force expressed in Newtons and a normalized frequency expressed in rad. The normalization was kept the same as published by Pinkster. For this analysis, the number of panels were 1368 and this resulted to a ratio of minimum wavelength (15.41m) over panel length (2m) equal to 7.7.

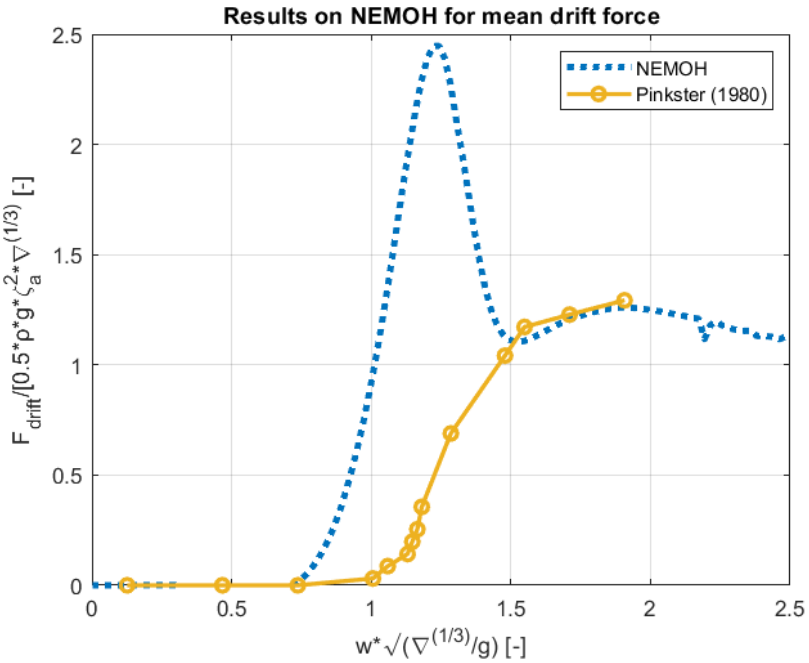

Figure 4.22: Drift forces on a barge at head waves

As it is becoming directly obvious from Figure 4.22, the results of the model are not precisely coinciding with the reference data. The two main observations here are: a mismatch in the maximum drift force and a mismatch in the frequency where the maximum occurs. More specifically, the reference data recorded a maximum normalized drift of 1.29 while the results of Nemoh recorded the maximum value at 2.42. As far as the peak frequency is concerned, results of Pinkster show a normalized peak frequency at 1.91rad while Nemoh shows at 1.22rad. If these values are converted again back to frequencies a value of 0.93rad/s and 0.59rad/s occur respectively. The explanation for this discrepancy in this case was not able to be found. For the case of the floating sphere analyzed in Section 4.4.1, the computation of the RAOs was performed in an uncoupled fashion since the motions of the sphere are not coupled due to its symmetric geometry. This was not possible to be applied for the case of the barge. Another possible source of error is that the affect of the phase angle of each RAO was not captured correctly due to the inherent conventions of Nemoh.
Despite the fact that the validation of the drift forces on the barge was not completely successful, it is considered that it gives a good estimation of the order of magnitude of the forces. Therefore, the far-field approach is still applicable in this project for the estimation of the drift forces. However, special attention should be paid in later stages of the design to reassure that the calculated second order forces are reliable. The two sources of error, maximum value and peak frequency, are selected to be two parameters in the simplified sensitivity analysis which follows. In this way, the effect of these errors can be quantified. As a concluding remark, any further analysis should have as a prerequisite the correct implementation of the far-field approach.

5 | Results

In this chapter, results regarding first order and mean drift wave forces will be presented. The different blocks concern the following geometries: a single floater, two adjacent floaters, two connected floaters, four adjacent floaters and four connected floaters. These five different blocks have been selected to gradually create the full geometry of the solar boat. The intermediate steps have also been validated in Section 4, so that concrete results are obtained. At the end of this chapter, a comparison is made between the potential mooring force and the already existing wind turbine forces. For this comparison, five different scenarios are selected to estimate the impact of different components

5.1 Single Floater: 1st Order Wave Forces

The dimensions of the floater are given in Table 3.8. The waves considered in this analysis are beam waves and therefore the resulting forces are almost exclusively excited in sway, heave and roll. The frequency range is selected to be from 0 to 6rad/s as this is where energy from the waves is expected according to Figure 3.7. Figures 5.1-5.3 illustrate the convergence study performed for the case of a single floater for 4 different meshes. The selected numbers were 416, 778, 1368 and 2019 panels respectively. And their corresponding execution times: 4.75, 12.3, 45.75 and 114.7mins. The number of panels selected to be used further in the analysis is 1368, as the results have already converged for this number and has also an execution time that will allow for the expansion of the model to more complicated systems.

One thing to note down here is that there are no irregular frequencies present in the analyzed frequency range. And this is also confirmed by the analytical formulas which predict the first irregular frequency at 7.5rad/s. Therefore, no special treatment is required here to identify and smoothen the influenced areas. As was analytically presented in Section 3.3.5, the irregular frequencies are a function of the dimensions of the floating body and the incoming wave length. Apparently, the floater is so small that these frequencies only appear for very short wave lengths.

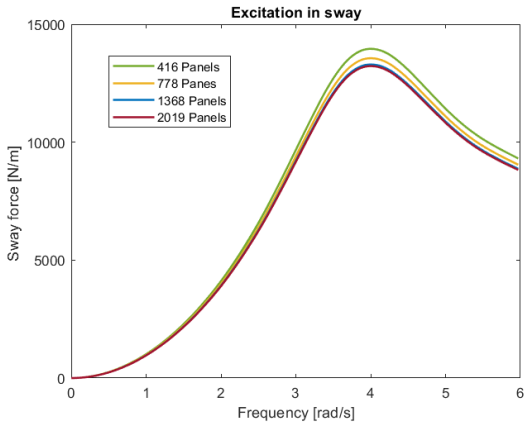

Figure 5.1: Convergence of sway force on a single floater

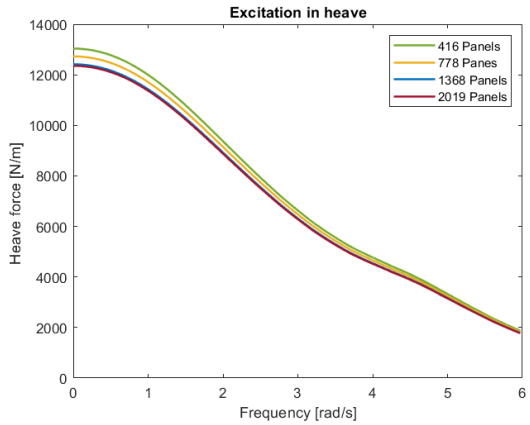

Figure 5.2: Convergence of heave force on a single floater

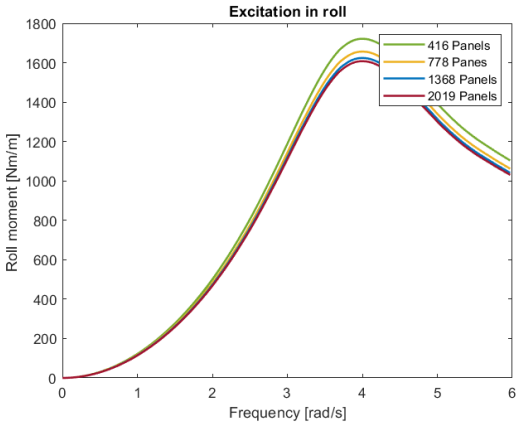

Figure 5.3: Convergence of roll moment on a single floater

After the calculation of the wave exciting forces and the selection of the number of panels, the calculation of the motions of the floater per wave amplitude can follow according to the EoM. It was selected to use 1368 panels for the analysis of the floater. This corresponded to 42, 12 and 8 panels in length, width and draft. The analyzed frequency range yields a minimum wavelength of 1.71m. Therefore, the ratio of the minimum wavelength over the panel length (0.05m) is equal to 34.2, compared to a value of 6.2 used for the single barge. These motions are presented in Figures 5.4-5.6.

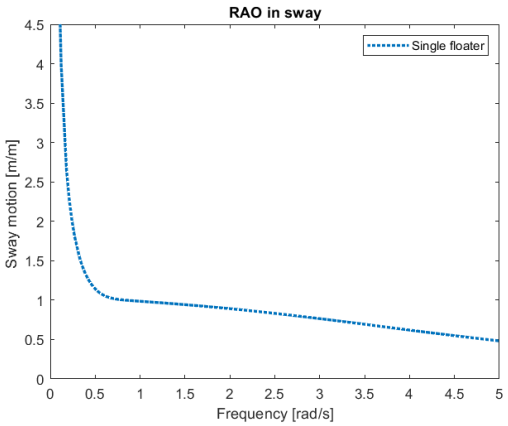

Figure 5.4: Sway motion of a single floater

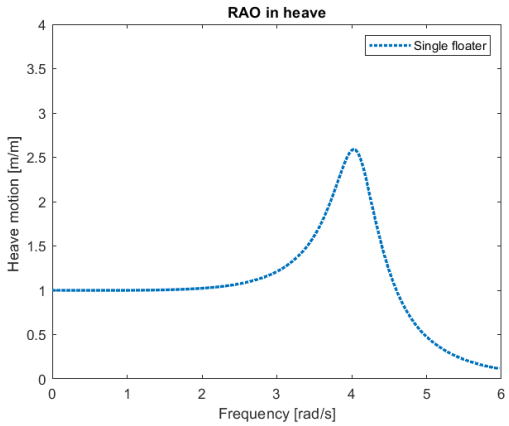

Figure 5.5: Heave motion of a single floater

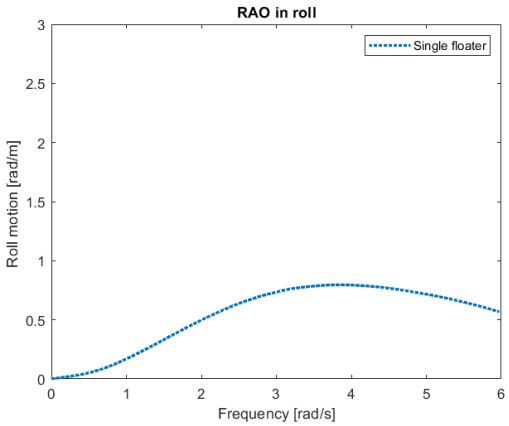

Figure 5.6: Roll motion of a single floater

From the figures above, it is obvious that the maximum vertical motion occurs at about 4rad/s while for the case of a single barge this peak was at 0.53rad/s (Figure 5.5). These peaks should correspond to the eigenfrequencies of the system in the respective motion given by the formula:

$$\omega_{33} = \sqrt{\frac{c_{33}}{m + a_{33}}} \ [rad/s] \tag{5.1}$$

Using Equation 5.1 and data produced by NEMOH for the added mass as well as computed data for the mass and the hydrostatic stiffness in heave, the following values are generated: 4.03rad/s for the floater and 0.54rad/s for the barge. This is a check that confirms that the generated plots are correctly capturing the physics of the problem. This big shift in the frequency where the heave peak occurs is correlated to the incoming wave length. Higher frequencies correspond to shorter waves. For the case of the barge, which has a width of 46m the resonance occurs at low frequencies and thus long waves. More importantly, the area around the natural frequency is characterized by motions dominated by the damping term. This means that high resonance can be expected when damping is small. After the peak, the waves are getting smaller compared to the width of the structure and consequently lose their influence. This is also true for the floater, but now the peak only occurs after 4rad/s when the length of the waves has already dropped too much. Until that point, the floater is too small that is just following the elevation of the wave. Taking a look at the ratio of the wave length to structure width, the following numbers occur: 4.8 for the barge and 6.6 for the floater. So even though the resonance for the floater occurs at a very smaller wave length, the ratios do not match perfectly.

5.2 Adjacent Floaters: 1st Order Wave Forces

The next block after the computation of the first order wave forces and the corresponding responses of a single floater is the expansion to two adjacent floaters. The distance at which these floaters are placed is regulated by the dimensions of the solar boat and is equal to 4.226m from the inner sides of the floaters. As was already noticed in Section 4.2, there is strong interference between the two bodies when placed in small proximity. Figures 5.7-5.9 present a comparison of the excitation forces for the case of a single and the case of two adjacent floaters.

It is reminded here that floater 1 is placed upwave of floater 2, so it is the one confronting first the wave. Starting with Figure 5.7, the maximum sway force that occurs now for the first floater reaches up to 19.7kN/m at a frequency of 4.2rad/s. The maximum horizontal force for the second floater is also present at the same frequency but has an amplitude of 14.2kN/m. For the case of the single floater the maximum force is 13.3kN/m and occurs at a frequency of 3.97rad/s. So, an increase of 48% and 6.7% is recorded for floater 1 and floater 2 respectively. Additionally, a periodic appearance of new peaks and troughs is recorded. Table 5.1 contains information on these frequencies, the corresponding wave lengths and the ratio of these lengths over the width of the structure.

Peak frequency [rad/s]	Wave length [m]	Wave length/Width of the floater [-]
3.45	5.18	8.81
4.17	3.54	6.02
4.89	2.58	4.39
5.52	2.02	3.44

Table 5.1: Sway peaks for two adjacent floaters

If the values of the last column of Table 5.1 are compared with each other, an almost constant factor of 1.37 is found. So, it seems that the peaks in sway force can be traced back as multiples of the ratio of the incoming length over the width of the structure.

Figure 5.8 gives an overview of the heave forces exerted on the two floaters with however small increase in amplitude compared to the case of a single floater. Once again, the first floater experiences about 20% higher forces at the peaks that are occurring again due to the interaction of the bodies. These peaks do not correspond to the same frequencies as in sway and are not as narrow.

Finally, for the case of excitation in roll as presented in Figure 5.9, the behavior is the exact same as sway force with the maximum moment for floater 1 being 50% larger compared to the single case. The increase in maximum excitation in roll for floater 2 is only about 6%.

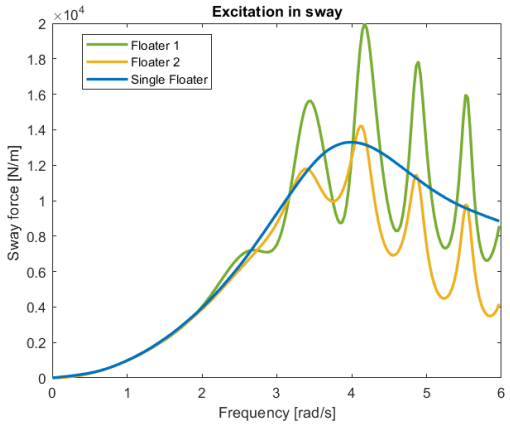

Figure 5.7: Sway force on a single and two floaters

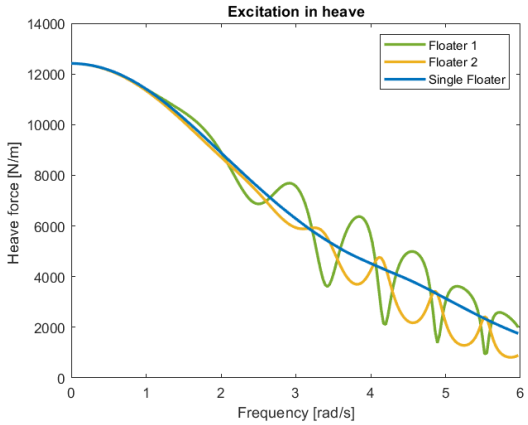

Figure 5.8: Heave force on a single and two floaters

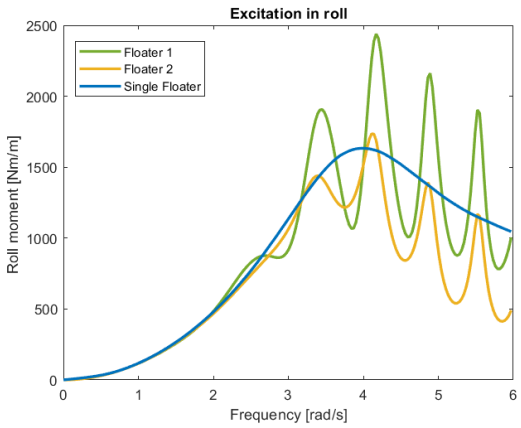

Figure 5.9: Roll moment on a single and two floaters

Moving a step forward, after getting the excitation forces, the computation of the relevant responses of the floaters is presented in Figures 5.10-5.12.

Starting with Figure 5.10, the general behavior of the floaters is the same in both cases. However, after 3.6rad/s there is a significant reduction of approximately 50% in the response of the downwave floater. The upwave floater seems to oscillate around the sway motion of the single floater with values differing up to 30%. Moving to Figure 5.11, the main focus is being drawn to the maximum vertical motion. For the case of the single floater the maximum response is 2.59m per wave amplitude. For the case of two adjacent floaters, floater 1 is recording a maximum vertical motion of 3.67m/m and floater 2 of 2.94m/m. So, there is an increase of 42% and 14% for the upwave and downwave floater respectively. After the occurring peak in heave however, floater 2 is presenting smaller responses compared to the case of a single floater.

Finally, the RAO in roll according to Figure 5.12, presents the same trends as sway, with decreased motions of floater 2 after the frequency of 3.6rad/s. Again, the amplitudes of the motions of floater 1 are oscillating around the values of the single floater. To conclude, all the three aforementioned figures demonstrate that the upwave floater is operating as a wave attenuator for the second floater which is excited significantly lower. Interesting is the fact that the responses of floater 1 are exceeding those of a single floater and this can related to the radiated and diffracted waves coming from floater 2, creating a complex wave field in the gap.

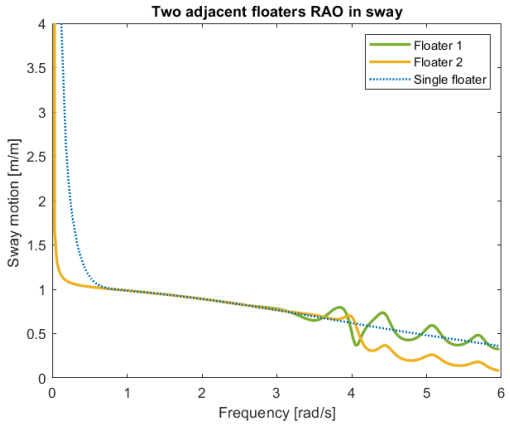

Figure 5.10: Sway RAO on a single and two floaters

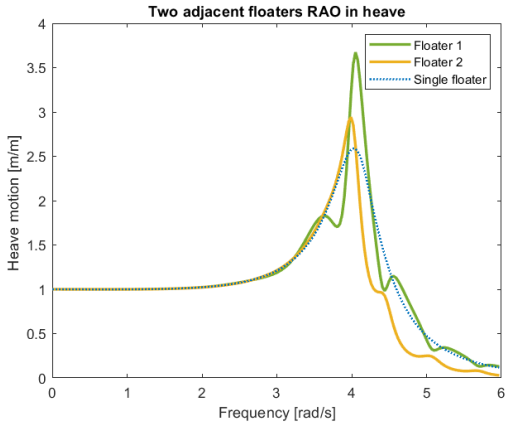

Figure 5.11: Heave RAO on a single and two floaters

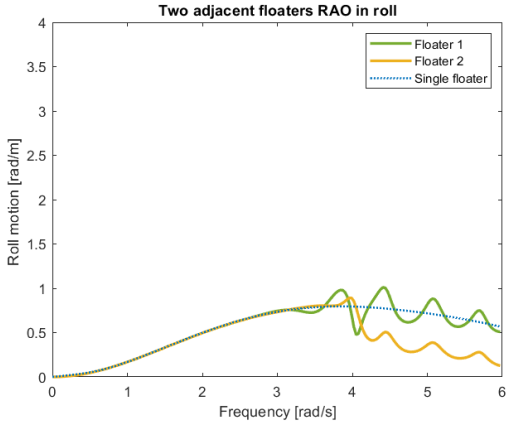

Figure 5.12: Roll RAO on a single and two floaters

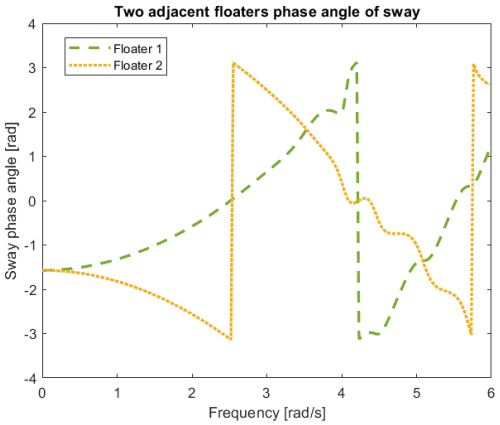

Figure 5.13: Phase angle of sway for two adjacent floaters

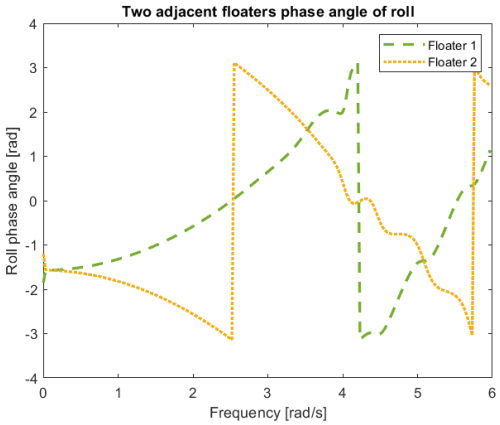

Figure 5.14: Phase angle of roll for two adjacent floaters

Figures 5.13 and 5.14 illustrate the phase angle of sway and roll motion respectively. This is done in an attempt to identify a potential connection between the peaks and troughs present in Figures 5.10 and 5.12. The phase angle is expressed in rad for every frequency analyzed in this report. However, no clear conclusions can be formed from these figures.

5.3 Two Connected Floaters: 1st Order Wave Forces

After presenting the results for the case of two adjacent floaters, the next block is the mechanical connection of these floaters. In this case, the hydrodynamic simulations are the exact same. However, during the post-processing of the results, the stiffness matrix of the connections is added as a new component in the EoM. The analytical explanation of this procedure has been performed in Section 2.5. For that reason, the presentation of the wave exciting forces is not needed since they are the same. However, the addition of the connection through the very stiff springs has a significant influence in the resulting responses. These responses are illustrated in Figures 5.15-5.17. In these figures the results both for the case of two adjacent floaters and the case for two adjacent connected floaters are included, to draw some conclusions on the effect of the connection.

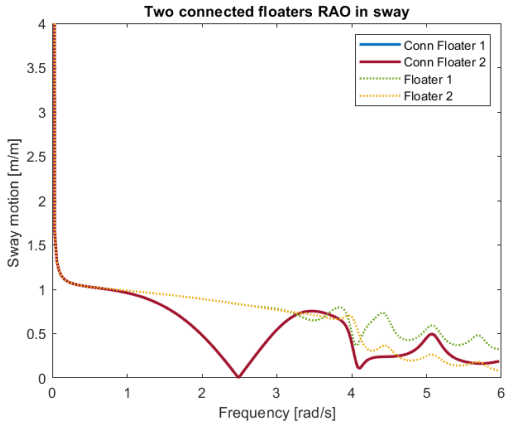

Figure 5.15: Sway RAO on two connected floaters

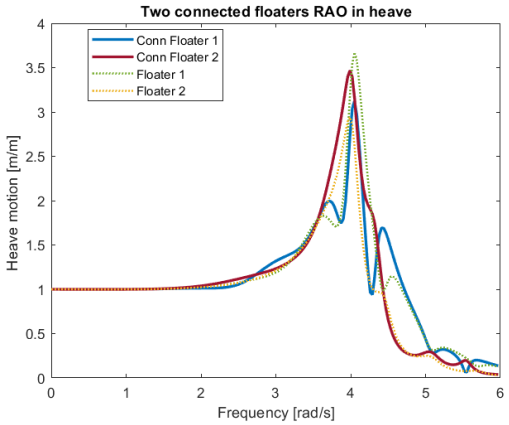

Figure 5.16: Heave RAO on two connected floaters

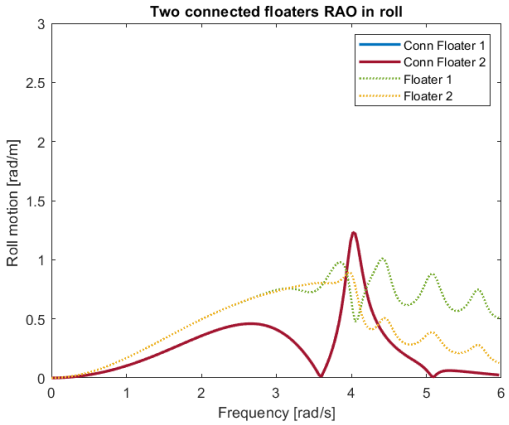

Figure 5.17: Roll RAO on two connected floaters

Starting with Figure 5.16 and the vertical response of the two floaters, it can be said that the behavior of the floaters has not been significantly affected. A 6% decrease in the maximum heave motion has been recorded for the upwave floater while a 13% decrease occurred for the downwave floater. Despite the connection, the floaters were free to move vertically independently due to the phase difference of the incoming wave in the motions.

Figures 5.15 and 5.17 are perfectly capturing the addition of the connection. As it can be noticed from these figures, the two connected floaters are now moving as a rigid body. The response in sway is now the same for the two floaters, with the remarkable fact that for some frequencies the motion is completely canceled. More specifically, at 2.49rad/s the system is experiencing zero sway motion and at 4.11rad/s the sway motion is only 0.1m per wave amplitude. This comes a result of the complicated interaction of the two bodies and the difference in the phase of the exciting forces. Let's take a look now at the phase angle of sway for the two bodies (Figure 5.18).

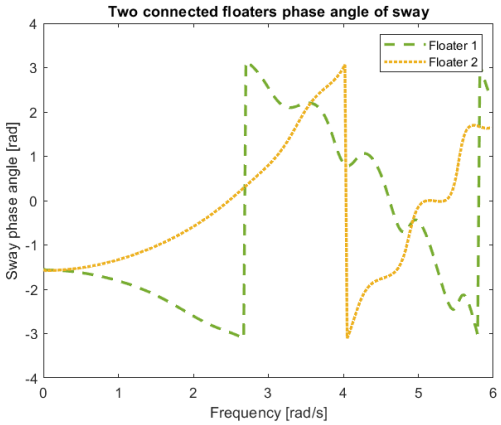

Figure 5.18: Phase angle of sway for two floaters

The two frequencies that present interest from this figure are at 2.6rad/s and 4.1rad/s, as these are the frequencies where the force is changing direction. The second value is the exact same where the high decrease is observed in Figure 5.15, while the first value is slightly larger (2.6 compared to 2.49). Even though it has not been completely proven, the change of the signs in the phase angle is a good indicator for the behavior of sway motion.
Focusing now on Figure 5.17, the same behavior is now observed for the response in roll. The connection is now forcing the two floaters to rotate together as a rigid body. The general response has decreased compared to the case of two not connected floaters, with a slight increase of about 15% in the peak value at 4rad/s. Again, there are two frequencies for which the motion is completely canceled: at 3.6 and 5.1rad/s. Figure 5.19 is again illustrated to check if something noticeable happens at these frequencies. However, the results presented do not demonstrate any correlation between these cancellations and the phase angle of roll.

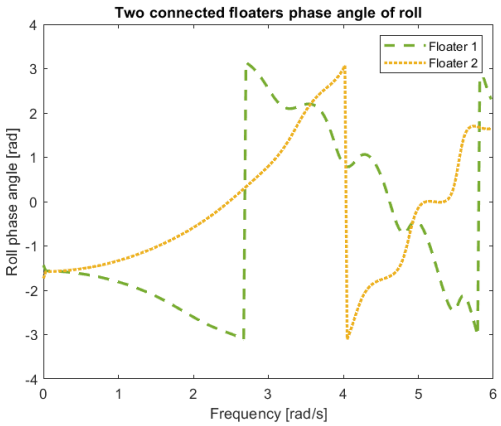

Figure 5.19: Phase angle of roll for two floaters

5.4 Four Adjacent Floaters: 1st Order Wave Forces

The next block in the representation of the full geometry is the simulation with four adjacent floaters. The exact configuration of the model can be found in Section 3.3.6. The offset in x direction is 2.82m while the one in y direction is 4.226m.
Figures 5.20-5.22 illustrate the comparison of the wave exciting forces for the case of two and the case of four adjacent barges.

The first comment that has to be made after the presentation of these figures is that in the configuration with the four floaters, the two upwave floaters 1 and 3 as well as the two downwave floaters 2 and 4 experience the exact same excitation. This happens because the wave direction analyzed here is along the y axis, the presence of a second row of floaters along the x axis does not influence the wave field. However, the hydrodynamic interaction is captured since the results are different from the case of the two floaters.

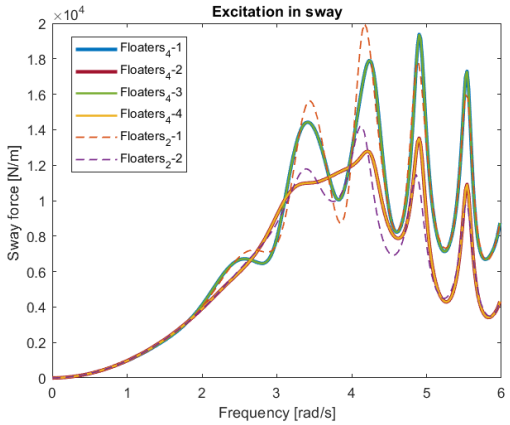

Figure 5.20: Sway force on 4 and 2 floaters

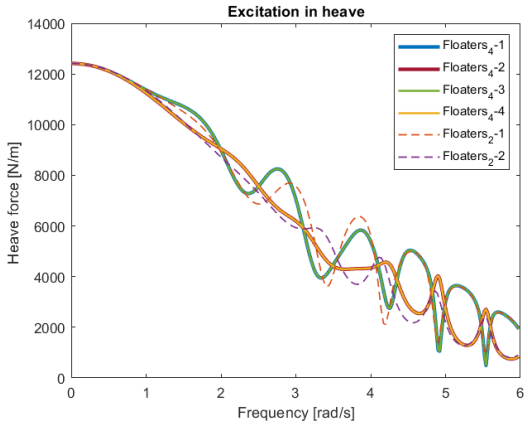

Figure 5.21: Heave force on 4 and 2 floaters

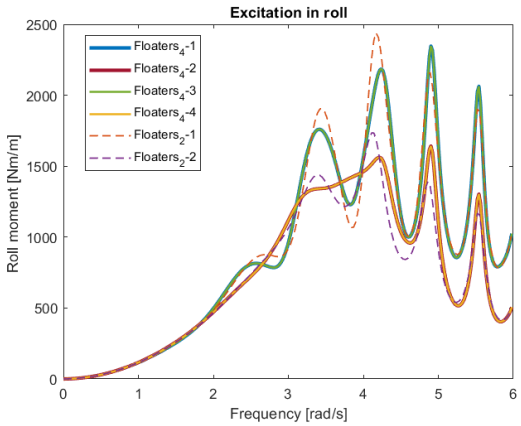

Figure 5.22: Roll moment on 4 and 2 floaters

Starting from Figure 5.20, the maximum force in sway for the case of 4 floaters and the first row of floaters (floaters 1 and 3) is occurring at 4.9rad/s and is only 3% smaller than the case of two floaters. For the second row of floaters (floater 2 and 4) the maximum excitation is occurring again at 4.9rad/s with an amplitude 5% lower than the case of two floaters. The general trend for the sway force shows that the presence of two extra floaters is reducing the sway forces, in a very low degree.
Figure 5.21 shows the comparison of heave excitation for two and four floaters. The oscillations of the amplitude do not allow for any safe conclusion. However, it is noticeable that after a frequency of 4rad/s the vertical forces of the four floaters are starting to converge with the case of two floaters. This can be explained by the fact that the wave lengths are becoming so small that the interaction along x-axis is no longer impactful.
Figure 5.22 presents the excitation around y-axis for the two cases of two and four adjacent floaters. The behavior of the excitation is similar to the excitation in sway (along y-axis). For the case of four floaters and the first row of floaters, meaning floater 1 and 3, the maximum roll moment reaches up to 2.3kNm per wave amplitude. The same value for the upwave floater in the configuration with two floaters is at 2.4kNm per wave amplitude. Only a slight decrease of 4% is recorded between the two cases. The maximum roll moment for floaters 2 and 4 reaches up to 1.6kNm/m. For the case of two floaters, this value is 1.7kNm/m. Therefore, a small decrease of 6% is recorded. In conclusion, the presence of two extra floaters is slightly decreasing the excitation in roll. Once again, as the frequency is increasing and the wave length is decreasing, the two cases are starting to converge.

The final block regarding the first order wave forces is the calculation of the RAOs for the four connected floaters. This is presented in Figures 5.23-5.25. The results of the previous analysis of the case of two connected floaters are also illustrated to allow for a comparison with an additional row of floaters.

Regarding sway motion, as presented by Figure 5.23, only two lines are visible because the connection has forced both of the configurations to move as a rigid body along the y axis. Moreover, for both the case of two floaters as well as the case of four floaters the horizontal motion is almost identical for the whole range of frequencies analyzed.

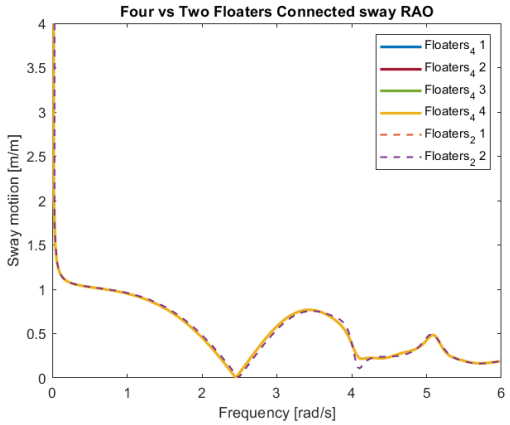

Figure 5.23: Sway RAO on 4 and 2 connected floaters

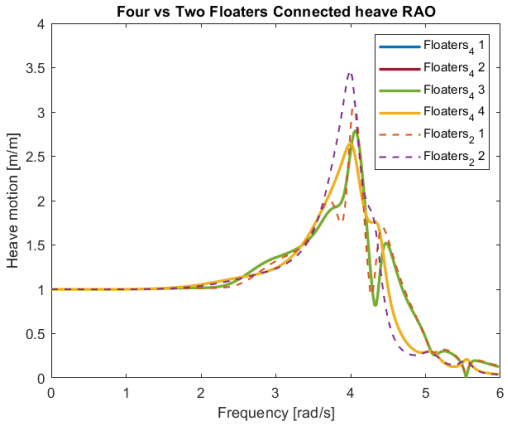

Figure 5.24: Heave force on 4 and 2 connected floaters

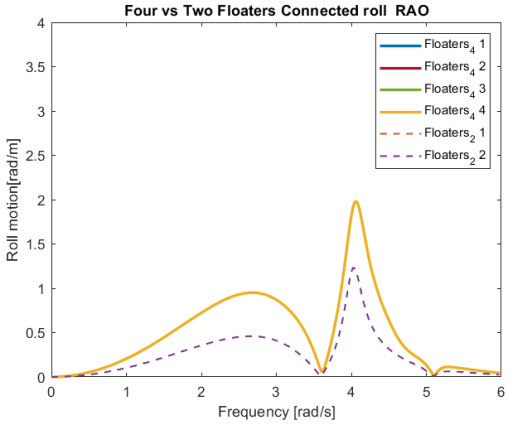

Figure 5.25: Roll RAO on 4 and 2 connected floaters

Figure 5.24 shows that for the case of four connected floaters, the first row (floaters 1 and 3) and the second row (floaters 2 and 4) are oscillating together. When it comes to the comparison with the case of two connected floaters a decrease in maximum amplitude is observed. More specifically, the upwave row of floaters presents 12% lower motion at resonance. Next to that, the downwave row of floaters shows a decreased peak in heave RAO by 24%. In general, for the case of the four connected floaters the four floaters have almost the same maximum vertical displacement.
Finally, for roll motion presented in Figure 5.25, it is obvious that the configuration of the four floaters is recording higher motions. The maximum rotation around x axis has been increased by 60% and this reveals a significant impact of another row of connected floaters. The motions are still canceling out at the frequencies of 3.6 and 5.1rad/s.

The last set of figures marks the end of the analysis regarding 1st order wave forces. A thorough presentation of the effect of adding more floaters in close proximity has been performed. The mechanical connections have been implemented correctly and the connected floaters are moving as a rigid body. This means that motions along y axis and rotations around x axis are the same for all the four floaters of the solar boat.

5.5 Drift Forces

This section is focusing on the presentation of the results regarding the second order mean drift force. The background and the formulas governing the far-field approach were explicitly treated in Section 2.7.3. Again the cases presented here will correspond to the building blocks of the model and the will include drift forces on a single floater, two floaters, four floaters as well as a comparison with a reference barge.

5.5.1 Single Floater: Drift Force

Starting with the case of a single floater, Figure 5.26 illustrates the horizontal drift force along the y-axis, since the component along x-axis is zero due to the 90° incoming waves. The force is expressed Quadratic Transfer Function (QTF) of the wave drift force, expressed as drift force per wave amplitude squared and is given for the analyzed range of frequencies from 0 to 6rad/s. This come as a consequence of the fact that the RAOs were analyzed within this range, and that was the input for the calculation of drift forces. Additionally, almost no wave energy is expected after 6rad/s and therefore the analysis is considered sufficient. Figure 5.27 contains the normalize drift force using the displacement ∇ of the floater for the normalization factor. A similar normalization has been performed for the horizontal axis of frequencies. The purpose of this normalization is to later compare how the drift forces are affected by the submerged volume of the configuration.

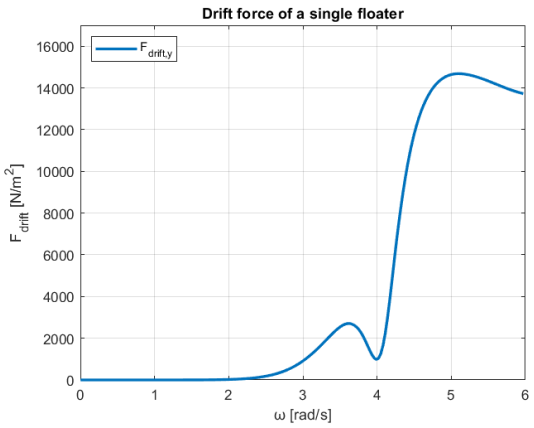

Figure 5.26: Drift force on a single floater

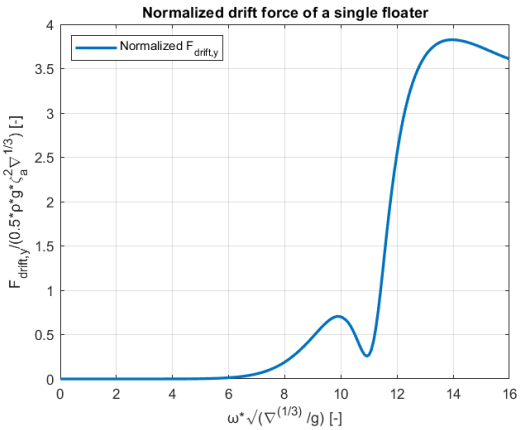

Figure 5.27: Normalized drift force on a single floater

From Figure 5.26, a maximum value of 14.7kN/m^2 for the horizontal drift force is recorded. The frequency where this peak occurs is at around 5.1rad/s. Interestingly enough, almost zero force is expected for frequencies below 3rad/s. So long waves mainly affect the first order excitation while drift forces are increasing as the waves are getting shorter. After the normalization, the peak value is now 3.82 according to Figure 5.27.

5.5.2 Two Floaters: Drift Force

Scaling up from a single to two floaters, the results are illustrated in Figures 5.28 and 5.29. In these figures, both the results for connected and not connected floaters are included, to draw some conclusions regarding the influence of the connection on the drift force. Starting from the maximum drift force, it is recorded that the peak value is 28.9kN/m^2 for the adjacent floaters and 29.94kN/m^2 for the case of connected. The corresponding frequencies where the maximum occurs are 4.95 and 5.1rad/s respectively. The overall behavior of the drift force for the two cases is that there is a small reduction between the frequencies 4-6rad/s for the configuration of the connected floaters while the maximum value is remaining almost the same. The normalized drift force has now increased to 5.98 for the adjacent floaters and 5.92 for the connected floaters. These values are almost 56% larger than the normalized forces of the single floater. For the maximum drift force, the results show that the addition of one extra floater in the analysis, impacted the maximum value by almost doubling it. The exact increase was found to be 97%, indicating nearly a linear relation.

5.5.3 Four Floaters: Drift Force

The last case regards the four floaters, both connected and not. Results are presented in Figures 5.30 and 5.31. The plots look almost identical for the case of the two floaters with a logical increase in amplitude for the drift force. More specifically, for the case of the connected floaters, the maximum values has climbed up to 65.46kN/m^2, in comparison to 29.94kN/m^2 for the two connected floaters. This is an increase of 126% confirming thus that the relation of drift force with the displaced volume is not linear. The frequency at which the maximum occurs is 4.94rad/s, perfectly matching with the peak frequency of the two floaters. When looking at Figure 5.31 and the normalized drift force, the maximum value for the case of connected floaters is 10.75 and

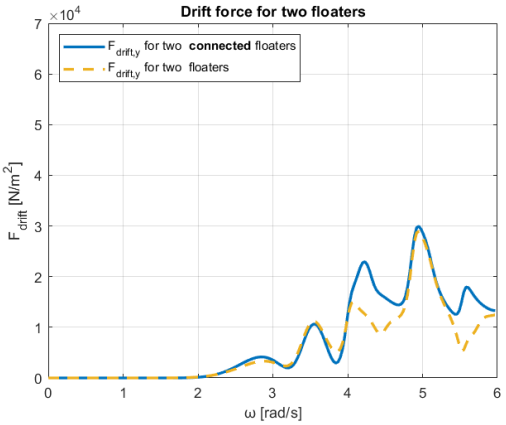

Figure 5.28: Drift force on two floaters

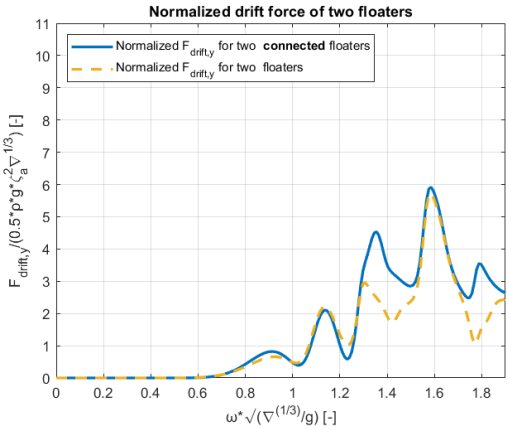

Figure 5.29: Normalized drift force on two floaters

for the case of not-connected floaters 10.34. This indicates that when the floaters are moving independently from each other, their interaction leads to slightly lower second order forces.

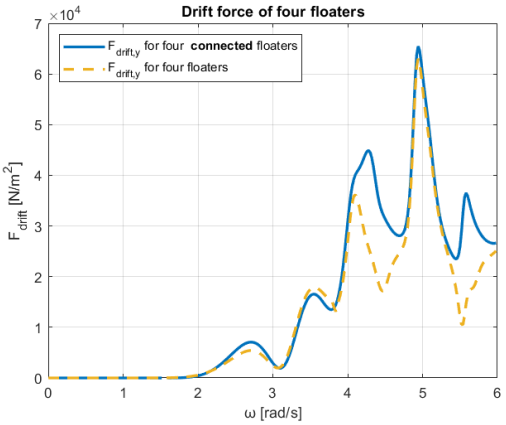

Figure 5.30: Drift force on four floaters

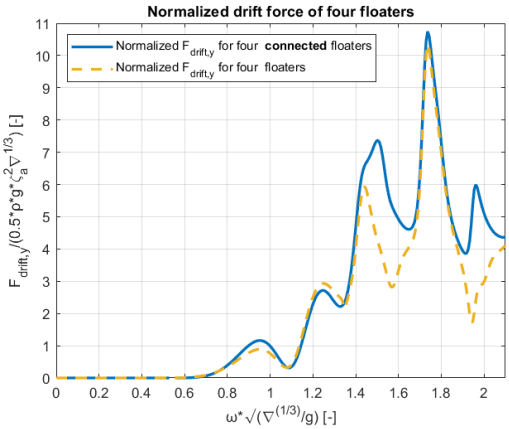

Figure 5.31: Normalized drift force on four floaters

5.5.4 Comparison of Drift Forces

After the analysis and presentation of all individual cases, it is valuable to show a picture with the overview of the drift forces. For this purpose, all the cases with the floaters have been included, as well as a reference case of a barge to use for comparison. This barge is the barge used in Section 4.4.2 for the validation of drift forces but now it has been analyzed under the effect of beam waves, as this is the same condition for the floaters. Table 5.2 is giving a comparison of the dimensions for the two floating bodies.

Parameter	Floater	Barge
Length (m)	2.1	150
Width (m)	0.588	50
Draft (m)	0.36	10
Displacement (m^3)	0.445	73,750

Table 5.2: Comparison of the dimensions of the floater and the barge

As it is obvious from Table 5.2, the submerged part of the barge is 1.7×10^5 times larger than the one of the floater. Figures 5.30 and 5.33 illustrate the results in terms of drift and normalized drift forces.

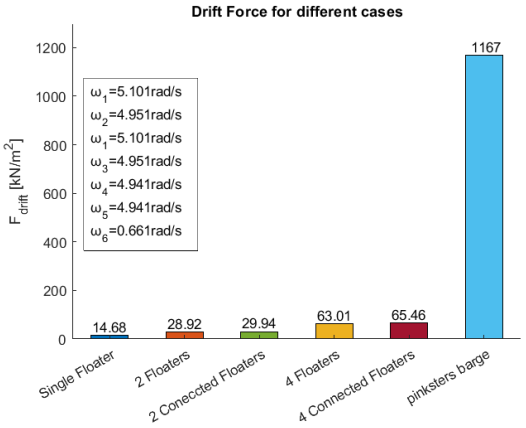

Figure 5.32: Summary of drift forces for various geometries

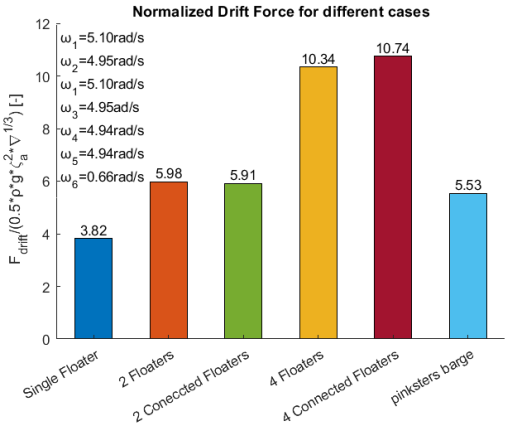

Figure 5.33: Summary of normalized drift for various geometries

Isolating the values of Figure 5.32 for the single floater and the barge it is recorded that: the maximum drift force for the floater is 14.68kN per wave amplitude squared while for the barge it goes up to 1167kN/m^2, being 80 times larger. Now, regarding the peak frequency, for the floater it is at 5.1rad/s while for the barge 0.66. This means that for the wider structure (barge), the maximum drift force occurs for a longer wave. It makes sense therefore to check the ratio of the wavelength for which the maximum occurs over the width of the structure. This ratio is 4.0 for the floater and 2.8 for the barge. Even though these numbers present a certain deviation, they can give an approximate indicator for the wavelength and therefore the wave frequency at which the maximum horizontal force may occur. Additionally, for the 3 different cases of the floaters it is observed that the addition of floaters is generating an increase in the drift force but not in an linear manner. This is accredited to the complex interaction between the floating bodies

Figure 5.33 presents special interest regarding the normalized drift forces. It is reminded here that the normalization has been achieved using the $\nabla^{1/3}$ to get a non dimensional value. For the cases of the floaters, the addition of one extra floater leads to an increase by 55% on the maximum normalize drift force. The addition of an extra row of two floaters leads to a 82% increase. The most interesting fact however lies in the comparison of the normalized drift force on the floater and the barge. As explained earlier, every extra floater leads to a significant increase in the force. That means that more displaced volume leads to higher forces. However, for the case of the barge that has 1.7×10^5 larger volume, the normalized drift force is just 45% larger from the single floater. The draft of the barge is 10m while the draft of the floater is just 0.36m. This consequently means, that adding bodies or increasing the displacement close to water surface leads to a direct increase the drift force. However, an increased displacement that goes way deeper from the waterline has just a minor effect. This behavior is totally explained by the fact that most of the wave energy is concentrated close to the waterline.

5.6 Expansion of Forces to Solar Unit

Until now, the analysis of the second order forces has been focused on four floaters that consist the solar boat of GroenLeven. Together with the analytical calculations for the wind forces the following results have occurred (Table 5.3) that regard the two forces acting on a solar boat. As the drift force is expressed in Newtons per wave amplitude squared, it is required to make an estimate of the wave amplitude. This is done using the maximum wave steepness ratio, that regulates that the wave height cannot exceed the 1/7 of the wave length in deep water conditions [39]. With an estimated wave height, the maximum drift forces, expressed in Newtons, on a solar boat can be computed. The total force acting on a solar boat is the summation of the wave drift forces and the wind forces acting on the solar panels and the freeboard of the floaters. Now, a comparison with the forces already acting on the wind turbine and the corresponding overturning moments is possible. An overview of these forces is illustrated in Figure 3.8. It is important to note that the maximum wind forces on the wind turbine have been calculated for a wind speed of 2.5 x average wind speed as described in Section 3.2.4.

The next step is to expand these forces to a whole solar unit consisting of 20 rows and 20 columns of solar boats, leading to a total of 400 solar boats. The most conservative approach is adopted in this project, as the solar unit wave forces are computed after the simple multiplication of the number of panels with the wave forces acting on a solar boat. Regarding the wind forces, it is assumed that only a percentage of the force is acting on

the rows behind the first row of panels due to the sheltering effects. The sheltering coefficients can be found in Appendix B, in Table B.3 for the wind force acting on the panels and in Table B.4 for the wind force acting on the floaters. Therefore, the total wind force on a solar unit can be described by the following equations. It is reminded here that every solar boat has two rows of floaters.

$$F_{tot,wind,panels} = (F_{wind,panels} + F_{wind,panels} * C_{shelt,2ndrowpanels} + F_{wind,panels} * C_{shelt,3rdrowpanels} + F_{wind,panels} * C_{shelt,3>3rowpanels} * (N_{columns} - 3)) * N_{rows,panels}$$

$$F_{tot,wind,floaters} = (F_{wind,floaters} + F_{windfloaters} * C_{shelt,2ndrowfloaters} + F_{wind,floaters} * C_{shelt,3rdrowfloaters} + F_{wind,floaters} * C_{shelt,3>3rowfloaters} * (N_{columns}) * 2 - 3) * N_{rows,floaters}$$

The total forces of the solar boat have been computed for the maximum drift forces which is again rather a conservative approach. Additionally, the wave drift forces and the wind forces acting on the solar units have resulted for a wind speed of 30m/s (50 year return period) and a wave state with a significant wave height of 1.70m and significant period of 4.34s. Therefore, it is again a conservative approach since the maximum mooring force occurs for differnt wind speeds compared to the maximum turbine forces.
According to Figure 3.3, every solar unit can be moored to 5 wind turbines along the x-axis which yields the most extreme results. In the other direction, more wind turbines can contribute and share the mooring force. As a result, the total forces acting on a solar unit can be divided by 5 to yield the final total mooring force acting on a wind turbine with an arm of 12.5m with respect to the base of the foundation.

As was analytically explained in Section 4.4.2, during the validation of the horizontal drift force on a barge, there were two types of mismatches: a mismatch in the maximum amplitude of the force and a mismatch in the frequency of the maximum occurs. The first mismatch has a direct impact on the total forces of the floating solar unit while the latter has an indirect impact through the calculated wave amplitude. Therefore, these two parameters are used as basis for Case 2 and Case 3 that will follow. Case 1 includes the comparison of the forces using direct results obtained in Section 5.5.3 for the maximum force and the frequency where this value occurs. Case 2 is using the assumption for the influence of the maximum amplitude as resulted from Figure 4.22. Case 3 is using the same results to make assumption for the peak frequency. Case 4 is introduced to calculate and compare the total forces of a solar unit, after taking into account the sheltering effects that the downwave boats are experiencing. Finally, a fifth case is presented where the total drift force is calculated based on the drift force density spectrum instead of the maximum value. This is performed to take into consideration the local environmental data. The presentation of every single case follows. For the comparison of the forces and moments, the ratio of the mooring forces over the other forces acting on the wind turbine is going to be used. A threshold of 15%-20% is arbitrarily used to serve as a reference point for the various plots.

Parameter	Value	Unit
Maximum Drift Force	65.46	kN/m^2
Peak Frequency	4.94	rad/s
Peak Wave Amplitude	0.18	m
Wind Load Panel	653	N
Wind Load Floater	164	N

Table 5.3: Summary of forces of a solar boat

5.6.1 Case 1: Maximum Forces

As was explained previously, the first case regards the calculation of the ratio of the forces and the moments for the maximum value of the drift forces as computed for four connected floaters. Figures 5.34-5.37 illustrate the computed results. The first two plots are expressed in terms of total number of solar boats per floating solar unit, while the bottom row of figures is expressing the results in terms of installed capacity. All figures include these five components: the existing force/moments on the wind turbine, the forces/moments of the mooring force for various number of boats (with 400 boats corresponding to the base case design and indicated with the star marker), the ratio of mooring force/moments over the existing forces/moments, a green stripe representing the threshold of 15-20% of this ratio and finally a pink stripe highlighting the base case scenario. For Case 1 and the base case scenario, the mooring forces reach up to 180kN and the corresponding moments up to 2.2MNm. From these forces, only 5% belongs to wind forces acting on the solar boats. Finally, the ratios of mooring over the existing forces and moments are 1.64 and 0.60 respectively. It can be said that Case 1 leads to high loading but even though the ratio of the forces is high, the moment ratio is considerable lower. This fact has its explanation at the arm at which the forces are acting. The majority of the wind forces are acting close to the hub height of the wind turbine at about 47.5m from the ground, while the mooring forces have an arm of 12.5m and this is the worst case scenario since it corresponds to the maximum water level.

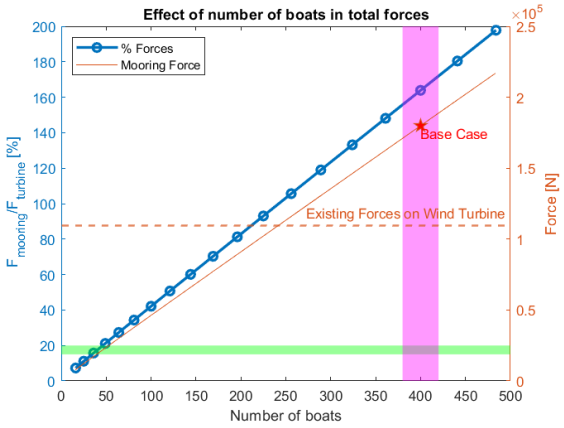

Figure 5.34: Case-1: Ratio of forces as a function of total solar boats per solar unit

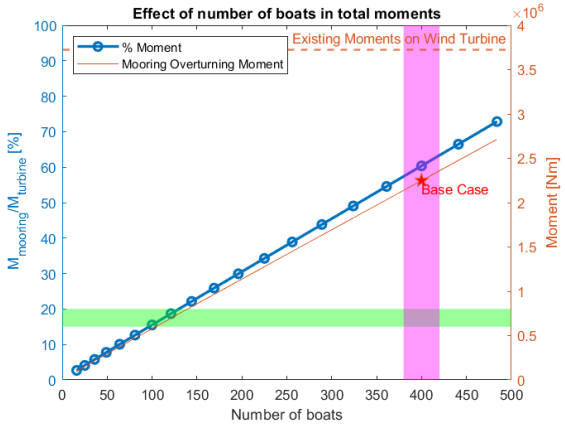

Figure 5.35: Case-1: Ratio of moments as a function of total solar boats per solar unit

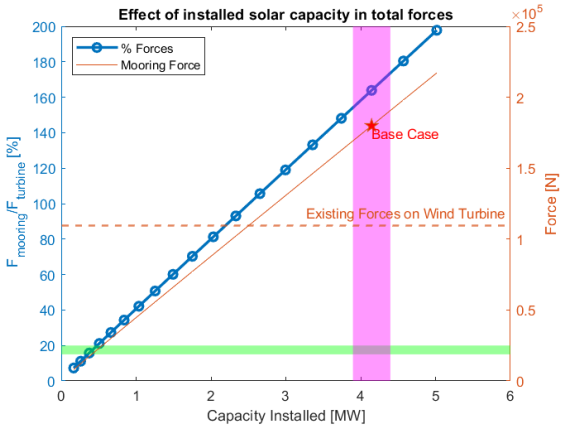

Figure 5.36: Case-1: Ratio of forces as a function of installed capacity per solar unit

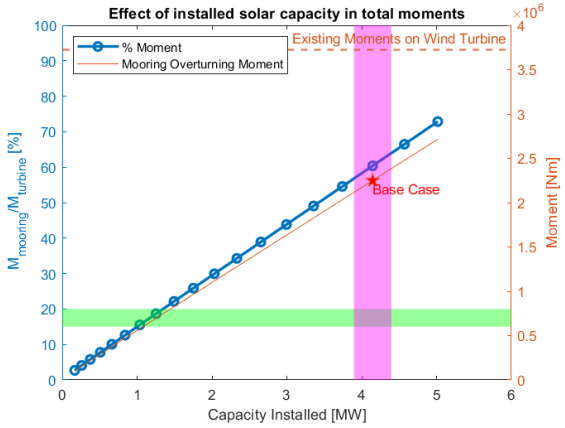

Figure 5.37: Case-1: Ratio of moments as a function of installed capacity per solar unit

5.6.2 Case 2: Assumption for Maximum Amplitude

The second case regards the adaptation of the maximum drift force on four floaters. According to Section 4.4.2 and specifically Figure 4.22, there is a deviation of 53% between the value computed with NEMOH and the reference data. This value is used to recalculate the forces on a solar boat and then a simple multiplication gives the expanded forces all over the floating solar unit. Figures 5.38-5.41 present the calculated results for the ratios of forces and moments. The mooring force has now dropped to 120kN while the mooring overturning moment has now declined to 1.5MNm. For Case 2, the wind forces on the panels and floaters account for only 8% of the total mooring force. So, once again the governing influence is coming from the wave excitation. Finally, for a solar unit of 4.1MW the ratio of the mooring forces over the existing wind turbine forces has reached a value of 1.1, noting therefore a 33% lower value compared to Case 1. The ratio of moments has now become 0.4 corresponding also to a 33% lower value. In conclusion, even if the assumption for the maximum drift force is made, the mooring forces are still way too high to consider the proposed mooring system feasible.

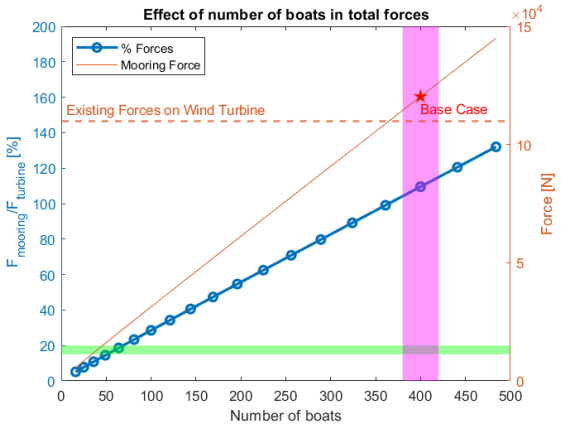

Figure 5.38: Case-2: Ratio of forces as a function of total solar boats per solar unit

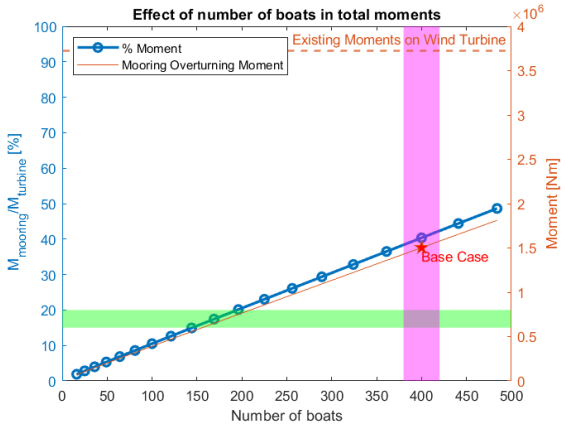

Figure 5.39: Case-2: Ratio of moments as a function of total solar boats per solar unit

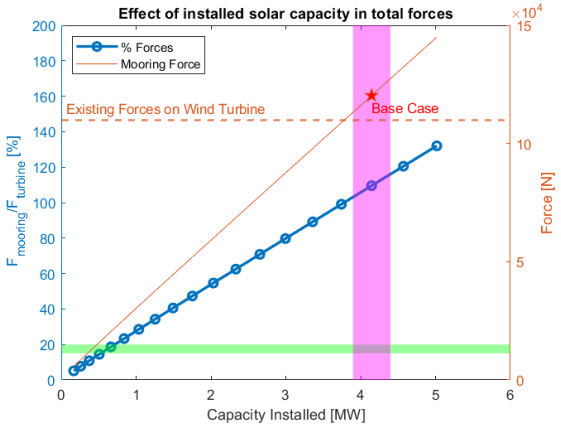

Figure 5.40: Case-2: Ratio of forces as a function of installed capacity per solar unit

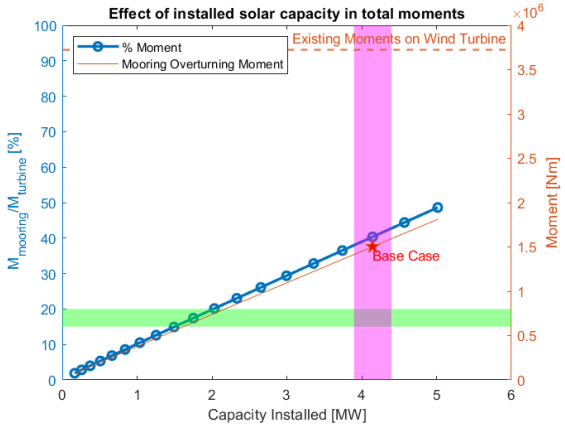

Figure 5.41: Case-2: Ratio of moments as a function of installed capacity per solar unit

5.6.3 Case 3: Assumption for Peak Frequency

The third case has been selected in order to account for the mismatch of the frequencies where the maximum drift force occurs. According to Figure 4.22, the reference data presents a peak at a normalized frequency of 1.91 while for the results computed by the developed model this value is 0.59. Converting these values using the normalization factors of displacement and gravity acceleration, they correspond to 0.9 and 0.28rad/s. Therefore, a mismatch of 60% has occurred for the peak frequencies. If this mismatch is traced back to the computation of the maximum wave height using the steepness ratio, the following results as illustrated in Figures 5.42-5.45 occur. With the adopted assumption of peak frequencies, the mooring force is now equal to 38kN and the corresponding mooring moment has dropped to a value of 0.48MNm. When compared to the values of Case 1, they account only for 21% of the forces and moments respectively. The ratio of mooring forces has now decreased to 35% and the ratio of mooring moments has dropped down to only 13%. If a comparison is made between the drift forces and the wind forces of the solar boat, the wind forces account now for 25% of the total load. The assumption adopted for this case has significantly reduced the loading coming from the potential mooring line, with the forces still being above the threshold but with the moments laying significantly lower. It can be said that influence of this assumption is so large, because it is actually influencing the wave height which is then squared before multiplied with the drift forces. This square factor is causing this noticeable drop in mooring forces.

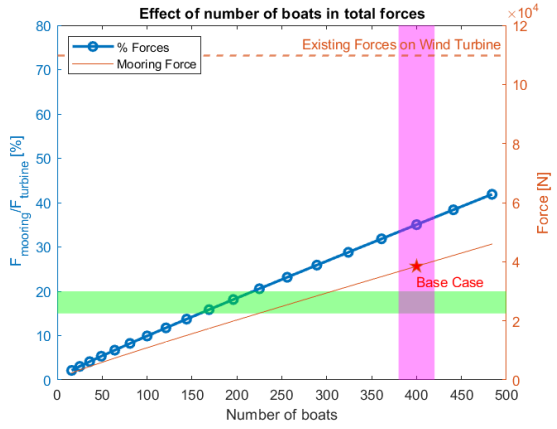

Figure 5.42: Case-3: Ratio of forces as a function of total solar boats per solar unit

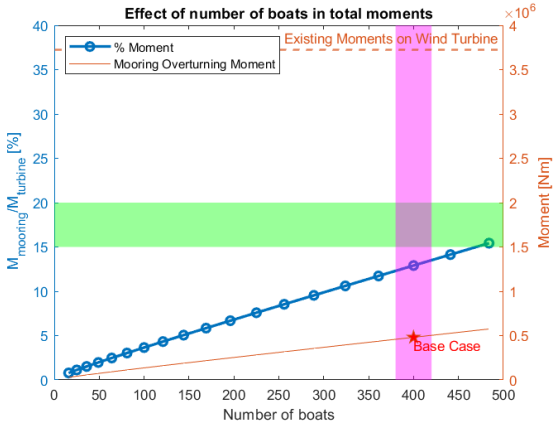

Figure 5.43: Case-3: Ratio of moments as a function of total solar boats per solar unit

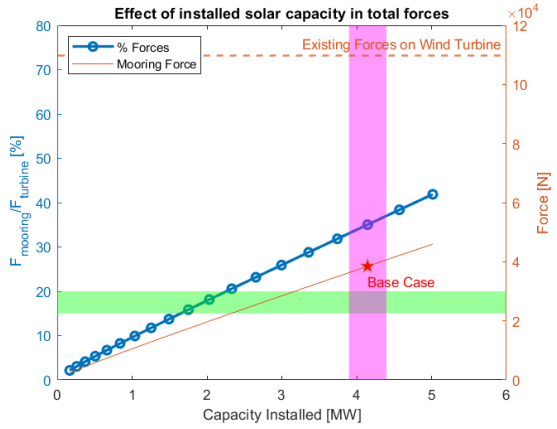

Figure 5.44: Case-3: Ratio of forces as a function of installed capacity per solar unit

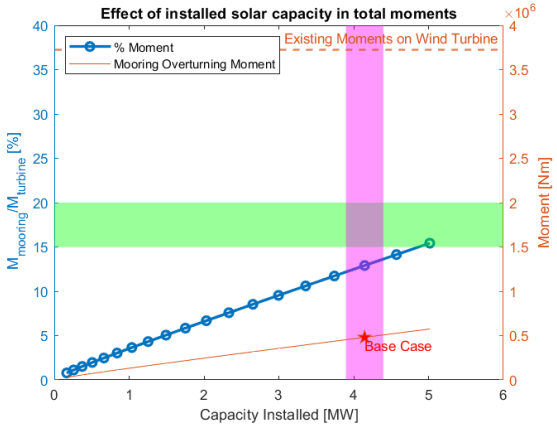

Figure 5.45: Case-3: Ratio of moments as a function of installed capacity per solar unit

5.6.4 Case 4: Assumption for Sheltering Effects

As it has been stated multiple times in this report, the expansion of the forces to the solar unit is rather conservative because they are just scaled with the number of solar boats. The fourth case has been selected to investigate what is the influence of the sheltering factor in the total mooring forces. It has been selected here to use the factors as follows: the first row of floaters is experiencing the full drift force, the second row is experiencing only 70% of the initial value, the third row is subjected to 60% of the starting drift force and every row behind the third row is experiencing only 50% of the starting value. If these coefficients are compared with the coefficients used in Section 2.5 for the analytical wind loads, they are significantly larger and thus provide once again conservative results.
Figures 5.46-5.49 illustrate the results for the ratio of forces and moments for Case number 4. Starting from the forces and Figure 5.47, the base case design of 400 solar boats leads to 102kN being 57% of Case 1. The ratio of the forces has now dropped to 92% deviating again by a large margin from the threshold of 20%. Moving to Figure 5.47, it is observed that now the mooring moments are 1.3MNm corresponding to 59% of the starting scenario of maximum drift moments. The consequent ratio of moments has now turned to 35% of the existing moments of the wind turbine. Finally for Case 4, the wind loads contribute only 9.3% to the total mooring force. In conclusion, Case 4 presents decreased values but the forces are still too large for the implementation of the system.

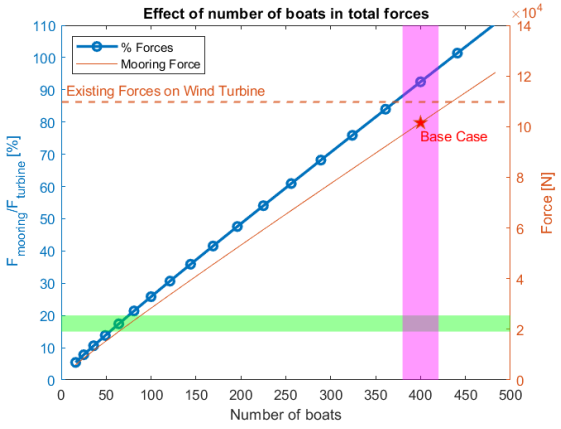

Figure 5.46: Case-4: Ratio of forces as a function of total solar boats per solar unit

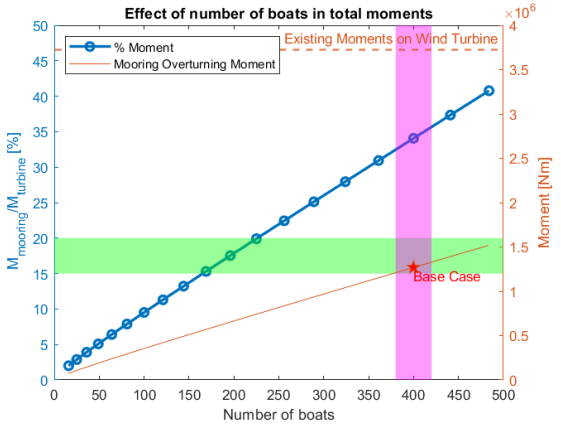

Figure 5.47: Case-4: Ratio of moments as a function of total solar boats per solar unit

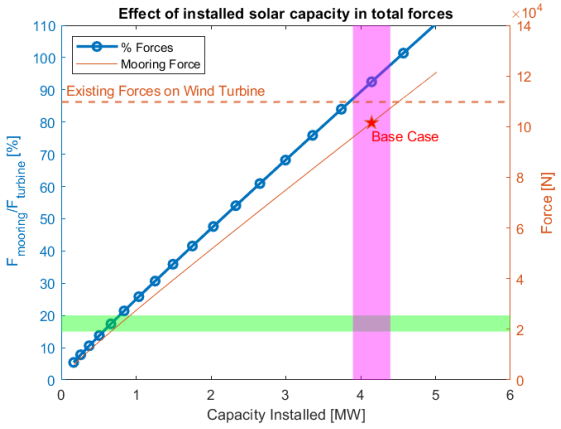

Figure 5.48: Case-4: Ratio of forces as a function of installed capacity per solar unit

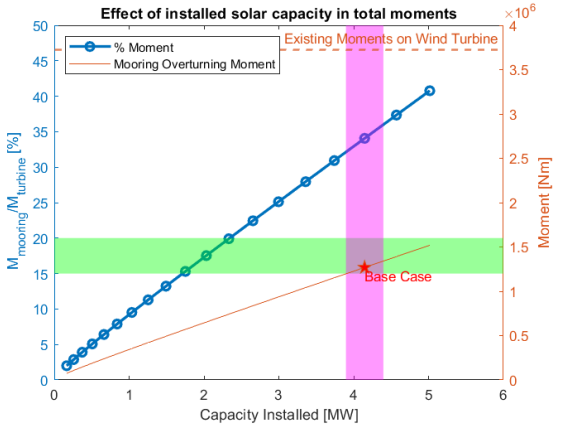

Figure 5.49: Case-4: Ratio of moments as a function of installed capacity per solar unit

5.6.5 Case 5: Drift Force Density Spectrum

The final case is introducing a new method to calculate the total mooring forces. For this purpose, the drift force density spectrum is used. The exact description of the method can be found in Section 3.3.7 but a quick explanation is following here. The wave energy density spectrum can be converted to a density spectrum of the ratio $\zeta_\alpha^2/\Delta\omega$ with the appropriate transformations (Figure 3.14). As can be seen from Figure 5.30, the drift force is expressed in Newtons per wave amplitude squared. The multiplication of these two aforementioned plots can yield the drift force distribution expressed in Newtons per amplitude bin $\Delta\omega$ as illustrated in Figure 5.50. With the use of Equation 3.15, the discrete force values of this plot can give the total drift force. This method has the advantage of incorporating the influence of the local environmental conditions. More analytically, wave drift forces are mostly excited after a frequency of 2rad/s while the majority of the wave energy is dropping rapidly after 2.5rad/s. As shown in Figure 5.50, the resulting significant drift force for a single solar boat is equal to 2502.25N compared to a value of 2130N as computed in Case 1 for the maximum drift force.

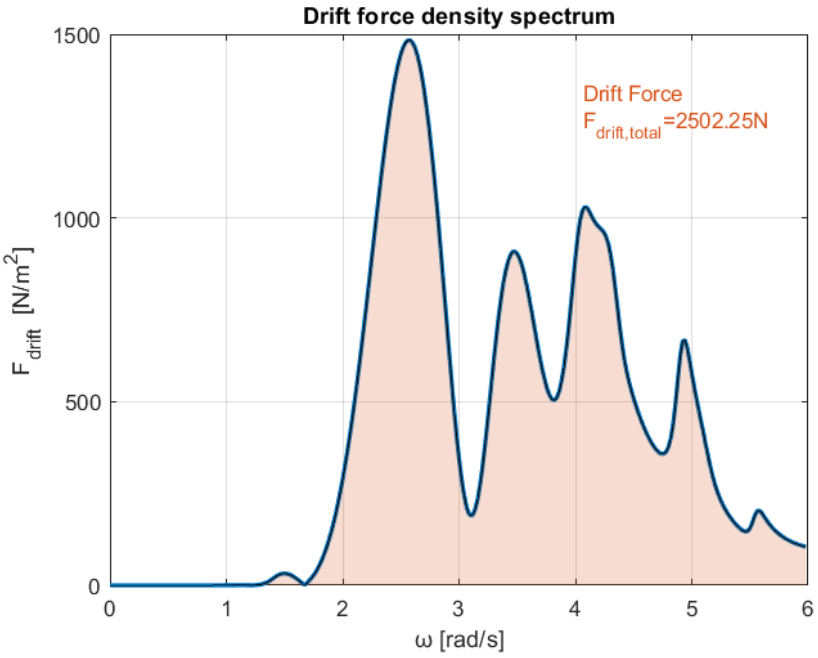

Figure 5.50: Drift force spectrum

After the calculation of significant drift force, Figures 5.51-5.54 illustrate the obtained results for the mooring forces and moments. Starting from the ratio of forces, the value has climbed to a value of 191% with a mooring force equal to 210kN. Moving towards the moment ratio, the value has reached up to 70% with the overturning mooring force being 13kNm. Both the force and moment ratios are located now above the selected threshold. These values indicate the huge impact of the inclusion of the wave energy into the method, in comparison to the cases that were resolved for the maximum forces. For this scenario, the wind loads on the solar boat are accounting for a small part of the total forces, with the exact value of 4.5%. For Case 3, the wind loads were responsible for 25% of the forces. It is becoming therefore obvious, that as the impact of the drift force is weakened, the wind loads on the solar panels and the freeboard of floaters are taking over the behavior of the solar units.

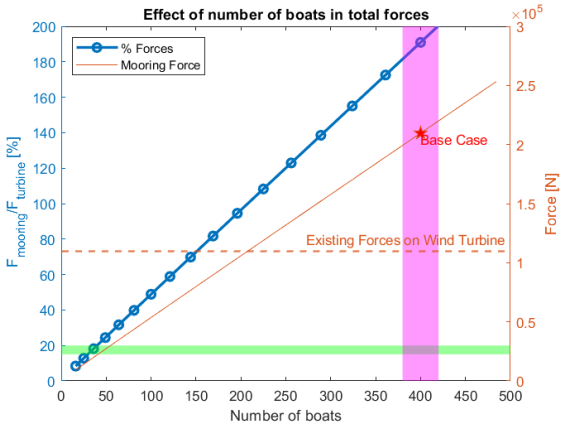

Figure 5.51: Case-5: Ratio of forces as a function of total solar boats per solar unit

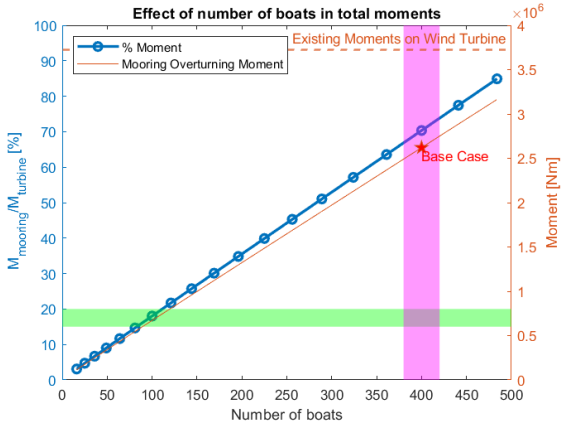

Figure 5.52: Case-5: Ratio of moments as a function of total solar boats per solar unit

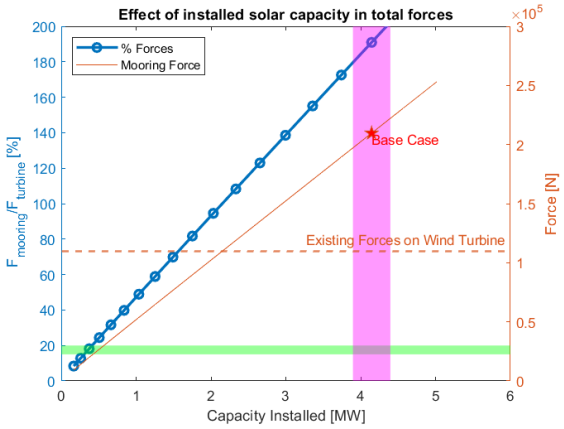

Figure 5.53: Case-5: Ratio of forces as a function of installed capacity per solar unit

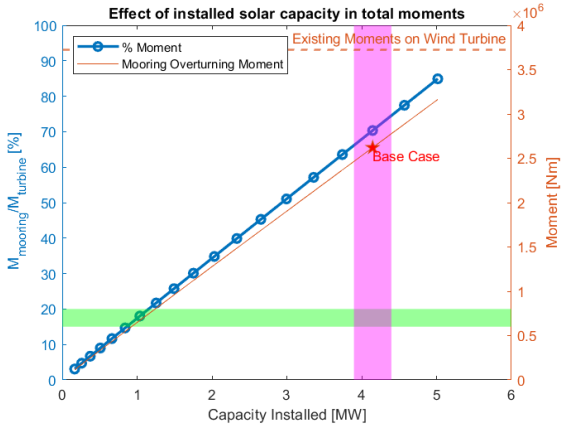

Figure 5.54: Case-5: Ratio of moments as a function of installed capacity per solar unit

To summarize all the cases examined here, Table 5.4 is presented a summary of the forces and moments as calculated for every individual case.

Case	Assumption	Force [kN]	Moments [kNm]	$F_{moor}/F_{existing}$ [-]	$M_{moor}/M_{existing}$ [-]
1	Maximum Drift Force	180	2200	1.64	0.60
2	Reduced Amplitude	120	1500	1.10	0.40
3	Reduced Peak Frequency	38	480	0.35	0.13
4	Sheltering Effects	102	1300	0.92	0.35
5	Drift Force Density Spectrum	210	2620	1.91	0.70

Table 5.4: Summary of all the cases for the comparison of the forces

According to Table 5.4, Case 5 presents the highest ratios, with Case 3 being the most favorable for the system.

6 | Discussion

This chapter makes an evaluation of the results presented in Chapter 5. Moreover, another published study is used for a comparison of the results.

6.1 First Order Wave Forces

rDuring this project, different geometries and configurations have been analyzed. Regarding first order wave forces, the addition of an extra floating body close to another leads to a significant increase in the forces of the bodies along the y-axis as well as the corresponding moments around x-axis, since these DoFs are coupled. As far as the vertical force is concerned, the interaction of the two bodies does not influence significantly the individual forces on the bodies. New peaks and troughs in various frequencies are occurring in the plots of sway forces and roll moments. These frequencies could be linked with the existence of standing waves between the gap of the bodies. An almost constant ratio of wave length to structure width was found to connect two consecutive frequencies where the peaks and troughs occur. The prevailing tendency in the three degrees of freedom analyzed here, is that the upwave floater is acting as a wave attenuator and therefore the downwave floater is presenting smaller responses. However, when the floaters are connected through a rigid connection, the motions in sway and roll become the same for the upwave and downwave floater. The average value of these responses is also decreased by about 40% compared to the case of not connected floaters. Moreover, when the two floaters are connected, a certain number of frequencies appear where the interaction of the motions leads to complete cancellation of the sway and roll responses. For the response along the vertical axis, there is no major impact of the rigid connection.

Expanding the model to four connected floaters, the exciting wave forces do not present any important deviation. The behavior is similar to the case of the two connected floaters and this is probably related to the fact that the distance perpendicular to the incoming wave, as regulated by the solar boat, is so big that the presence of one more column of floaters does not have a major impact. The responses of the rigidly connected floaters are almost identical for the case of sway and heave motion. For the rotation around x-axis, the configuration with four floaters shows a significant increase. The average value of roll per wave amplitude is increased by 35%. This means that a total increase in size for the rigid body is mostly influencing the rotational motions.

6.2 Second Order Drift Forces

All information obtained for the wave drift force should be treated with caution, since the model was not able to be completely validated with reference data. Despite this, the order of magnitude has shown to be correct and therefore can serve as a good indicator of the mean horizontal force. The addition of extra floaters leads to a direct increase in the drift force. However, this increase is not completely linear. In any case, it indicates that the small draft of the floaters used make them receive the whole energy of the waves and the upwave row of floaters does not reflect a high percentage of it.
Based on the different scenarios adopted for the calculation of the total drift force on a solar unit it has occurred that if the maximum value of the drift force is used, then the incident wave height is the most influential parameter. The method with the use of the drift force distribution presents the advantage of suitably involving the local environmental data in the prediction of the total drift forces. Finally, it is also the scenario that yields the highest forces and therefore the most conservative results for the proposed mooring configuration, as the ratio of mooring forces over the forces acting on the tower reaches up to 190%.

The total mooring forces and the corresponding force and moments ratios are calculated for the base case design with solar units consisting of 400 solar boats and reaching up to 4.1MW. The size of the solar unit affects linearly the amplitude of the forces. This consequently means that if less solar boats per solar unit are used, these ratios would reduce accordingly.

6.3 Considerations on the mooring system

In a study performed by Ikhennicheu et al. [43], analytical formulas were used for the calculation of total loads on a solar farm within a lake. The components of the forces correspond to wind and wave loads. For the calculation of the wind loads similar formulas have been adopted for this report. As for the wave loads, Maruo's formula [68] was used with the assumption of 80% reflected waves. The floating solar unit has been analyzed as a large rigid body rather than individual floaters and it was located in a large lake with 3km available fetch. These environmental conditions present remarkable similarity with the case of Delta21. The analysis was performed for four different wind directions since the orientation of the panels resulted into different loading. For a floating island of 7.5MW the wind loads were responsible for 66% to 82% of total loading on the island. That means that the wave loads on the floaters ranged from 18% to 34% of the total loading. When compared to this report, the value of wind loads for the scenario with the significant value of drift force accounts for only 4.5% of the total loading. The rest of the scenarios lead to a range from 5% to 25%. This means that the selection of the approach for the calculation of the wave forces is very influential as for the results obtained. The consideration of the solar unit as a rigid body leads to significantly lower wave loads but does not take into account the interaction of individual floaters, as well as the interaction of individual solar boats.

Moreover, the report by Ikhennicheu et al. included some preliminary calculations for the mooring design. The main observation was that since the fairleads of the mooring lines will be on the floaters, the acceptable load on the floater is going to be the crucial factor in the determination of the total amount of lines. In their report, for a total load of 1200kN on the floating unit, 83 mooring lines are used. The selected lines consist of a combination of studless chains for the part of the line laying on the seabed and steel wire for the rest. In this project, for the worst case scenario, the total force does not exceed the value of 210kN which means that a considerable lower number of lines could be used. The usage of wire rope (spiral strand) for the mooring lines would lead to high axial stiffness followed by a low submerged weight, allowing the lines to maintain a horizontal configuration.

The final selection of the mooring system has to take into account the optimization between the environmental loading and the number of the fairleads. The maximum load at the fairlead is usually given by the manufacturer. Therefore, the details for the mooring design should be further checked in a more thorough analysis after the final decision on the size and total number of solar boats and thus the total solar unit loading.

7 | Conclusions

In this thesis a new synergy between a wind and solar park has been proposed for the Energy Storage Lake of Delta21. The local environmental conditions within the lake are imposing great challenges due to large water level fluctuations. One of these challenges is a mooring configuration for the floating solar units capable to follow the water level fluctuations. The proposed configuration developed in this project is investigating the potential of using the towers of the wind turbines as anchoring points for the mooring lines. The first step towards the feasibility of such a mooring system is the estimation of the forces that would be applied on the wind turbine tower through the mooring line. This thesis proposed a methodology for the estimation of these forces, after the selection of a base case design for the arrangement of the solar units and the wind turbines based on the LCOE and the annual energy production.

The structure that is studied in this project is the floating solar boat that GroenLeven is using. The solar boat is consisted of 4 floaters that are in contact with the water and 16 solar panels with an inclination of about 12°. The analysis is therefore distinguished into two parts: estimation of the wind loads as imposed on the solar panels and the freeboard of the floaters; wave forces acting on the submerged part of the floaters. In order to create solid steps during the solution of the problem, four different building blocks have been chosen. These building blocks have been selected to represent: a single floater, two adjacent floaters, two adjacent floaters mechanically connected and finally four adjacent floaters mechanically connected representing in that way the solar boat. Each building block has been analyzed separately in order to create a correct basis for the expansion of the full model.

Linear potential theory has been used successfully through the boundary element method NEMOH to perform the hydrodynamic simulations. The output of NEMOH in terms of hydrodynamic coefficients and wave exciting forces was then used to solve the equation of motions and finally calculate the responses of the floating bodies corresponding to each block. After the calculation of these first order wave forces and the resulting responses, the far-field approach was adopted for the estimation of the QTFs of the wave drift force. The focus has been drawn on these mean drift forces since they are the component of the wave forces that a mooring system would primarily counteract. The end goal was therefore the estimation of the drift forces for a solar boat. For the calculation of the wind loads use of analytical formulas has been made. During the analysis, the only wave direction considered was perpendicular to the length of the floaters yielding in this way higher forces and motions and making the approach more conservative.

In order to check the accuracy of the intermediate results, four validation cases with reference published data were used. More specifically, the validation cases have been applied for: the first order wave forces and motions of a single barge, the first order wave forces and motions of two adjacent barges placed in close proximity, the first order wave forces and motions of two adjacent barges mechanically connected with a hinged connection and then with a rigid connection, the second order drift forces on a floating sphere and a floating barge. The computed first order forces and motions with the use of NEMOH presented a great agreement with the reference data for both the case of a single as well as two adjacent barges. The mechanical connection with the use of springs as adopted in the model was also proved to generate reliable results. Regarding the mean drift forces, the use of the far-field approach proved to give accurate results for the case of a floating sphere whereas a noticeable deviation was recorded for the floating barge. Even though the calculated drift force for the case of the barge was not entirely matched with the reference data, it still gives a good estimation of the order of magnitude of these forces. For this reason, the far-field approach has been considered sufficient for this early stage of the design, but any further study should prerequisite its correct implementation.

After the calculation of the mean wave drift and wind forces on a single solar boat, the expansion towards a whole solar unit consisting of 400 solar boats and reaching a capacity of 4.1MW was performed. The total

forces of the solar unit were assumed to scale linearly with the number of the boats. This approach is considered to produce again the most conservative results. Five different scenarios were examined to investigate the influence of the following parameters: the maximum value of the drift force, the wave amplitude, the sheltering effects of adjacent boats and the drift force density spectrum. The results of these five scenarios were then compared with the wind and wave forces acting on the wind turbine independently of the inclusion of the mooring line. The results showed that the adoption of the total force based on the drift force density spectrum leads firstly to a correct consideration of the local environmental conditions and secondly to total mooring forces accounting for 210% of the tower forces. For this case, the wind loads were responsible for only 4.5% of the total loading acting on the solar unit. As for the scenarios using the maximum value of the drift force, the wave amplitude was proven to be the single most influential parameter. For the first four scenarios the mooring forces ranged from 35% to 165% of the overall wind turbine tower loading. The concluding remark is that the mooring forces that would result from the proposed usage of the wind turbine towers as anchoring points, do not comprise a showstopper for the design. The proper approach to scale the forces of a single solar boat to the whole solar unit should be selected with caution. However, there are more aspects that have to be investigated and checked before obtaining a concrete answer for the feasibility of the system. These aspects include among others the technical design of such a connection, the exact mooring line material and configuration, the stress analysis on the connection point on the tower and of course the impact of such a solution in the economic side of the project.

This thesis has focused exclusively on introducing a new synergy for a hybrid power plant consisting of bottom founded wind turbines and floating solar units within the ESL of Delta21. There are definitely more aspects and elements relevant to such a HPP that require a lot of consideration. These elements have to do with the optimization of the configuration for each energy resource; the synergies and challenges for sharing electrical infrastructure such as transformers and power cables; the impact of shadowing effects due to the presence of the wind turbines on the solar energy production; the dynamic behavior of the tower of the wind turbines due to the water fluctuations inside the lake. In any case, the purpose of this thesis was to become a springboard for studying the cooperation of these two renewable technologies within the ESL. The results look favorable towards further investigation of the project and can be used as input for future studies regarding the loading of the wind turbine towers.

8 | Recommendations

In this chapter recommendations for future research are presented, that could potentially improve the work performed in this thesis and also expand the feasibility study for a combined wind and solar park within the ESL of Delta21. The order that these recommendations are displayed, reflect their relative importance.

As mentioned in both the validation and the conclusions of this report, the calculated wave drift force on a barge with the use of the far-field approach was not able to entirely match the reference data. Even though it provides a good estimation of the order of magnitude, it consequently means that there is uncertainty regarding the exact values of the drift forces of a solar boat. Therefore, it is a component that definitely needs improvement for further use of the model. The improvement could potentially be achieved with the correct implementation of the far-field approach which was not able to be validated in this project. Another way to improve the reliability of the calculated drift forces would be the adoption of the near-field approach. Even though it presents higher complexity, the direct pressure integration might lead to more accurate results and can also be used for a comparison with the far-field approach.

During this thesis, the hydrodynamic simulations with the software NEMOH were limited to four floating bodies representing a solar boat. The expansion to a grid of multiple solar boats and the conclusions for the behavior of the whole solar unit were therefore drawn using some assumptions. In order to remove the uncertainty underlying these assumptions, it would be very interesting and important to include more floating bodies in the simulations. The expansion of the model from a single solar boat to a 2x2 grid of 4 solar boats would produce results that could capture the complex interaction of these floating bodies. This would also require the correct modelling of the connection between the solar boats which is close to a hinge connection that allows relevant rotations. Additionally, more conclusions could be made about the sheltering effects for a row of 4 floaters as well as the expansion of the first and second order forces to the whole unit. However, the modelling of more than one solar boats would come with a tremendous increase in computational time. That means that the computational power would be a limiting factor for this improvement of the model.

During the final stage of the project, the computed mooring forces are being compared with wind and wave forces acting on the towers. In addition, the contribution of these forces into the overturning moments is being checked. The next step and improvement of the method would include the investigation of the influence of these forces on the stresses. Once the material of the tower has been defined, it would be possible to estimate the potential impact of the mooring force on the thickness and radius of the tower based on the shear and bending moment capacity. This additional check would allow for a more concrete evaluation on the feasibility of the system.

The model developed in this project is aiming to the estimation of the second order drift forces and the wind forces which can then be later used as input for the design of a mooring system. This implies an uncoupled analysis for the modeling of the mooring system. In reality however, the inclusion of the mooring in the system would produce different results through its stiffness and inertia. Therefore, during a later stage of the design, the properties and configuration of the mooring system would be necessary to correctly capture the interaction with the floating unit.

For the selection of the mooring configuration, it would also be necessary to set the final distances between the solar units and the wind turbines. This would mean that an optimization of the layout should be sought with the potential objectives being the maximization of the energy output, the minimization of the levelized cost of energy, the minimization of the shadow effects or a more stable energy output. Future studies could focus on these parameters to evaluate different configurations of the layout of the HPP.

A final recommendation for future studies lies in the economic feasibility of the proposed system. Using the towers of the wind turbines as anchoring points would mean that a mechanism with a twofold character should be used. The first objective would be to allow the floating units to follow the water fluctuations as imposed by the operation of the lake while the second objective should be to protect the tower from wear and damages. This would introduce a new component in comparison with conventional mooring systems. As a result, the impact of such a system on the total costs should be further investigated to obtain a concrete overview of the feasibility of the system.

References

[1] S. R. Ara, S. Paul, and Z. H. Rather. “Two-level planning approach to analyze techno-economic feasibility of hybrid offshore wind-solar pv power plants”. In: *Sustainable Energy Technologies and Assessments* 47 (2021), p. 101509.

[2] A. Arabali, M. Ghofrani, M. Etezadi-Amoli, M. S. Fadali, and Y. Baghzouz. “Genetic-algorithm-based optimization approach for energy management”. In: *IEEE Transactions on Power Delivery* 28.1 (2012), pp. 162–170.

[3] S. Astariz, A. Vazquez, and G. Iglesias. “Evaluation and comparison of the levelized cost of tidal, wave, and offshore wind energy”. In: *Journal of Renewable and Sustainable Energy* 7.5 (2015), p. 053112.

[4] R. de Azevedo and O. Mohammed. “Profit-maximizing utility-scale hybrid wind-PV farm modeling and optimization”. In: *SoutheastCon 2015*. IEEE. 2015, pp. 1–8.

[5] R. A. Badwawi, M. Abusara, and T. Mallick. “A review of hybrid solar PV and wind energy system”. In: *Smart Science* 3.3 (2015), pp. 127–138.

[6] G. Bekele and B. Palm. “Feasibility study for a standalone solar–wind-based hybrid energy system for application in Ethiopia”. In: *Applied energy* 87.2 (2010), pp. 487–495.

[7] L. Berke and H. Lavooij. *Personal Communication*. Delta21. Dec. 2022.

[8] S. Bhattacharya. *Design of foundations for offshore wind turbines*. John Wiley & Sons, 2019.

[9] W. Bieusheuvel. *Personal Communication*. GroenLeven. Apr. 2022.

[10] J.W. van der Blonk. “Concept design for the GreenBattery on the energy storage lake of the Delta21 project”. MA thesis. the Netherlands: Delft University of Technology, 2020.

[11] T. Bos. *Personal Communication*. Dutch Wind Design. Apr. 2022.

[12] D. B. Carvalho, E. .C Guardia, and J. W. M. Lima. “Technical-economic analysis of the insertion of PV power into a wind-solar hybrid system”. In: *Solar Energy* 191 (2019), pp. 530–539.

[13] Open CASCADE. *SALOME*. `https://www.salome-platform.org/`. accessed on 13/10/2022.

[14] R. Cazzaniga, M. Cicu, M. Rosa-Clot, P. Rosa-Clot, G.M. Tina, and C. Ventura. “Floating photovoltaic plants: Performance analysis and design solutions”. In: *Renewable and Sustainable Energy Reviews* 81 (2018), pp. 1730–1741.

[15] Y. C. Chiang, P. Y. Lee, P. C. Chen, S. S. Lin, and S. S. Hsiao. “A study on low-cost gravity base foundations for offshore wind turbine in Taiwan”. In: *The Twenty-fifth International Ocean and Polar Engineering Conference*. OnePetro. 2015.

[16] European Commission. *Photovoltaic Geographical Information System*. `https://re.jrc.ec.europa.eu/pvg_tools/en/tools.html`. accessed on 21/02/2022.

[17] B. L. I. X Consultancy, I.D. M. van den Brink, and M.L. de la Vieter. “Pathways to potential cost reductions for offshore wind energy”. In: TSE3200003 (2021).

[18] X. Costoya, M. deCastro, D. Carvalho, B. Arguilé-Pérez, and M. Gómez-Gesteira. “Combining offshore wind and solar photovoltaic energy to stabilize energy supply under climate change scenarios: A case study on the western Iberian Peninsula”. In: *Renewable and Sustainable Energy Reviews* 157 (2022), p. 112037.

[19] A. Couto and A. Estanqueiro. “Exploring wind and solar PV generation complementarity to meet electricity demand”. In: *Energies* 13.16 (2020), p. 4132.

[20] K. Das, A. D. Hansen, M. Koivisto, and P. E. Sørensen. “Enhanced features of wind-based hybrid power plants”. In: *Proceedings of the 4th International Hybrid Power Systems Workshop, Crete, Greece*. Vol. 20. 2019.

[21] G. Delhommeau. “Les problèmes de diffraction-radiation et de résistance de vagues: étude théorique et résolution numérique par la méthode des singularités”. PhD thesis. Nantes, 1987.

[22] KC Divya and Jacob Østergaard. “Battery energy storage technology for power systems—An overview”. In: *Electric power systems research* 79.4 (2009), pp. 511–520.

[23] DNVGL-RP DNVGL. “C205”. In: *Environmental conditions and environmental loads, Det Norske Veritas and Germanischer Lloyd, Norway* (2010).

[24] DNVGL-RP-C205. “Environmental conditions and environmental loads”. In: (2017).

[25] Gabriel Nasser Doyle de Doile, Paulo Rotella Junior, Luiz Célio Souza Rocha, Ivan Bolis, Karel Janda, and Luiz Moreira Coelho Junior. “Hybrid wind and solar photovoltaic generation with energy storage systems: A systematic literature review and contributions to technical and economic regulations”. In: *Energies* 14.20 (2021), p. 6521.

[26] E. Dursun, B. Acarkan, and O. Kilic. “Modeling of hydrogen production with a stand-alone renewable hybrid power system”. In: *International Journal of Hydrogen Energy* 37.4 (2012), pp. 3098–3107.

[27] E. van Eeden. “A new dynamic landscape for the Haringlviet: Landscape architecture explorations for Delta21”. MA thesis. the Netherlands: Technische Universiteit Delft, 2021.

[28] O. Ekren and B. Y Ekren. “Size optimization of a PV/wind hybrid energy conversion system with battery storage using simulated annealing”. In: *Applied energy* 87.2 (2010), pp. 592–598.

[29] H. Engberts. “A techno-economic feasibility analysis of the multi-use of aquaculture and PV in the Energy Storage Lake of Delta21”. MA thesis. the Netherlands: Delft University of Technology, 2021.

[30] Annette Evans, Vladimir Strezov, and Tim J Evans. “Assessment of utility energy storage options for increased renewable energy penetration”. In: *Renewable and Sustainable Energy Reviews* 16.6 (2012), pp. 4141–4147.

[31] O. M. Faltinsen and A. E. Løken. “Slow drift oscillations of a ship in irregular waves”. In: *Applied Ocean Research* 1.1 (1979), pp. 21–31.

[32] F. Fazelpour, M. Vafaeipour, O. Rahbari, and M. A. Rosen. “Intelligent optimization to integrate a plug-in hybrid electric vehicle smart parking lot with renewable energy resources and enhance grid characteristics”. In: *Energy Conversion and Management* 77 (2014), pp. 250–261.

[33] M. Folley, A. Babarit, B. Child, D. Forehand, L. O’Boyle, K. Silverthorne, J. Spinneken, V. Stratigaki, and P. Troch. “A review of numerical modelling of wave energy converter arrays”. In: *International Conference on Offshore Mechanics and Arctic Engineering*. Vol. 44946. American Society of Mechanical Engineers. 2012, pp. 535–545.

[34] D. Friel, M. Karimirad, T. Whittaker, J. Doran, and E. Howlin. “A review of floating photovoltaic design concepts and installed variations”. In: *Proceedings of the 4th International Conference Offshore Renew Energy CORE*. 2019, pp. 1–10.

[35] A. K. Gerlach, D. Stetter, J. Schmid, Ch. Breyer, et al. “PV and wind power-complementary technologies”. In: *Proc. 26th European Photovoltaic Solar Energy Conference*. Vol. 2. 2011.

[36] G. Giorgi, R. Gomes, G. Bracco, and G. Mattiazzo. “The effect of mooring line parameters in inducing parametric resonance on the spar-buoy oscillating water column wave energy converter”. In: *Journal of Marine Science and Engineering* 8.1 (2020), p. 29.

[37] S.Z.M. Golroodbari, D.F. Vaartjes, J.B.L. Meit, A.P. Van Hoeken, M. Eberveld, H. Jonker, and W. van Sark. “Pooling the cable: A techno-economic feasibility study of integrating offshore floating photovoltaic solar technology within an offshore wind park”. In: *Solar Energy* 219 (2021), pp. 65–74.

[38] P. Guevel et al. “Le théorème de Lagally généralisé et ses applications en hydrodynamique navale”. In: (1981).

[39] L. H. Holthuijsen. *Waves in oceanic and coastal waters*. Cambridge university press, 2010.

[40] S. Huang, S. Sheng, Y. You, A. Gerthoffert, W. Wang, and Z. Wang. “Numerical study of a novel flex mooring system of the floating wave energy converter in ultra-shallow water and experimental validation”. In: *Ocean Engineering* 151 (2018), pp. 342–354.

[41] W. Huang and R. Yang. “Water depth variation influence on the mooring line design for FOWT within shallow water region”. In: *Journal of Marine Science and Engineering* 9.4 (2021), p. 409.

[42] IEA. *Renewables 2021 Data Explorer, IEA, Paris*. `https://www.iea.org/articles/renewables-2021-data-explorer`. [Online; accessed 19-March-2022]. 2022.

[43] M. Ikhennicheu, B. Danglade, R. Pascal, V. Arramounet, Q. Trébaol, and F. Gorintin. “Analytical method for loads determination on floating solar farms in three typical environments”. In: *Solar Energy* 219 (2021), pp. 34–41.

[44] Infoplaza. *wave climate*. `http://www.waveclimate.com/`. accessed on 13/10/2022.

[45] R. B. Inglis and W. G. Price. “Irregular frequencies in three dimensional source distribution techniques”. In: *International Shipbuilding Progress* 28.319 (1981), pp. 57–62.

[46] IRENA. “Future of Solar Photovoltaic: Deployment, investment, technology, grid integration and socio-economic aspects (A Global Energy Transformation Paper)”. In: (2019).

[47] IRENA. “Future of wind: Deployment, investment, technology, grid integration and socio-economic aspects (A Global Energy Transformation Paper)”. In: (2019).

[48] IRENA. “Renewable Power Costs in 2021”. In: (2022).

[49] T. Janssen. “Modelling mechanical behavior of offshore floating solar concepts”. MA thesis. the Netherlands: Delft University of Technology, 2022.

[50] P. Jenkins, M. Elmnifi, A. Younis, and A. Emhamed. “Hybrid power generation by using solar and wind energy: case study”. In: *World Journal of Mechanics* 9.4 (2019), pp. 81–93.

[51] Z. Jiang. “Installation of offshore wind turbines: A technical review”. In: *Renewable and Sustainable Energy Reviews* 139 (2021), p. 110576.

[52] J.M.J. Journée and W.W. Massie. *Offshore Hydromechanics, 1st Edition*. Delft University of Technology, the Netherlands, 2008.

[53] C. M. Jubayer and H. Hangan. “A numerical approach to the investigation of wind loading on an array of ground mounted solar photovoltaic (PV) panels”. In: *Journal of Wind Engineering and Industrial Aerodynamics* 153 (2016), pp. 60–70.

[54] J. Jurasz, J. Mikulik, M. Krzywda, B. Ciapała, and M. Janowski. “Integrating a wind-and solar-powered hybrid to the power system by coupling it with a hydroelectric power station with pumping installation”. In: *Energy* 144 (2018), pp. 549–563.

[55] V. Khare, S. Nema, and P. Baredar. “Solar–wind hybrid renewable energy system: A review”. In: *Renewable and Sustainable Energy Reviews* 58 (2016), pp. 23–33.

[56] S. Kim, S. Yoon, and W. Choi. “Design and construction of 1 MW class floating PV generation structural system using FRP members”. In: *Energies* 10.8 (2017), p. 1142.

[57] V. Klonari, D. Fraile, R. Rossi, and M. Schmela. “Exploring the Viability of hybrid wind-solar power plants”. In: *Proceedings of the 4th International Hybrid Power Systems Workshop, Crete, Greece*. 2019, pp. 22–23.

[58] K. Kudou. “The Drifting Force acting on a Three-dimensional Body in Waves (1 st report)”. In: *Journal of the Society of Naval Architects of Japan* 1977.141 (1977), pp. 71–77.

[59] N. P. Kumar, K. Balaraman, and C. Shekar R. Atla. “Optimal mix of wind-solar PV hybrid power plant with minimum variability”. In: *2016 IEEE 6th International Conference on Power Systems (ICPS)*. IEEE. 2016, pp. 1–6.

[60] M. Liang, X. Wang, S. Xu, and A. Ding. “A shallow water mooring system design methodology combining NSGA-II with the vessel-mooring coupled model”. In: *Ocean Engineering* 190 (2019), p. 106417.

[61] H. Long, M. Eghlimi, and Z. Zhang. “Configuration optimization and analysis of a large scale PV/wind system”. In: *IEEE Transactions on Sustainable Energy* 8.1 (2016), pp. 84–93.

[62] M. López, N. Rodrı´guez, and G. Iglesias. “Combined floating offshore wind and solar PV”. In: *Journal of Marine Science and Engineering* 8.8 (2020), p. 576.

[63] D. Ludwig, C. Breyer, A.A. Solomon, and R. Seguin. “Evaluation of an onsite integrated hybrid PV-Wind power plant”. In: *AIMS Energy* 8.5 (2020), pp. 988–1006.

[64] K. T. Ma, Y. Luo, C. T. T. Kwan, and Y. Wu. *Mooring system engineering for offshore structures*. Gulf Professional Publishing, 2019.

[65] T. Ma, H. Yang, L. Lu, and J. Peng. “Optimal design of an autonomous solar–wind-pumped storage power supply system”. In: *Applied Energy* 160 (2015), pp. 728–736.

[66] A. Maleki and A. Askarzadeh. “Comparative study of artificial intelligence techniques for sizing of a hydrogen-based stand-alone photovoltaic/wind hybrid system”. In: *international journal of hydrogen energy* 39.19 (2014), pp. 9973–9984.

[67] I Mamia and J Appelbaum. “Shadow analysis of wind turbines for dual use of land for combined wind and solar photovoltaic power generation”. In: *Renewable and Sustainable Energy Reviews* 55 (2016), pp. 713–718.

[68] H. Maruo. “The drift on a body floating in waves”. In: *J. Ship Res.* 4.3 (1960), pp. 1–10.

[69] D. Mazzeo, N. Matera, P. De Luca, C. Baglivo, P. M. Congedo, and G. Oliveti. “A literature review and statistical analysis of photovoltaic-wind hybrid renewable system research by considering the most relevant 550 articles: An upgradable matrix literature database”. In: *Journal of Cleaner Production* 295 (2021), p. 126070.

[70] G. Merei, M. Leuthold, and D. U. Sauer. “Optimization of an Off-grid hybrid PV-Wind-Diesel system with different battery technologies-Sensitivity Analysis”. In: *Intelec 2013; 35th International Telecommunications Energy Conference, SMART POWER AND EFFICIENCY*. VDE. 2013, pp. 1–6.

[71] S Mertens. “Design of wind and solar energy supply, to match energy demand”. In: *Cleaner Engineering and Technology* (2022), p. 100402.

[72] N. Mezzai, D. Rekioua, T. Rekioua, A. Mohammedi, K. Idjdarane, and S. Bacha. “Modeling of hybrid photovoltaic/wind/fuel cells power system”. In: *International journal of hydrogen energy* 39.27 (2014), pp. 15158–15168.

[73] H. E. Murdock, D. Gibb, T. Andre, J. L. Sawin, A. Brown, L. Ranalder, U. Collier, C. Dent, B. Epp, C. Hareesh Kumar, et al. “Renewables 2021-Global status report”. In: (2021).

[74] A. Myhr, C. Bjerkseter, A. Ågotnes, and T. A. Nygaard. “Levelised cost of energy for offshore floating wind turbines in a life cycle perspective”. In: *Renewable energy* 66 (2014), pp. 714–728.

[75] A. Naeem, N. U. Hassan, and N. Arshad. “Design of Solar-Wind Hybrid Power System by using Solar-Wind Complementarity”. In: *2020 4th International Conference on Green Energy and Applications (ICGEA)*. IEEE. 2020, pp. 100–105.

[76] LHEAA Centrale Nantes. *NEMOHH Presentation*. `https://lheea.ec-nantes.fr/valorisation/logiciels-et-brevets/nemoh-presentationl`. accessed on 13/10/2022.

[77] J. N. Newman. “The drift force and moment on ships in waves”. In: *Journal of ship research* 11.01 (1967), pp. 51–60.

[78] P. Paliwal, N.P. Patidar, and R.K. Nema. “Determination of reliability constrained optimal resource mix for an autonomous hybrid power system using particle swarm optimization”. In: *Renewable energy* 63 (2014), pp. 194–204.

[79] J. A. Pinkster and G. Van Oortmerssen. “Computation of the first and second order wave forces on oscillating bodies in regular waves”. In: *Proceedings of the 2nd International Conference on Numerical Ship Hydrodynamics, Berkeley, California, USA*. 1978.

[80] D. V. Pombo, A. G. Raducu, N. Styliaras, O. Sahin, S. Thanopoulos, J. Funkquist, and E. Shayesteh. “The first utility scale hybrid plant in Europe: The case of Haringvliet”. In: *Virtual 5th International Hybrid Power Systems Workshop*. 2021.

[81] Energy Sector Management Assistance Program and Solar Energy Research Institute of Singapore. *Where Sun Meets Water: Floating Solar Handbook for Practitioners*. World Bank, 2019.

[82] J. Qian, L. Mu, Y. Zhang, and Y. Zhang. “Behavior of a Structured Piled Beam–Slab Foundation for a Wind Turbine under Multidirectional Loads in Sand”. In: *International Journal of Geomechanics* 21.3 (2021), p. 04020267.

[83] M. Redón-Santafé, P. Ferrer-Gisbert, F.J. Sánchez-R., J. B. Torregrosa Soler, J. J. Ferran Gozalvez, and C. M. Ferrer Gisbert. “Implementation of a photovoltaic floating cover for irrigation reservoirs”. In: *Journal of cleaner production* 66 (2014), pp. 568–570.

[84] G. Reikard, B. Robertson, and J. R. Bidlot. “Combining wave energy with wind and solar: Short-term forecasting”. In: *Renewable Energy* 81 (2015), pp. 442–456.

[85] J. Robledo, J. Leloux, B. Sarr, C. A. Gueymard, and P. Darez. “Dynamic simulation of the shading cast by a wind farm on an adjacent photovoltaic plant”. In: ().

[86] G. Rubio-Domingo and P Linares. “The future investment costs of offshore wind: An estimation based on auction results”. In: *Renewable and Sustainable Energy Reviews* 148 (2021), p. 111324.

[87] A. Sahu, N. Yadav, and K. Sudhakar. “Floating photovoltaic power plant: A review”. In: *Renewable and sustainable energy reviews* 66 (2016), pp. 815–824.

[88] R. G. Sanchez, I. Kougias, M. Moner-Girona, F. Fahl, and A. Jäger-Waldau. “Assessment of floating solar photovoltaics potential in existing hydropower reservoirs in Africa”. In: *Renewable Energy* 169 (2021), pp. 687–699.

[89] S. Sánchez, J. S. López-Gutiérrez, V. Negro, and M. D. Esteban. “Foundations in offshore wind farms: Evolution, characteristics and range of use. Analysis of main dimensional parameters in monopile foundations”. In: *Journal of Marine Science and Engineering* 7.12 (2019), p. 441.

[90] T. Sarpkaya. *Morison’s Equation and the Wave Forces on Offshore Structures.* Tech. rep. SARPKAYA (TURGUT) CARMEL CA, 1981.

[91] Y. Sawle, S.C. Gupta, and A. K. Bohre. “Optimal sizing of standalone PV/Wind/Biomass hybrid energy system using GA and PSO optimization technique”. In: *Energy Procedia* 117 (2017), pp. 690–698.

[92] D. Schindler, H. D. Behr, and C. Jung. “On the spatiotemporal variability and potential of complementarity of wind and solar resources”. In: *Energy Conversion and Management* 218 (2020), p. 113016.

[93] W. M. Shanghavi S.and Grady and B. Schwarz. “Evaluating the impact of wind turbine shadows on an integrated wind and solar farm”. In: *2012 3rd IEEE PES Innovative Smart Grid Technologies Europe (ISGT Europe)*. IEEE. 2012, pp. 1–6.

[94] S. Silvestre and A. Chouder. “Effects of shadowing on photovoltaic module performance”. In: *Progress in Photovoltaics: Research and applications* 16.2 (2008), pp. 141–149.

[95] Mohammed Yekini Suberu, Mohd Wazir Mustafa, and Nouruddeen Bashir. “Energy storage systems for renewable energy power sector integration and mitigation of intermittency”. In: *Renewable and Sustainable Energy Reviews* 35 (2014), pp. 499–514.

[96] L. Sun, R. E. Taylor, and Y. S. Choo. “Responses of interconnected floating bodies”. In: *The IES Journal Part A: Civil & Structural Engineering* 4.3 (2011), pp. 143–156.

[97] L. Sun, R. E. Taylor, and P. H. Taylor. “First-and second-order analysis of resonant waves between adjacent barges”. In: *Journal of Fluids and Structures* 26.6 (2010), pp. 954–978.

[98] K Suyehiro. “The drift of ships caused by rolling among waves”. In: *Trans. Inst. Naval Arch* 66 (1924).

[99] B. E. Türkay and A. Y. Telli. “Economic analysis of standalone and grid connected hybrid energy systems”. In: *Renewable energy* 36.7 (2011), pp. 1931–1943.

[100] N. Vani and V. Khare. “Rural electrification system based on hybrid energy system model optimization using HOMER”. In: *Can J Basic Appl Sci* 1 (2013), pp. 19–25.

[101] S. Venkataraman, C. Ziesler, P. Johnson, and S. Van Kempen. “Integrated wind, solar, and energy storage: Designing plants with a better generation profile and lower overall cost”. In: *IEEE Power and Energy Magazine* 16.3 (2018), pp. 74–83.

[102] Det Norske Veritas. *Design, Development and Operation of Floating Solar Photovoltaic Systems*. Tech. rep. Technical Report. Available online: https://www. dnv. com/energy/standards . . ., 2021.

[103] J. V. Wehausen. “The motion of floating bodies”. In: *Annual review of fluid mechanics* 3.1 (1971), pp. 237–268.

[104] P. Wellens. *Motions loading of structures in waves, Part 2, Lecture Notes in Offshore and Dredging Engineering*. Delft University of Technology, the Netherlands, Nov. 2021.

[105] R. J. S. Whitehouse, J. Sutherland, and J. M. Harris. “Evaluating scour at marine gravity foundations”. In: *Proceedings of the Institution of Civil Engineers-Maritime Engineering*. Vol. 164. 4. Thomas Telford Ltd. 2011, pp. 143–157.

[106] T. Whittaker, M. Folley, and J. Hancock. “Environmental Loads, Motions, and Mooring Systems”. In: *Floating PV Plants*. Elsevier, 2020, pp. 47–66.

[107] WindEurope. *Renewable Hybrid Power Plants: Exploring the benefits and market opportunities*. `https://windeurope.org/policy/position-papers/renewable-hybrid-power-plants-exploring-the-benefits-and-market-opportunities/`. [Online; accessed 19-March-2022]. 2022.

[108] WindEurope. *WindEurope’s online dataset of co-located projects*. `https://windeurope.org/about-wind/database-for-wind-and-storage-colocated-projects/`. [Online; accessed 19-March-2022]. 2022.

[109] D. Xu, L. Kang, L. Chang, and B. Cao. “Optimal sizing of standalone hybrid wind/PV power systems using genetic algorithms”. In: *Canadian Conference on Electrical and Computer Engineering, 2005.* IEEE. 2005, pp. 1722–1725.

[110] J. Yan, T. Qu, S. Han, Y. Liu, X. Lei, and H. Wang. “Reviews on characteristic of renewables: Evaluating the variability and complementarity”. In: *International Transactions on Electrical Energy Systems* 30.7 (2020), e12281.

[111] R. Y. Yang and S. H. Yu. “A Study on a Floating Solar Energy System Applied in an Intertidal Zone”. In: *Energies* 14.22 (2021), p. 7789.

[112] I. R. Young and L. A. Verhagen. “The growth of fetch limited waves in water of finite depth. Part 1. Total energy and peak frequency”. In: *Coastal Engineering* 29.1-2 (1996), pp. 47–78.

[113] F. Yu, Y. Su, Y. Liu, H. Liu, and F. Duan. “Dynamic response of the mooring system in the floating photovoltaic power station”. In: *Journal of Physics: Conference Series*. Vol. 2087. 1. IOP Publishing. 2021, p. 012028.

A | LCOE Analysis

This appendix presents the analytical calculations that were performed for the estimation of LCOE. The starting year of construction is assumed to be 2030 and only the first 6 years are illustrated for presentation reasons.

Assumptions (in 2022)	
Initial Investment Cost (€)	48,048,00
Operations and Maintenance Costs (€)	693,000
O&M Growth Rate (%)	0.00%
Degradation of Panels (%)	0.5%
Annual Fuel Costs (€)	-
Annual Electricity Output (kWH)	96,200,00
Project Lifespan (years)	30
Discount Rate (%)	6.00%
Entry Date	31/12/2030

Total Costs	Entry	Construction	Operations	Operations	Operations	Operations	Operations
Date	31/12/2030	31/12/2031	31/12/2032	31/12/2033	31/12/2034	31/12/2035	31/12/2036
Year Frac (From Start Date)		1	2	3	4	5	6
Initial Investment	48,048,000	-	-	-	-	-	-
O&M Costs	-	693,000	693,000	693,000	693,000	693,000	...
Fuel Costs	-	-	-	-	-	-	-
Discount Factor		0.943	0.890	0.840	0.792	0.747	...
Present Value of Costs	48,048,000	653,774	616,768	581,856	548,921	517,850	...
NPV of Total Costs	€ 57,587,028						

Total Energy Output	Entry	1	2	3	4	5	6
Yearly Output	-	96,200,000	95,719,000	95,240,405	94,764,203	93,818,930	...
Discount Factor	-	0.943	0.890	0.840	0.792	0.747	...
Present Value of Costs	-	90,754,717	85,189,569	79,965,681	75,062,125	70,459,259	...
NPV of Total Output	1,258,293,626 kWh						

LCOE	€45,77/MWh

Table A.1: Solar LCOE analytical calculation

Assumptions (in 2030)	
Initial Investment Cost (€)	31.974.400
Operations and Maintenance Costs (€)	1.280.000
O&M Growth Rate (%)	0.00%
Degradation of Wind Turbines (%)	0.5%
Annual Fuel Costs (€)	-
Annual Electricity Output (kWH)	75,400,400
Project Lifespan (years)	30
Discount Rate (%)	6.00%
Entry Date	31/12/2030

Total Costs	Entry	Construction	Operations	Operations	Operations	Operations	Operations
Date	31/12/2030	31/12/2031	31/12/2032	31/12/2033	31/12/2034	31/12/2035	31/12/2036
Year Frac (From Start Date)		1	2	3	4	5	6
Initial Investment	31,974,400	-	-	-	-	-	-
O&M Costs	-	1,280,000	1,280,000	1,280,000	1,280,000	1.280.000	...
Fuel Costs	-	-	-	-	-	-	-
Discount Factor		0.943	0.890	0.840	0.792	0.747	...
Present Value of Costs	31,974.000	1,207,547	1,139,195	1,074,713	1,013,880	956,490	902,349 ...
NPV of Total Costs	€ 49,593,384						

Total Energy Output	Entry	1	2	3	4	5	6
Yearly Output	-	75,400,000	75,023,000	74,647,885	74,274,646	73,903,272	...
Discount Factor	-	0.943	0.890	0.840	0.792	0.747	...
Present Value of Costs	-	71,132,075	66,770,203	62,675,804	58,832,476	55,224,824	...
NPV of Total Output	986,230,139 kWh						

LCOE	€50.29/MWh

Table A.2: Wind LCOE analytical calculation

B | Analytical Wind Loads

As was discussed in Section3.2.3, the main equation for the calculation of the wind loads is:

$$F_{wind} = \frac{1}{2}\rho V^2 A C_d C_s$$

Where,

- ρ is the density of the fluid
- A is the area exposed to the flow
- V is the flow velocity (at the corresponding height)
- C_s is the sheltering coefficient to account for the presence of multiple objects
- C_d is the drag coefficient and depends on the shape and surface roughness of the considered object

The density of the air is $1.225 kg/m^3$ and the velocity is taken as the one with 100-return period, and which for the height of 0.5m has a value of $V = 15.2 m/s$.
The geometry of the solar panels and the floaters, and the corresponding area exposed to the flow, is given in Table B.1.

Panels Geometry		Unit	Floaters Geometry		Unit
Depth	2285	mm	Height	630	mm
Length	1134	mm	Draft	360	mm
Width	35	mm	Freeboard	270	mm
Tilt	12	o	Width	588	mm
Weight	31.63	kg	Length	2100	mm
			Weight	30.89	kg
Projected area			Projected area		
0^o	0.539	m^2	0^o	0.567	m^2
90^o	0.080	m^2	90^o	0.159	m^2

Table B.1: Properties of the solar panels and the floaters

The values of the drag coefficient are adopted according to DNV-RP-C205 [24] based on the closest shape available in the guideline (Table B.2).

Object	Load Cases	Closest Shape in DNV-RP-C205	C_d
Floater	0^o/90^o/180^o/270^o	Cube	1.05
Panel	0^o/180^o	Isosceles triangle shape	1.1
Panel	90^o/270^o	Cube	1.05

Table B.2: Drag coefficients for various shapes

The sheltering coefficients for each row of panes are presented in TableB.3 and are adopted from [43].

Sheltering coefficient for each row of panels	$C_s - 0^o$	$C_s - 90^o$
Row 1	1.0	1.0
Row 2	0.4	0.1
Row 3	0.3	0.1
Row >3	0.1	0.1

Table B.3: Sheltering coefficients for every row of panels

For the estimation of the sheltering coefficients of the floaters, analytical formulas from [24] will be used. This is done because two floaters of the same solar boat have different distances from the floaters of the next floater. This is illustrated in FigureB.1.

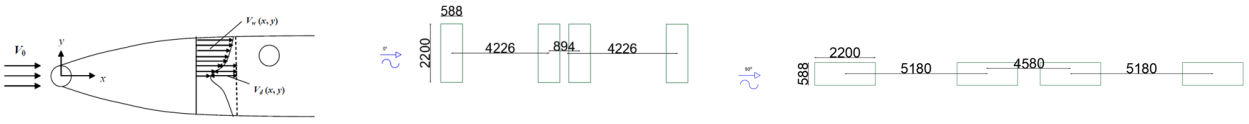

(a) Wake recovery [24]

(b) Floaters in 0^o incoming flow (distances in mm)

(c) Floaters in 90^o incoming flow (distances in mm)

Figure B.1: Sheltering effects for the floaters

The velocity in the wake can be taken as:

$$v_w(x, y) = v_0 - v_d(x, y)$$

where, v_0 denotes the free-stream current velocity acting on the upstream body and $v_d(x, y)$ is the deficit velocity field given as:

$$v_d(x, y) = k_2 v_0 \sqrt{\frac{C_D D}{x_s}} e^{-0.693(\frac{y}{b})^2}$$

where:

$$x_s = x + \frac{4D}{C_D}$$

$$b = k_1 \sqrt{C_D D x_s}$$

The empirical constants k_1 and k_2 have values of 0.25 and 1.0 respectively.
With the use of the above equations and the distances as dictated in Figures B.1b and B.1c, the sheltering coefficients for the floaters are presented in Table B.4.

Sheltering coefficient for each row of floater	$C_s - 0^o$	$C_s - 90^o$
Row 1	1.0	1.0
Row 2	0.5	0.6
Row 3	0.2	0.4
Row >3	0.1	0.1

Table B.4: Sheltering coefficients for every row of floaters

For the base case design described in Section 3.1.4, every floating solar unit is consisted of 20 rows and 20 columns. So, the total wind forces acting on a solar unit for a wind blowing vertically to the larger dimension of the solar boat (0^o) would be: $13.4kN$ resulting from the freeboard of the floaters and $36.3kN$ resulting from the solar panels.